The Dissertation Committee for Pinan Dawkrajai Certifies that this is the approved version of the following dissertation:

Temperature Prediction Model for a Producing Horizontal Well

Committee:

Larry W. Lake, Supervisor

A. Daniel Hill

Ding Zhu

Ekwere J. Peters

Quoc P. Nguyen

Temperature Prediction Model for a Producing Horizontal Well

by

Pinan Dawkrajai, B.S.; M.S.

Dissertation

Presented to the Faculty of the Graduate School of

The University of Texas at Austin

in Partial Fulfillment

of the Requirements

for the Degree of

Doctor of Philosophy

The University of Texas at Austin

August 2006

Dedication

This dissertation is dedicated to my mother who has passed away while I was writing.

Acknowledgements

I would like to express my gratitude and appreciation to Prof. Larry W. Lake, Prof. A. Daniel Hill and Asst. Prof. Ding Zhu for their guidance throughout this research project. Without their advice and attention to the details, these results would not have been found. I would like to especially thank Prof. Larry W. Lake for being patient and kind to me throughout this study although I had messed his blackboard with an expanded version of energy balance because I initially did not know what to do and which terms are important. I am also grateful to Prof. Ekwere J. Peters and Asst. Prof. Quoc P. Nguyen for their willingness to serve as members of the dissertation committee. I want to extend my gratitude to all members of the Petroleum and Geosystems Engineering Department who have helped me with the execution of this work. I want to thank my wife Jarukamol and my son Napat for their love and support. They have provided me with understanding that enabled me to have many hours from family while working on this research. I would like to express my appreciation to the U.S. Department of Energy NETL for providing financial support through the Department of Petroleum and Geosystems Engineering. Finally, I would like to thank the participants (Keita Yoshioka and Analis A. Romero) of this research project for the feedback they have given me.

Temperature Prediction Model for a Producing Horizontal Well

Publication No._____

Pinan Dawkrajai, Ph.D.

The University of Texas at Austin, 2006

Supervisor: Larry W. Lake

Distributed temperature sensors (DTS) are increasingly used for monitoring producing sections of horizontal wells. The temperature data from DTS are reliable, accurate and continuous in time (readings every few minutes) and space (readings every meter). One of the potential uses of DTS is to infer the amount and types of fluid entering horizontal sections. To perform such an inference requires a temperature model.

A new analytical model was developed here for predicting the inflow temperature of a fluid entering a horizontal wellbore during production. The distinguishing aspect of the model is that it accounts for subtle thermal energy effects including fluid expansion, viscous dissipative heating, and thermal conduction. Reservoir inflow and wellbore flow are coupled by modeling the reservoir as multi-segmented reservoirs in which the direction of flow in the reservoir is perpendicular (not parallel) to the wellbore. The coupled model is then used to simulate several examples to illustrate how temperature changes with flow rate and type of fluid entering a wellbore.

We further develop a numerical temperature model of a bottom water drive reservoir to demonstrate the uses of temperature profiles in detecting water entries. Water in this numerical model is initially located in a deeper and warmer zone below a horizontal well.

Results show that oil or water can enter the wellbore 2-3 ^{o}F higher, while gas can enter with 5-6 ^{o}F lower, than the geothermal temperature. Inflow temperature causes the slope of the wellbore temperature profile to change notably, depending on the flow rates and types of fluid entering. The temperature profile can locate a zone that is producing excessive water or gas if the rate is large. The size of the temperature changes on the profiles is obviously detectable by DTS, which has a resolution as fine as 0.0045 ^{o}F for the time and spatial average of 1 hour and 50 feet if the cable range is less than 3,000 feet. This study has confirmed the uses of DTS in reservoir monitoring of a horizontal production well.

Table of Contents

List of Tables

List of Figures

xiv

CHAPTER   1

Introduction

This study addresses the question of whether distributed temperature data could be used to infer other useful information such as amount and types of fluid entering a wellbore.   This information is essential for reservoir management and well performance optimizeation, for example, to identify excessive water or gas entries or to decide if reservoir stimulation is needed in a particular section of a well.   Although the temperature data may also help in other applications, for example, inferring injectivity profiles for an injection well, this study focuses only on temperature data in a horizontal well that is producing under steady-state flow or for a sufficiently long time.   The early-time heat transfer effects are not studied here because temperature data tend to reflect long term behavior in a well, not just current conditions.

In the first section of this chapter, the motivation of the study is presented.   The specific objectives are listed in Section 1.2.   Section 1.3 emphasizes the contribution of this study to current knowledge.   Section 1.4 presents the outline of this dissertation.

1.1 MOTIVATIONS

There are three main motivations to study temperature profiles in horizontal wells during production; (1) the advancement of distributed temperature measurement, (2) the past successes of temperature measurement and interpretation in some applications, and (3) the proliferation of horizontal wells as driven by continued advances in drilling technology.

1.1.1 Advancement of distributed temperature measurement

Fiber-optic technology has made downhole temperature measurement very accurate and reliable. A recent development is distributed temperature sensors (DTS). DTS employ a thin glass fiber optical cable installed along the entire length of the well. Laser light sent through the cable scatters with characteristics that depend on the local temperature. It is then possible to obtain a temperature profile with resolution less than 0.0045 ^{o}F at some spatial and temporal resolutions. It is also possible to measure temperature at a distance of several kilometers, with a spatial resolution of one meter, and with a measurement time of typically a few minutes (Sensornet Limited, 2006).

Many field applications of this technology have been reported. For example, in an Oman oilfield fiber sensors were installed in several long horizontal open-hole completion intervals of production and injection wells. The results show that it is cost effective and less risky than conventional production logging in horizontal wells. Analysis of the data has helped the understanding of flow in a horizontal producer and injector (Brown *et al*., 2003). Another application of this technology is to install sensors together with downhole mechanical instrumentation such as valves and inflow control devices. Distributed temperature measurements at meter long intervals in the wellbore provide real-time data that help identify water flowing into a particular section. Then, an action to shut in the zone is possible with remotely operated hydraulic interval control values (Tolan *et al*., 2001).

Unlike a production log that provides only snapshots of the reservoir performance, the DTS enables continuous monitoring of a well to detect temporal changes in the temperature profiles. This advancement of the temperature measurement has motivated us to develop a model to translate temperature data into flow information, which is important for reservoir management.

1.1.2 Past successes of temperature interpretation

Downhole temperature measurement is not new to oil and gas wells. A temperature instrument has been a part of production logging tools for many years. Temperature logs have been used successfully in vertical wells to locate gas entries, detect casing leaks, evaluate cement placement, and estimate inflow profiles. Recently, interpretations of temperature in horizontal wells are reported to be useful to identify types of fluid flowing to a wellbore (Tolan *et al.*, 2001; Brown *et al.*, 2003; Foucault *et al.*, 2004). The unwanted fluid is isolated by means of an intelligent well technology. These benefits have encouraged further investigation of the potential uses of temperature profiles of horizontal well from DTS.

1.1.3 Proliferation of horizontal wells

Horizontal wells have become a common production technique for oil and gas recovery. They provide large contact area with the reservoir, so a large flow rate is produced from the well. Producing sections of horizontal wells are usually thousands of feet long and require close observation so that the large production rate is maintained. A surveillance tool that is most likely to be deployed in such a horizontal well is DTS. This is one of the reasons why we study temperature profiles of horizontal wells.

Analyzing temperature profile is challenging. For example, the flow geometry of horizontal wells is much more complex than vertical wells because the flow is constrained by the horizontal reservoir boundaries. Certain assumptions must be made to derive both the flow and temperature models. Another challenge is that geothermal temperatures along a horizontal well are almost constant. The size of temperature change is expected to be small, so it is crucial to include subtle thermal energy effect; heat convection, fluid expansion, viscous dissipation, and thermal conduction. Neglecting the subtle thermal energy would result in an immediate conclusion that the

3

wellbore temperature profile does not change along horizontal sections because of the small variation in geothermal temperature at well depth.

1.2 OBJECTIVES

Although distributed temperature sensors are widely accepted to provide high accuracy and fine resolution, there are still challenges on how to improve temperature measurement, to transfer a large amount of data, and to install sensors in a well. This study will not deal with those measurement challenges. We assume that the temperature measurement is perfect and focus study on the meaning of temperature data and their value for monitoring well performance in production wells.

The main objective is to develop a temperature prediction model and use it to demonstrate the size of temperature change in a horizontal well under some production scenarios. Basically, we will investigate how the origin, amount, and types of fluid entering a well affect temperature profiles.

Figure 1.1 depicts what the study is about. It shows a physical model of a horizontal well producing fluid from a box-shaped reservoir. Under this particular geometry, the mathematical models (mass and energy balances) that describes non-isothermal flow, both in the wellbore and the reservoir, predict the temperature, pressure, and inflow rate profiles that are used to analyze temperature behavior and its values in reservoir monitoring.

With these broad objectives in mind, we can itemize the specific goals of the study as the following.

1. Study previous literature pertaining to productivity of horizontal wells, the application of the temperature measurement from DTS, and temperature models that are used in temperature logging interpretation.

4

2.   Develop analytical and numerical models that predict wellbore temperature, wellbore pressure and inflow rates.

3.   Demonstrate the size of temperature changes caused by flow rates, types of fluid, and no-flow interval.

4.   Explain the occurrence of variations in temperature profiles.

5.   Evaluate conditions in which the temperature data from DTS could be useful.
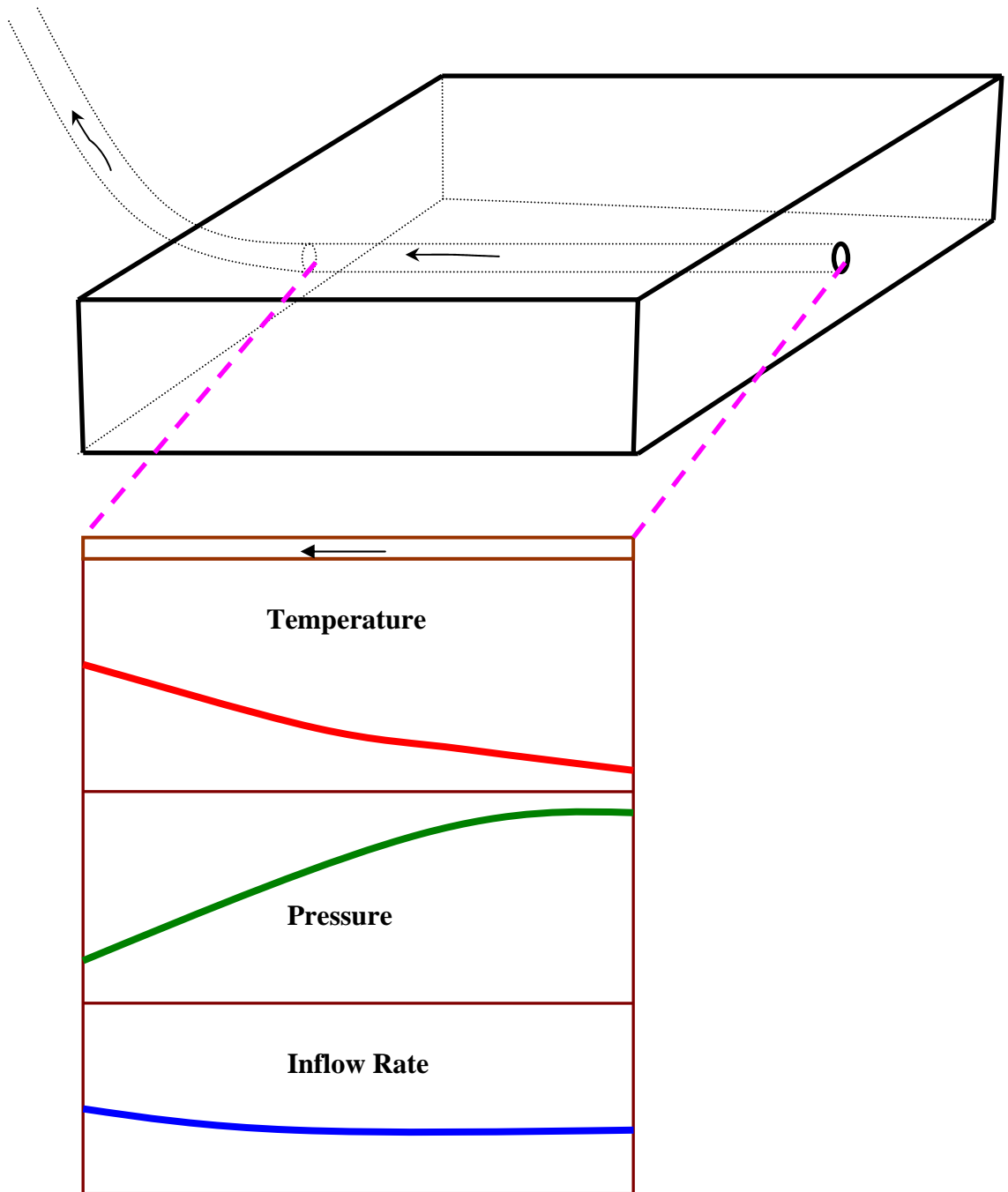
Figure 1.1   Schematic of predicted results from the temperature model of flow in a
horizontal well.

1.3 CONTRIBUTIONS OF THIS STUDY

To the best of our effort in reviewing the literature, there is no analytical temperature model of fluid entering horizontal wellbore that takes into account the effects of the subtle thermal energy change, including heat conduction, convection, viscous dissipation, and fluid expansion for flow in reservoir. Including this subtle thermal energy change in the model is a contribution of this study in that it predicts inflow and wellbore temperature of the fluid, and extends the applicability to a horizontal well where the wellbore temperature does not change significantly along horizontal wells because of the constant geothermal temperature along horizontal sections.

In this study, we have developed an analytical inflow temperature model, and then coupled it with an available numerical wellbore model to predict temperature profiles in horizontal wells.   We do not attempt to develop an analytical model for two-phase flow. Instead, we develop a numerical model to study temperature behavior and to develop a criterion to detect water entries in horizontal wells.

1.4 ORGANIZATION OF THE DISSERTATION

This dissertation is organized into five chapters.   This first chapter presents the introduction including an overall importance of the study, motivation, and objectives. The second chapter provides the background of subjects involved in the study.   Section 2.1 reviews basic concepts and applications of temperature logs.   Section 2.2 gives the background of horizontal well productivity, including rigorous and approximate models under steady and pseudosteady flow conditions.   The aim of Section 2.2 is to present a flow model that is suitable for coupling with energy balance of reservoir flow.   Section 2.3 presents the wellbore flow model that is used to couple with the reservoir flow model. Appendix A presents a summary of fluid property correlations used in the study.

Chapter 3 discusses the development of a new analytical temperature model for single-phase flow in reservoir. To obtain wellbore temperature profiles, the reservoir model is coupled with a wellbore model. The coupled model is then used to simulate examples to demonstrate how the temperature profile changes with flow rates and types of fluid entering a wellbore. Chapter 4 discusses the development of numerical temperature model for two-phase flow in a bottom water drive reservoir. The numerical model is then used to illustrate a specific condition for which water entry locations can be identified from the temperature profile of a horizontal well. Chapter 5 gives conclusions and recommendations from the study.

CHAPTER 2

Reviews of Temperature Logs and Horizontal Well Models

Before discussing the temperature model and results, let us first review some background about temperature logging, productivity models of a horizontal well, and wellbore flow models. Reviewing these will help understand pressure and temperature profiles in the subsequent chapters.

2.1 TEMPERATURE LOGGING

Temperature logging is probably the oldest production log; it was used as early as the mid 1930's. It continues to be a part of the production logging tool kit because temperature is easy to measure and has features unlike other kind of logs. This overview is intended to provide some basic concepts and applications of temperature logs.

2.1.1 Geothermal temperature

From the fact that heat is transferred from inside the Earth to its surface, we always observed that temperature increases with depth. This temperature that naturally increases with depth is known as geothermal temperature. The rate of increase depends on the types of rock layers and their thermal conductivity. This observation can be simply explained by Fourier's law of heat conduction. Fourier's law states that the heat flux by conduction is proportional to the temperature gradient, which is mathematically represented by

$$\vec{e}_{cond} = -K_{Tt}\vec{\nabla}T \tag{2.1}$$

where K_{Tt} is the total thermal conductivity, including rock and fluid, in the rock layers. It is commonly treated as a constant over particular rock layers, although it is actually a

function of the constituent minerals and fluids within the rock. $\vec{e}_{cond}$ is the heat flux (rate of thermal energy transfer per unit area), which is approximately constant with depth. $\vec{\nabla}T$ is the temperature gradient; and the minus sign shows that the transfer is in the direction of decreasing temperature.   Assuming $\vec{e}_{cond}$ is constant, we can sketch the geothermal temperature profile as a straight line over the depth of interest.   The slope of the geothermal temperature in each rock layers depends on its thermal conductivity; the higher the thermal conductivity of a rock layer, the lower the slope across it.

Figure 2.1 shows an example sketch of geothermal temperature profiles. However, in some special geologic setting where rock layers are distorted by igneous intrusions, salt domes, or facies changes, the geothermal temperature profile should be estimated according to those geologic distortions before interpreting temperature logs.
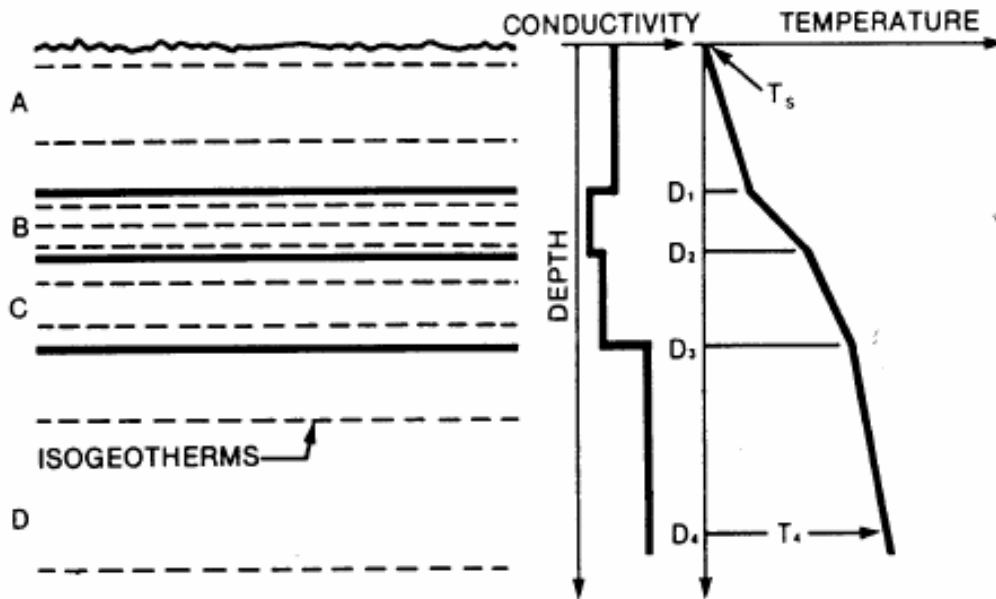
Figure 2.1   Sketch of geothermal temperature profiles (right) for different formations. [From Jorden and Campbell (1984)]

It is important to know the geothermal temperature profile because the interpretation technique of temperature logs are based primarily on both the change in temperature logs and how much the temperature logs deviate from the geothermal temperature. In practice, we can measure the geothermal temperature from a surrogated well that has been shut in for years, or estimate it by taking a bottom-hole reading and linearly extrapolating it to a surface temperature. The geothermal temperature gradients vary significantly from one rock formation to another formation as shown in Figure 2.2, wherein geothermal gradients range from 0.0045 to 0.034 ^{o}F/ft.

Depth (feet)
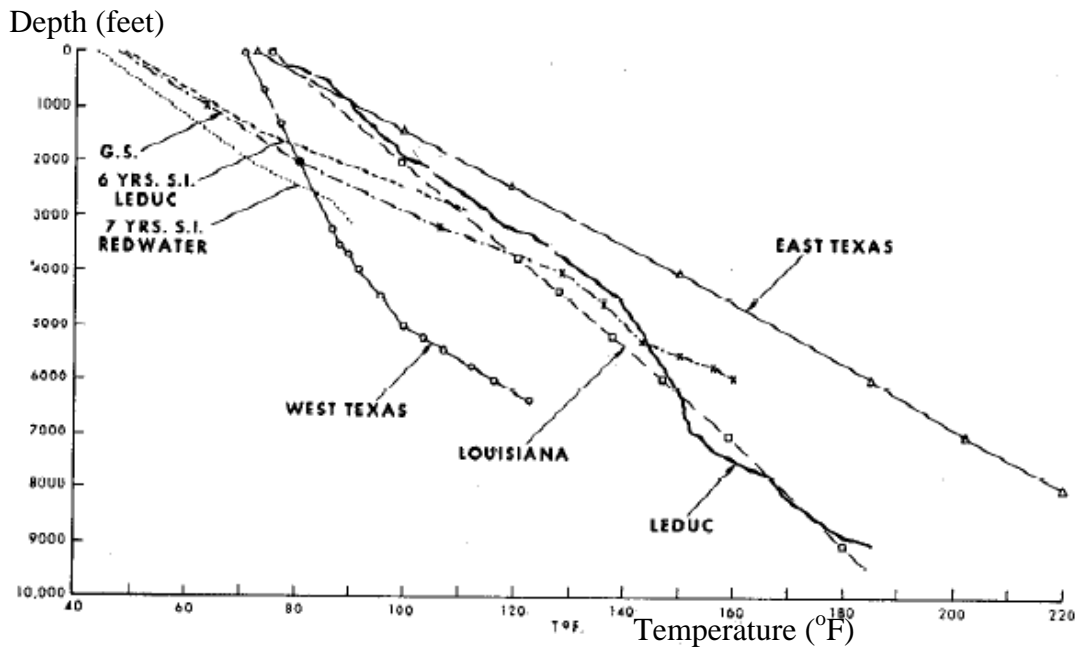
Figure 2.2   Measured geothermal temperatures in United State oil fields. [From Connolly (1965)]

2.1.2   Joule-Thomson effect

When a fluid expands at constant enthalpy (isenthalpic process) because of pressure drop, the temperature of the fluid changes. This phenomenon is named the

11

Joule-Thomson effect.   The temperature change per unit pressure change is called the Joule-Thomson coefficient, C_{JT}.   An expression for C_{JT} can be derived as follows:

For an isenthalpic process,

$$\Delta H = 0$$

For a pure fluid, the fluid enthalpy is a function of pressure and temperature.   The above equation can then be expanded in the following manner.

$$\left(\frac{\partial H}{\partial T}\right)_p \Delta T + \left(\frac{\partial H}{\partial p}\right)_T \Delta p = 0$$

Apply the definition of the heat capacity and Maxwell's relation of thermodynamics.

$$C_p \Delta T + \left[V - T\left(\frac{\partial V}{\partial T}\right)_p\right]\Delta p = 0$$

Replace the specific volume with the fluid density, $V = \dfrac{1}{\rho}$.   The above equation becomes

$$C_p \Delta T + \left[\frac{1}{\rho} - \frac{T}{\rho}(-\frac{1}{\rho})\left(\frac{\partial \rho}{\partial T}\right)_p\right]\Delta p = 0$$

Substitute definition of thermal expansion coefficient into the equation.

$$C_p \Delta T + \left[\frac{1}{\rho} - \frac{\beta T}{\rho}\right]\Delta p = 0$$

Rearranging the above equation gives the expression for C_{JT}.

$$C_{JT} = \left(\frac{\partial T}{\partial p}\right)_H = \frac{\beta T - 1}{\rho C_p} \tag{2.2}$$

12

where β is the thermal expansion coefficient defined as $-\frac{1}{\rho}\left(\frac{\partial \rho}{\partial T}\right)_p$, and ρ is the

density of the fluid. C_p is the specific heat capacity. For an ideal gas, $\beta = \frac{1}{T}$, and

the Joule-Thomson coefficient is zero, which means that when an ideal gas expands at

constant enthalpy, there is no temperature change. As real fluids expand, cooling occurs

if C_{JT} is positive, while warming occurs if it is negative. For natural gases up to

pressures of about 5,000 psi, C_{JT} is positive in the range of 0.01 to 0.06 ^{o}F per psi

(McCain, 1990). For liquids, a general rule is that C_{JT} is negative for temperatures

below approximately 80-90% of the liquid's critical temperature and positive otherwise.

This rule does not apply, however, for pressures below the liquid's vapor pressure.

Water has a negative C_{JT} for temperature below 500 ^{o}F, and it warms up approximately

0.002-0.003 ^{o}F per psi pressure drop, as do most oils (Steffensen and Smith, 1973).

Fluid flow in a reservoir can be approximated as an isenthalpic flow (no heat nor

work done on fluid). During production, the Joule-Thomson effect is a dominant factor

causing the inflow temperature of the fluid to be different from the geothermal

temperature at that depth.

2.1.3 Applications of temperature logs

Temperature logs are used in many applications both for producing wells and for

injection wells as presented in the literature (Hill, 1990). This section provides a brief

overview of how temperature logs can be used to locate the top of cement, detect casing

leaks, and estimate flow rate profiles. Although this section presents the interpretation

for vertical wells, similar ideas can potentially be modified and applied for the horizontal

wells that will be discussed in Chapter 3 and 4.

2.1.3.1 Locate gas entry

Knowledge of the Joule-Thomson effect helps temperature log interpretation. For example, we can use the temperature log to identify a gas entry in a commingled-production well.   Suppose that a gas producing zone exists between the two oil zones as illustrated in Figure 2.3.   How can a gas entry be identified from the wellbore temperature profile?   Because of the Joule-Thomson effect, the inflow temperature (marked T_I on the Figure 2.3) of the gas from the middle zone is lower than the geothermal temperature.   Also, the mixing between the inflow gas and the wellbore flow lowers the mixed temperature below the geothermal temperature.   Clearly, the middle zone is identified as a gas zone based on the large cooling anomaly on the temperature profile.   However, not all cooling anomalies are gas entries.   Liquid that enters wellbore from a shallower depth can also cause a cooling anomaly.   Consider the top zone (oil) on Figure 2.3.   Here the oil tends to enter wellbore at or slightly above geothermal temperature.   The entering oil mixes with the warmer flow from below; as a result, the new mixed flow is at a temperature between the two.

As the warm fluid from a deep zone is flowing upward over the non-perforated interval (for example, from the depth marked **A** to the depth marked **B** on Figure 2.3), it loses heat through the surrounding formation, so the wellbore temperature profile slants slightly toward the geothermal temperature profile.   If the fluid did not lose or gain heat, the wellbore temperature profile would be vertical from point **A** to point **B'** in Figure 2.3.

Temperature

Depth

Wellbore temperature

Geothermal gradient

B B'

T_I

A

T_I = Gas inflow temperature

Top zone
(oil)

Middle zone
(gas)

Bottom zone
(oil)
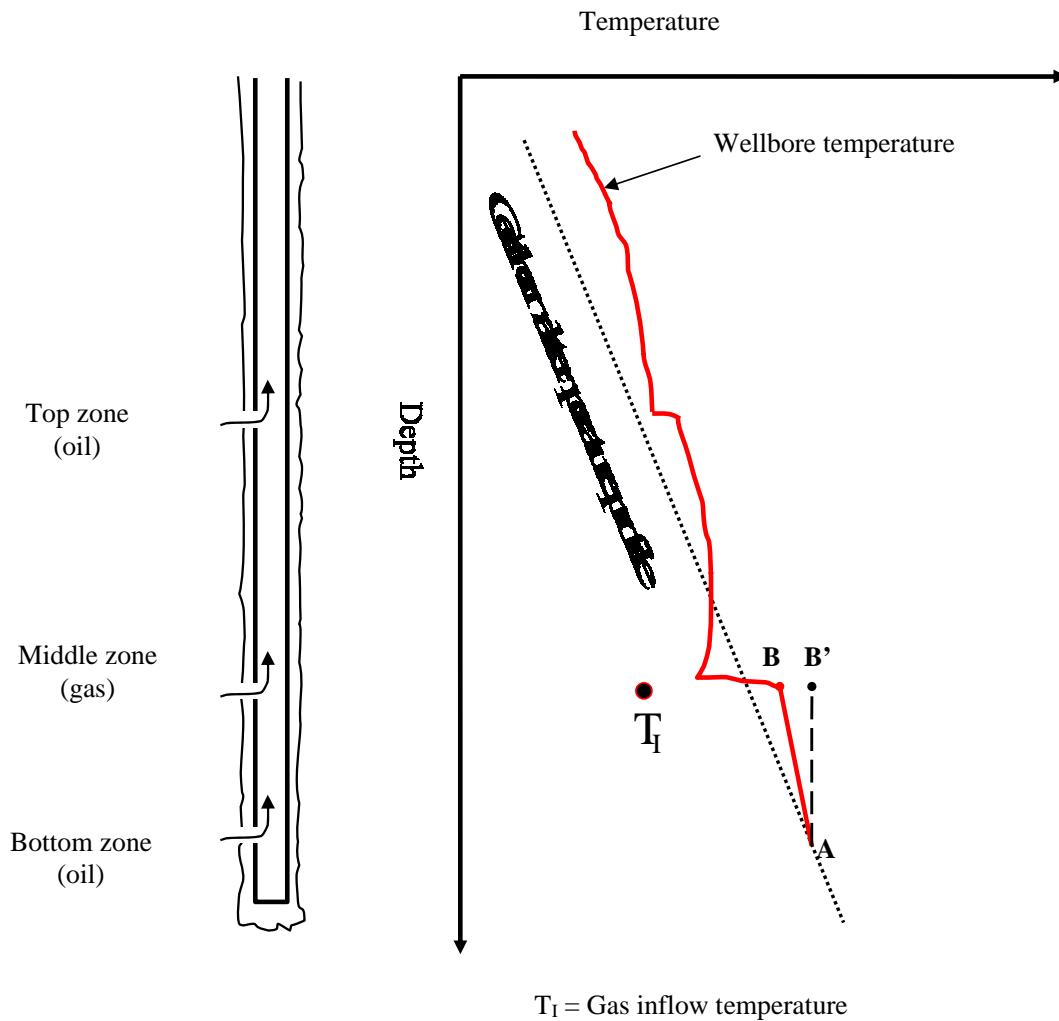
Figure 2.3   Detection of gas entry on a temperature profile by the Joule-Thomson effect.

2.1.3.2   *Locate top of cement*

It is important to verify that the top of the cement is at the location at which it is designed.   Consequently, that means there is no unexpected loss of cement into a thief zone or a big wash-out zone.   A temperature log is a powerful tool to detect the top of

cement by realizing the fact that the curing of cement consists of exothermic reactions. There are two main reactions that release energy when water is added to cement, which is mainly composed of tricalcium silicate and dicalcium silicate.

$$2Ca_3SiO_5 + 7H_2O \rightarrow 3CaO \cdot 2SiO_2 \cdot 4H_2O + 3Ca(OH)_2 + 173.6 \, kJ \qquad (2.3)$$

$$2Ca_2SiO_4 + 5H_2O \rightarrow 3CaO \cdot 2SiO_2 \cdot 4H_2O + Ca(OH)_2 + 58.6 \, kJ \qquad (2.4)$$
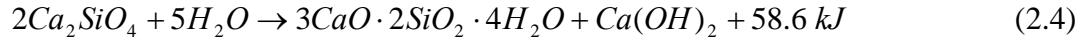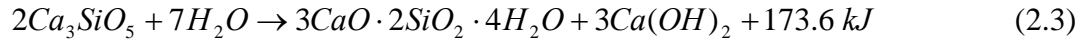
A large amount of thermal energy (232.2 kJ from both reactions per two moles of both silicate) causes a rise in the wellbore temperature that can be easily detected with a temperature log, provided that the log was run right after the curing reactions ended. Figure 2.4 shows an example of a temperature log run for the purpose of locating the top of the cement. The top of the cement is located at the depth of 6,400 feet at which the temperature rises about 5 ^{o}F above the geothermal temperature. The larger volume of cement corresponds to higher temperature rise in the interval from 6,600 to 7,800 feet (Hill,1990).
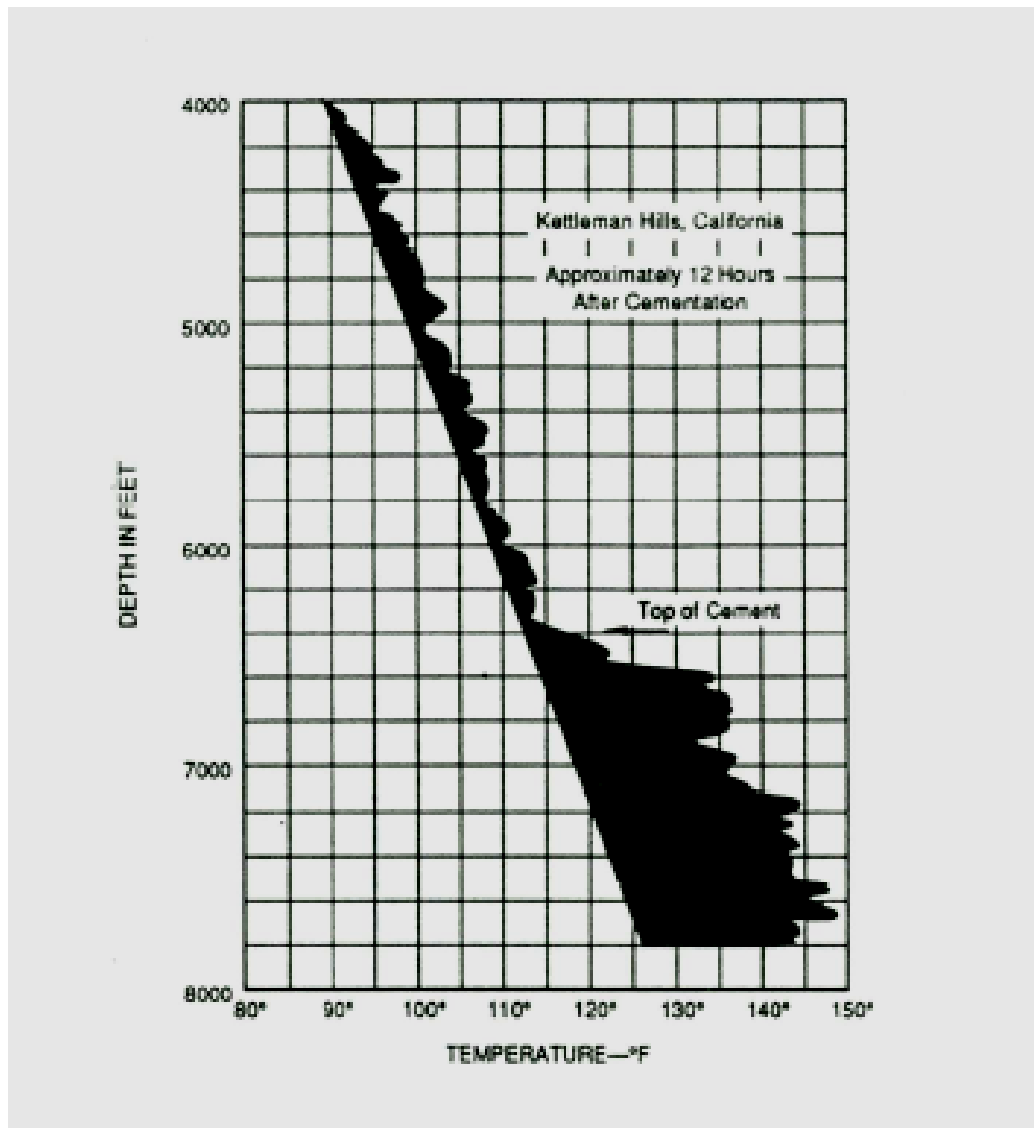
Figure 2.4   Application of temperature log to locate the top of a cement zone. [From Hill (1990)]

2.1.3.3 *Detect casing leaks and channels*

A temperature log alone may not give a unique interpretation, but when combined with other production logs, such as a spinner flowmeter, its interpretation can be clear and unique.   For example, suppose that we have a temperature log like the one shown in

17

Figure 2.5.   The top zone is perforated and producing oil.   The wellbore temperature profile deviated from the geothermal temperature profile indicates that there is an upward flow from the depth of the bottom zone, which has a warmer fluid than the top zone because the fluid temperature is at geothermal temperature.   In this situation, we have two possible interpretations from which the wellbore temperature profiles in both cases are identical.   One is that there is a casing leak in the bottom zone (left) where fluid enters the wellbore.   Since the temperature log is affected not only by the flow inside the casing but also by channel flow outside the casing, another possible interpretation is that the channeling liquid originates in a bottom zone and then enters the wellbore at the top zone (right).   To distinguish between the two possibilities, a spinner flowmeter is needed to check if there is flow inside the wellbore at the bottom zone.   If the flowing fluid enters the wellbore at the bottom zone, casing leak is the true interpretation.   On the other hand, if the flowmeter indicates that the flowing fluid does not enter the wellbore in the bottom zone, there must be an upward channel flow behind the casing and enters the well at the top zone.
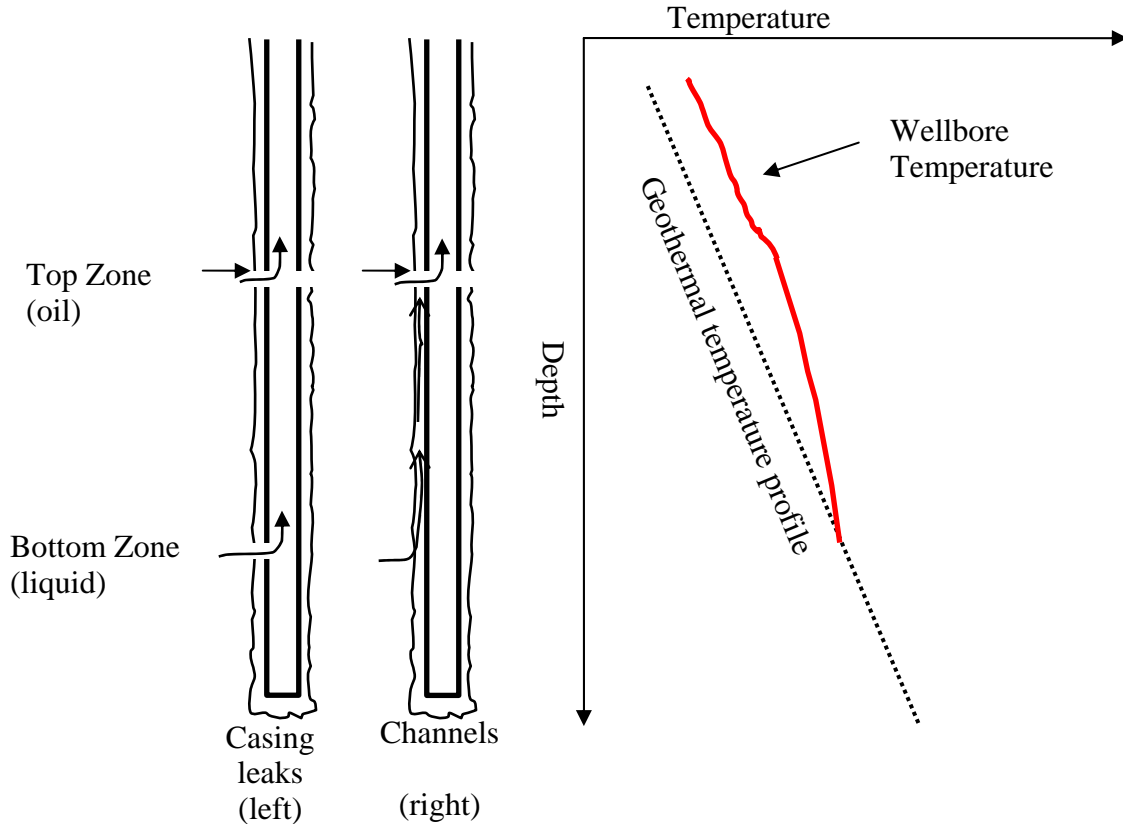
Figure 2.5   Application of a temperature log to detect casing leaks and channels.

2.1.3.4   Estimate flow rate

In a production well, fluid enters the wellbore at the geothermal temperature if the Joule-Thomson effect is neglected.   While the fluid flows up the well, it conductively loses thermal energy to the casing and surrounding formation.   As a result, the temperature profile of the flowing fluid is concave towards the geothermal temperature profile.   The temperature profile eventually approaches an asymptote parallel to the geothermal temperature profile as shown in Figure 2.6.

Quantitatively, such a temperature profile is described by Ramey's model (Ramey, 1962).   Ramey developed a model for an incompressible fluid based on the fact

that the heat is conducted radially away from the casing through the formation (i.e. fluid losing heat while flowing upward). The solution of the first-order differential equation with the boundary condition that $T_{well} = T_i$ at $D = 0$ gives

$$T_{well}(D,t) = T_G - g_G z + [T_i(t) + g_G z - T_b] e^{-D/z} \qquad (2.5)$$

where

$$z = q \frac{\rho C_p [K_{Tt} + f(t) r_w U_o]}{2\pi K_{Tt} r_w U_o}$$

$$f(t) = -\ln\left(\frac{r_{out}}{2\sqrt{\alpha t}}\right) - 0.29$$

$$\alpha = \frac{K_{Tt}}{\rho_{rock} C_{p,rock}}$$

q is flow rate

T_{well} is fluid wellbore temperature

T_G is geothermal temperature

T_i is temperature of fluid at surface ($D = 0$)

T_b is geothermal temperature at $D = 0$

g_G is geothermal temperature gradient

D is depth

U_o is overall heat-transfer coefficient

r_w is wellbore radius

r_{out} is radius at outside of the casing

ρ_{rock} is rock density

$C_{p,rock}$ is rock heat capacity

t is time

20

$f(t)$ given above is determined by applying line source/sink (constant heat flux) solution. z is a parameter proportional to flow rate, and thermal property of casing and surrounding formation. The asymptotic solutions of equation (2.5) is when D is large compared to z, $e^{-D/z}$ approaches zero; so equation (2.5) simplify to

$$T_w(D) = T_G(D) - g_z z$$

which means that the temperature curve becomes parallel to the geothermal temperature profile. As shown in Figure 2.6, the separation between the asymptotic portion of the temperature log and the geothermal temperature is mainly a function of flow rate. The purpose of reviewing this application is to show that it is possible to translate temperature measurement to flow rate profile in vertical wells.
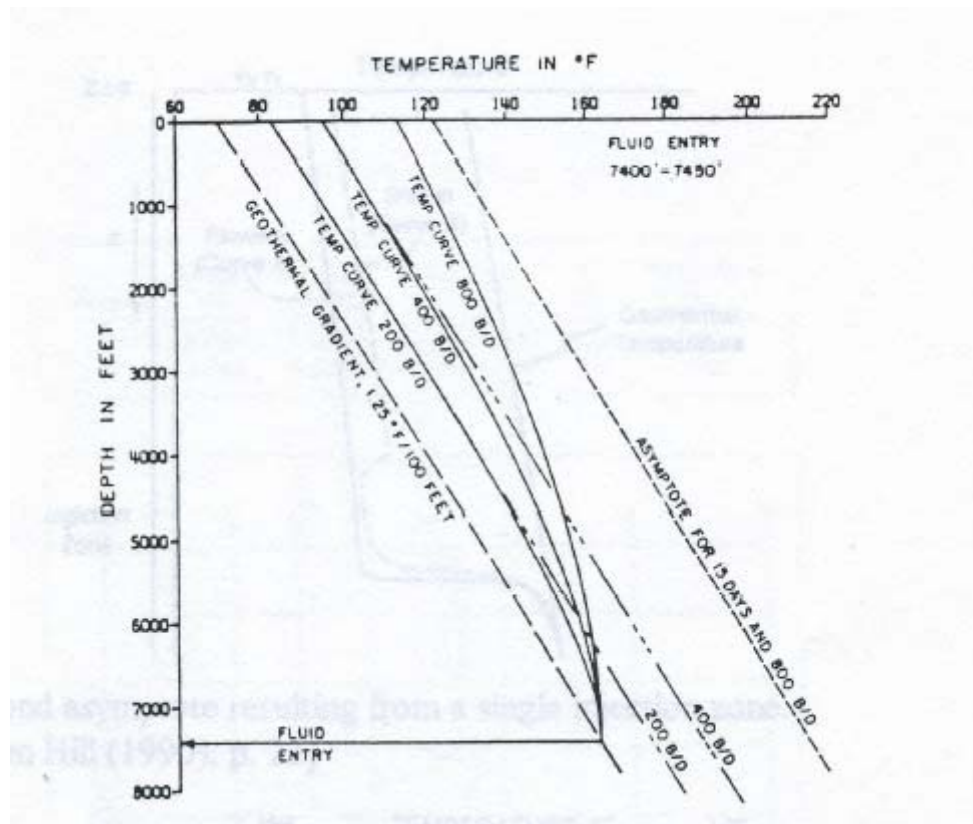
Figure 2.6   Application of temperature log to estimate flow rate. [From Curtis and Witterholt (1973)]

2.2   PRODUCTIVITY MODELS OF A HORIZONTAL WELL

Downhole temperature profiles of vertical wells are reasonably well understood, and are generally modeled using a radial geometry. In recent years, however, the widespread use of horizontal wells and attempts to continuously monitor horizontal wells by DTS has required that the knowledge from temperature logs be adapted to the horizontal well geometry. Chapters 3 and 4 will present the temperature model for relating temperature behavior to flow behavior, in which a productivity model that describes the pressure distribution in a reservoir is necessary to couple with an energy balance. This section is intended to introduce pressure-based productivity models for a

horizontal well. Many models have been proposed to evaluate the productivity of horizontal wells. Here we review only the models that are suitable for use in this study.

2.2.1 Model derived from sources and sinks

Originally, the method of instantaneous point source solution for solving heat conduction problems is presented by Carslaw and Jaeger (1959). Later, Gringarten *et al*. (1973) and Ouyang *et al*. (1998) applied it to fluid flow in reservoir. They used Green's functions (instantaneous source function) to solve the diffusivity equation, which is analogous to heat conduction equation. The plane, line, and point sources are used with Newman's product method to generate solutions for reservoir flow. The solution is general and can be applied to a single-phase flow in anisotropic reservoir and three-dimension flow. For example, if a horizontal well fully penetrates a box-shaped reservoir with infinite reservoir boundary in y-direction and no-flow boundaries in all others, the pressure drop between the well and any location in reservoir can be written in equation (2.6). The equation describes pressure field at any time. For steady-state flow, the solution can be simplified by using long time approximation $(t \rightarrow \infty)$.

$$\Delta p(y,z,y_{well},z_{well},t) = \frac{q}{\phi c_t L} \int_{\tau=0}^{\tau=t} S_y S_z d\tau \tag{2.6}$$

where

$$\Delta p = p(y,z,t) - p_{well}$$

$$S_y = \frac{1}{2\sqrt{\pi \eta_y \tau}} \exp\left[-\frac{(y-y_{well})^2}{4\eta_y \tau}\right]$$

$$S_z = \frac{1}{h}\left[1 + 2\sum_{n=1}^{\infty} \exp(-\frac{n^2 \pi^2 \eta_z \tau}{h^2})\cos(\frac{\pi z_{well}}{h})\cos(\frac{n\pi z}{h})\right]$$

23

$$\eta_y = \frac{k_y}{\phi c_t \mu}$$

$$\eta_z = \frac{k_z}{\phi c_t \mu}$$

Symbols are defined in the Nomenclature. The time variable τ is a dummy variable of integration. Although this solution is analytical for a simple reservoir geometry, it still requires a numerical integration of equation (2.6) to describe the pressure distribution in reservoir. Clearly, if we were to couple this solution with an energy balance that includes heat conduction and the Joule-Thomson effect, it would be as difficult as developing a numerical simulation. Since the purpose of the study is to develop a simple temperature model that could equivalently provide a means to assess the size of the temperature change in the reservoir and wellbore, we will use a more simple productivity model that can still serve the purpose. When we deal with two-phase and three-dimension flow in Chapter 4, we will develop a numerical simulation. The model derived from sources and sinks will not be used in this study. We present it here just for a comparison with other approaches.

2.2.2 Model derived from conformal mapping

Butler (1994) employs the mathematical technique called conformal mapping to solve the two-dimensional equation that describes a single-phase, steady-state flow in reservoir, as given below.

$$\frac{\partial^2 \Phi}{\partial y^2} + \frac{\partial^2 \Phi}{\partial z^2} = 0 \tag{2.7}$$

24
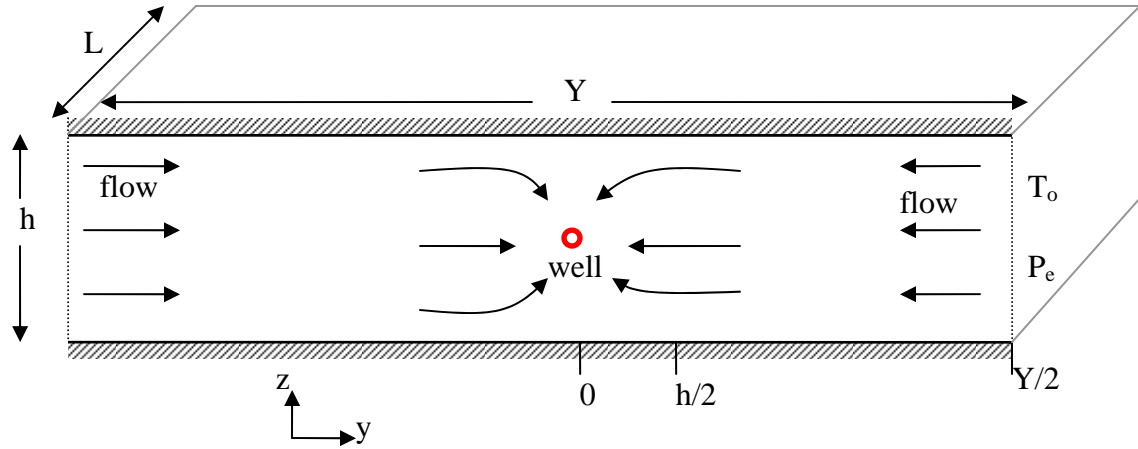
Figure 2.7   Sketch shows flow direction in y-z plane with no-flow upper and lower
boundaries.

where Φ is the flow potential, which is pressure if gravity is neglected.

Consider a two-dimensional reservoir of thickness h as shown in Figure 2.7. A production well at the center of the reservoir is producing at uniformly distributed rate along the well length, q/L.   As the geometry suggests, flow toward a horizontal well is two dimensional.   There is no flow in the x-direction (parallel to the well) because the well is fully penetrated through the center of the reservoir.   For an isotropic reservoir, the solution of equation (2.7) is

$$\Phi(y,z) = \frac{\mu}{4\pi k}\left(\frac{q}{L}\right)\ln\left(\cosh(\frac{2\pi y}{h}) - \cos(\frac{2\pi z}{h})\right) \tag{2.8}$$

where μ is fluid viscosity, k is permeability, h is reservoir thickness, L is well length, and q is production rate of the horizontal well.   The solution is illustrated in Figure 2.8, where we set $q/L = 5$ bbl/d/ft, $k = 50$ md, $h = 50$ ft, $\mu = 1$ cp, and

neglect gravity. The reservoir flow potential, $\Phi - \Phi_{well}$, is plotted on the vertical axis in which Φ_{well} is obtained by evaluating equation (2.8) at $y = r_w$, $z = 0$.
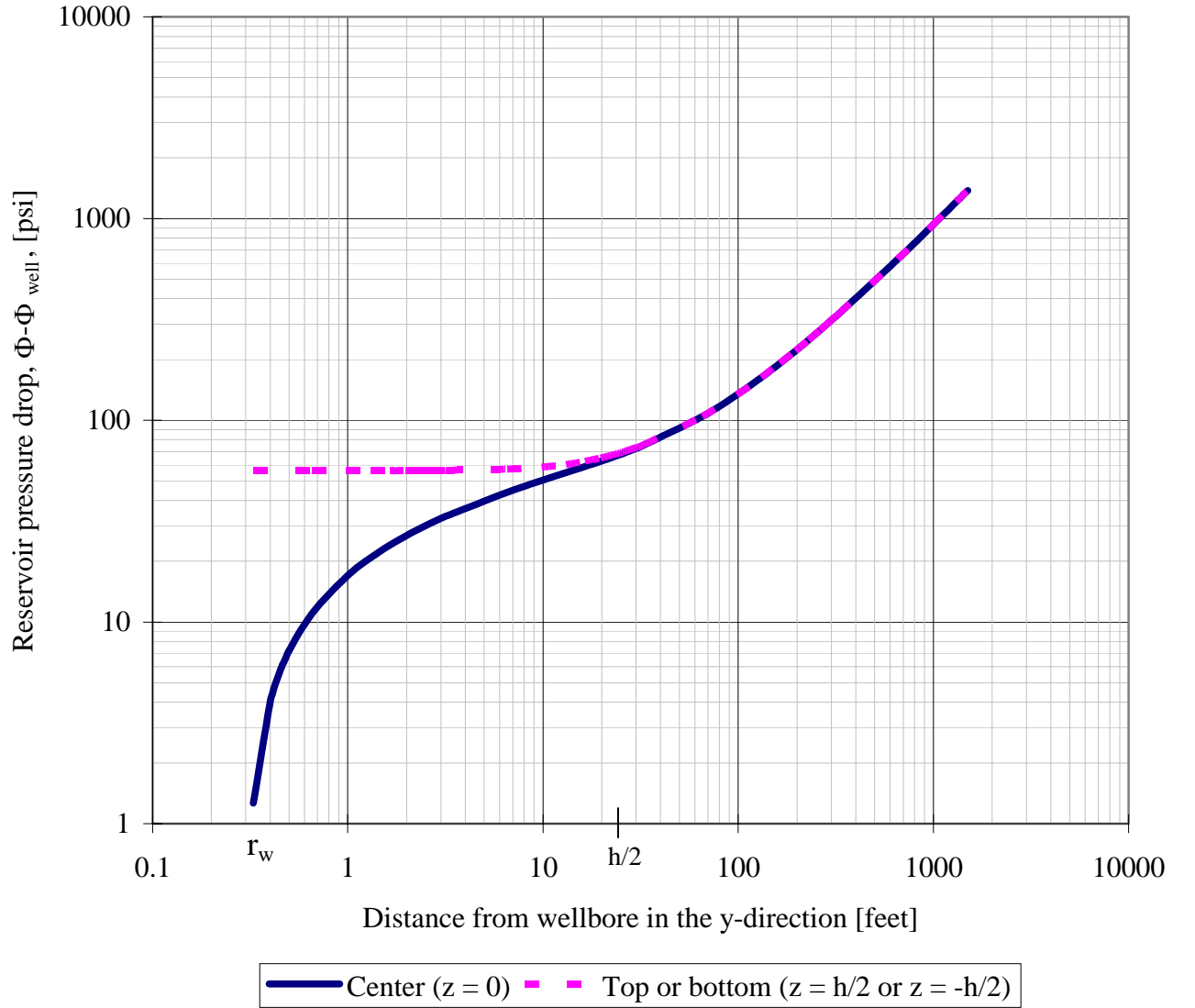
Figure 2.8   Illustration of the conformal mapping solution.

2.2.3   Model derived from simplifying the finite element result

In the same wellbore and reservoir flow geometry as conformal mapping model in Section 2.2.2, Furui *et al.* (2003) observed flow potential lines from a finite element simulation and found that we can approximate the pressure profile in the reservoir by a composite of one-dimensional radial flow near the well and one-dimensional linear flow farther from the well.   Therefore, the pressure profile in reservoir can be simply calculated by equation (2.9) and (2.10).

Radial flow region:

$$\Phi(y,z) = \frac{\mu}{2\pi k}\left(\frac{q}{L}\right)\ln\left(\frac{\sqrt{y^2+z^2}}{r_w}\right) \quad , \text{ for } \ r_w \le \sqrt{y^2+z^2} \le \frac{h}{2} \qquad (2.9)$$

Linear flow region:

$$\Phi(y,z) = \frac{\mu}{2\pi k}\left(\frac{q}{L}\right)\ln\left(\frac{h/2}{r_w}\right) + \frac{\mu}{kh}\left(\frac{q/2}{L}\right)\left(y-\frac{h}{2}\right) \quad , \text{ for } \ y > \frac{h}{2} \ \text{ or } \ y < -\frac{h}{2} \qquad (2.10)$$

This radial-linear composite model is verified by plotting its solution against the analytical model (conformal mapping model) as shown in Figure 2.9   The input parameters used to plot the graph here are the same as the ones used in Section 2.2.2 for a fair comparison.   Figure 2.9   shows that pressure profiles for both models agree at every location in the reservoir.

The fundamental advantage of equations (2.9) and (2.10) is that they represent a two-dimensional flow by two one-dimensional flows.   As a result, we are able to analytically solve a complex energy balance that includes subtle energy changes.   Later in Chapter 3, we will develop an inflow temperature model based on this flow model.
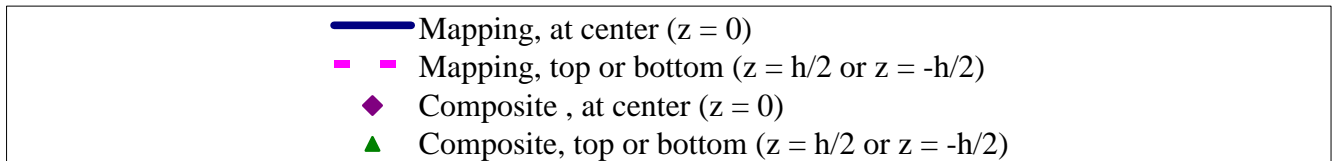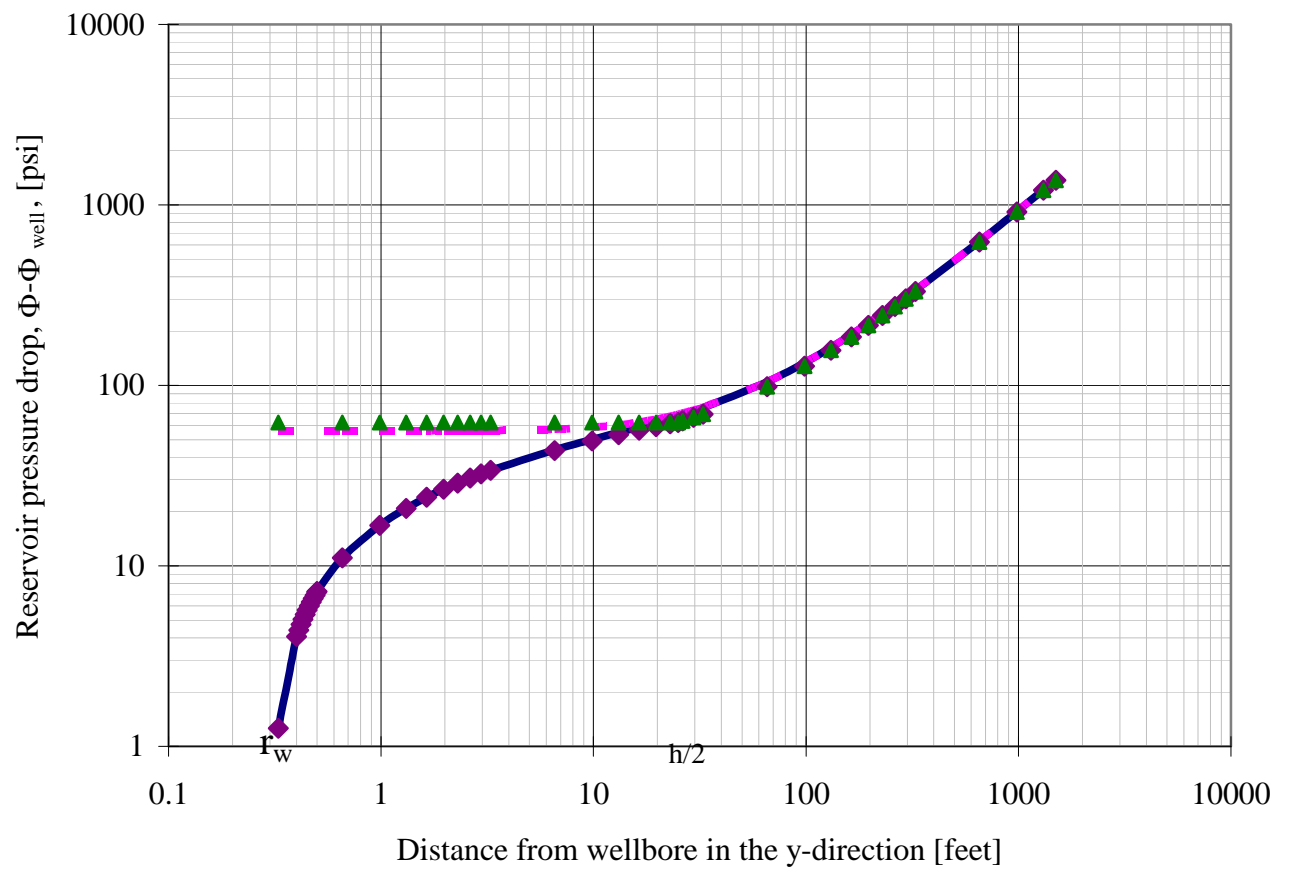
Figure 2.9   Comparison of the conformal mapping model and the radial-linear
             composite model.

2.3 NON-ISOTHERMAL WELLBORE FLOW MODEL

For a vertical well, it is reasonable to assume that the pressure drop caused by friction along the producing section of the well is negligible. This is mainly because the length of the well that is in contact with the reservoir is short and an inconsiderable pressure drop is expected in such short wellbore within the practical ranges of vertical well production rates. For a horizontal well, neglecting the influence of long wellbore pressure drop could lead to an error in estimating the inflow rate distribution along the wellbore. A larger pressure drop in the wellbore imposes more inflow from the reservoir. Because of the pressure drop along the horizontal wellbore, the temperature of flowing fluid will change, caused mainly by the Joule-Thomson effect and the mixing of inflow temperature feeding into a wellbore .

To predict temperature inside the wellbore, we will couple an inflow temperature model with a non-isothermal wellbore flow model developed by Yoshioka *et al*. (2004). There are two main considerations in the model. First, the model includes mass and heat transfer from the reservoir inflow and flow along the wellbore axis (x-direction). Second, the model takes into account subtle energy changes; so the temperature changes caused by Joule-Thomson effect is included.

Yoshioka *et al*. (2004) and Yoshioka (2007) derived the pressure drop along the wellbore from conservation of mass and momentum under steady-state flow. Consider a wellbore that produces fluids from a reservoir as shown in Figure 2.10.
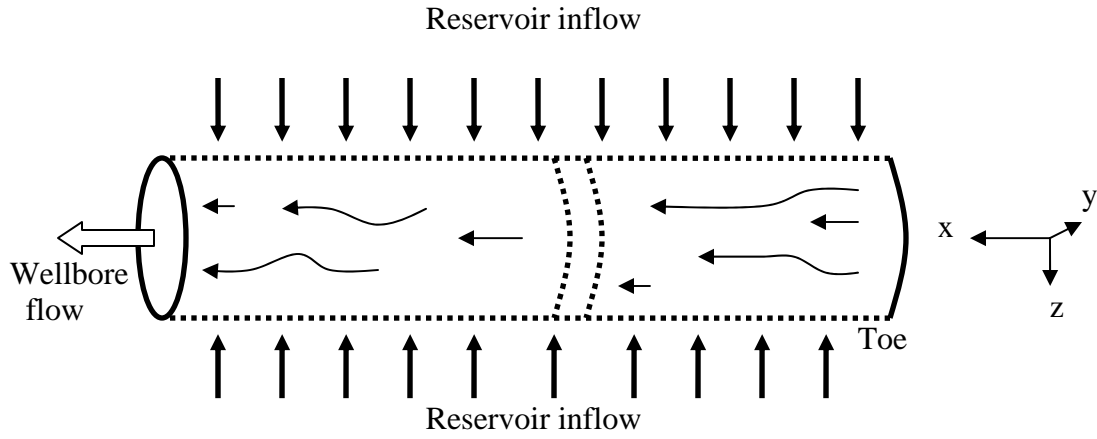
Figure 2.10   Schematic of wellbore flow and reservoir inflow.

The wellbore flow has to take into account multi-phase flow because the inflowing fluid can be any phase (gas, oil, or water) or mixtures thereof.   Thus, the mass and momentum balances are equation (2.11) and (2.12).

$$-\pi r_w^2 \frac{d}{dx}(\rho_l v_l y_l) + 2\pi r_w (\rho_l v_l)_I = 0 \qquad (2.11)$$

$$-\frac{\rho_m f_m v_m^2}{r_w} - \frac{d}{dx}(\rho_m v_m^2 + p) - \rho_m g \sin\theta = 0 \qquad (2.12)$$

where

$$\rho_m = \sum_{l=1}^{Np} \rho_l y_l \;\; , and \quad v_m = \frac{\displaystyle\sum_{l=1}^{Np} \rho_l v_l y_l}{\displaystyle\sum_{l=1}^{Np} \rho_l y_l}$$

30

the subscript l denotes the phases, and subscript I denotes an inflowing fluid quantity. Then v_l is a velocity of phase l in wellbore. $(v_l)_I$ is an inflow velocity of phase l. The subscript m in the momentum equation denotes a mixture of all phases. The wellbore pressure (p) is assumed to be the same for each phase. y_l is the volume fraction of phase l (i.e. the holdup of the phase). The notation is defined in the Nomenclature.

The result of combining the mass and momentum balance is a differential equation that describes the pressure drop along the wellbore.

$$\frac{d\,p_{well}}{d\,x} = -\frac{\rho_m v_m^2 f_m}{r_w} - \frac{d}{dx}(\rho_m v_m^2) - \rho_m g \sin\theta \qquad (2.13)$$

The first term of the right side is the pressure drop caused by friction in wellbore. The second term is the pressure drop caused by acceleration of the flowing fluid. The third term is the pressure drop caused by gravity.

Correlation of friction factor for this homogeneous model (no slip velocity between phases) is expressed in term of Reynolds number. Reynolds number for mixture and for inflow wall are defined as

$$N_{Re,w} = \frac{\rho_{m,I} v_{m,I} (2r_w)}{\mu_{m,I}}$$

$$N_{Re} = \frac{\rho_m v_m (2r_w)}{\mu_m}$$

where

$$\mu_m = \sum_{l=1}^{N_p} y_l \mu_l$$

31

For larminar flow,

$$f_m = f_o \left(1 - 0.04304\, N_{Re,w}^{0.6142}\right)$$

and

$$f_o = \frac{16}{N_{Re}}$$

For turbulent flow in an open-hole wellbore,

$$f_m = f_o \left[1 - 29.03 \left(\frac{N_{Re,w}}{N_{Re}}\right)^{0.8003}\right]$$

and

$$f_o = \left[-4\log\left\{\frac{\varepsilon}{3.7065} - \frac{5.0452}{N_{Re}}\log\left[\frac{\varepsilon^{1.1098}}{2.8257} + \left(\frac{7.149}{N_{Re}}\right)^{0.8981}\right]\right\}\right]^{-2}$$

Yoshioka *et al.* (2004) and Yoshioka (2007) also derived a differential equation that describes the temperature along wellbore. The final form of the temperature equation is

$$\frac{dT}{dx} = \frac{2(\rho v C_p)_{T,I}}{r_w (\rho v C_p)_T}\left(T_I - T_{well}\right) + \frac{(\rho v C_p C_{JT})_T}{(\rho v C_p)_T}\frac{dp_{well}}{dx} + \frac{(\rho v)_T}{(\rho v C_p)_T} g\sin\theta \qquad (2.14)$$

where

$$(\rho v)_T = \sum_{l=1}^{N_p} \rho_l v_l y_l$$

$$(\rho v C_p)_T = \sum_{l=1}^{N_p} \rho_l v_l y_l C_{p,l}$$

$$(\rho v C_p C_{JT})_T = \sum_{l=1}^{N_p} \rho_l v_l y_l C_{p,l} C_{JT,l}$$

The first term on the right side of equation (2.14) is the heat exchange between the wellbore and reservoir caused by convection of inflow and wellbore flows. The second term is the temperature change in the wellbore caused by the Joule-Thomson effect. The third term is the temperature change in a wellbore caused by gravity.

These three equations (2.11, 2.13, 2.14) are solved numerically by discretizing the equations with finite differences. The solution procedures are as follows.

1. Make an initial guess for pressure and temperature along the wellbore
2. Obtain the velocity profile from equation (2.11).
3. Calculate the temperature profile from equation (2.14).
4. Calculate the pressure profile from equation (2.13).
5. Test for convergence of temperature and pressure profiles.

The procedures are repeated until the pressure and temperature converge. To help convergence, the initial guess should be estimated by the analytical solution discussed in Chapter 3.

CHAPTER   3

Analytical Temperature Model

The analytical temperature model presented in this chapter couples reservoir inflow with wellbore flow.   For reservoir inflow, mass and energy balances are solved along with Darcy's Law.   The wellbore model previously presented in Section 2.3 solves mass, energy and momentum balances.   The coupled model will provide a means to assess the size of a temperature change caused by the subtle thermal energy such as the Joule-Thomson effect and heat conduction.   Only a steady-state temperature model is developed in this chapter.   The derivation of an inflow temperature model will be presented in detail, wherein the necessary assumptions are stated along with the derivation.   Furthermore, we do sensitivity studies with the model to illustrate the flow conditions that cause measurable temperature changes or anomalies that could be recognized in an analysis of distributed temperature measurements.

3.1 GEOMETRY OF THE MODEL

Although horizontal wells have many bends and curves with local inclinations over 80 degrees from the vertical, we have modeled the well as a straight horizontal because we aim to investigate how big is the temperature change caused by the thermal energy resulting from fluid expansion, viscous dissipation, and heat conduction.   Since the wellbore does not change with elevation, it means that we have excluded the effects of the gravity and the geothermal temperature on the pressure and temperature profiles.

The inflow temperature model is developed based on the geometry sketched in Figure 3.1.   A horizontal well is modeled as an open hole drilled fully through a boxed-shape reservoir with no-flow boundaries on the top and bottom of the reservoir.   In an

isotropic reservoir, the flow is likely to be radial near the well and linear far from the well. Knowing that, we can simplify the flow region into two composite systems composed of radial flow from $y = r_w$ to $y = h/2$ and linear flow from $y = h/2$ to $y = Y/2$ (Furui *et al.*, 2002). This flow model describes the reservoir pressure distribution in the two-dimensional plane (y-z plane) as illustrated in Figure 2.9 although it is based on a composite of one-dimensional flows. Since the horizontal well is fully penetrating in the x-direction, the reservoir flow in the x-direction is assumed to be small and negligible.
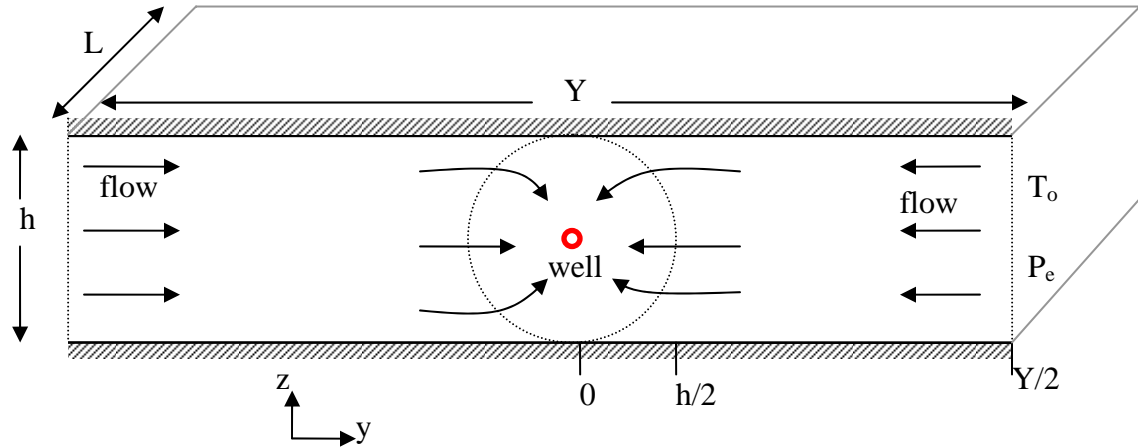
Figure 3.1   A reservoir segment shows the flow direction into wellbore at the center. Inside the circle is a radial flow region and outside is a linear flow region.

With this simple flow geometry, an energy balance can be solved analytically for a single-phase flow under steady-state conditions. The inflow temperature model resulting from solving the energy balance will provide a means to relate temperature profiles to flow rates and the type of fluid entering the wellbore. If we did not include the thermal energy, such as the Joule-Thomson effect in the energy balance, the inflow

temperature of the entering fluid would be the same as the geothermal temperature; then there would be no way to translate the temperature profiles to flow behavior.

We consider a reservoir segment containing a well section in the center. Each reservoir segment produces a single-phase fluid, but multi-phase flow appears in the wellbore as a result of the mixing of single-phase flows of different phases from the reservoir segments. Figure 3.2 illustrates the geometry of the model. With this multi-segmented reservoir technique, we model a typical horizontal well that is thousands of feet long, where some horizontal sections can be producing oil, water, or gas.
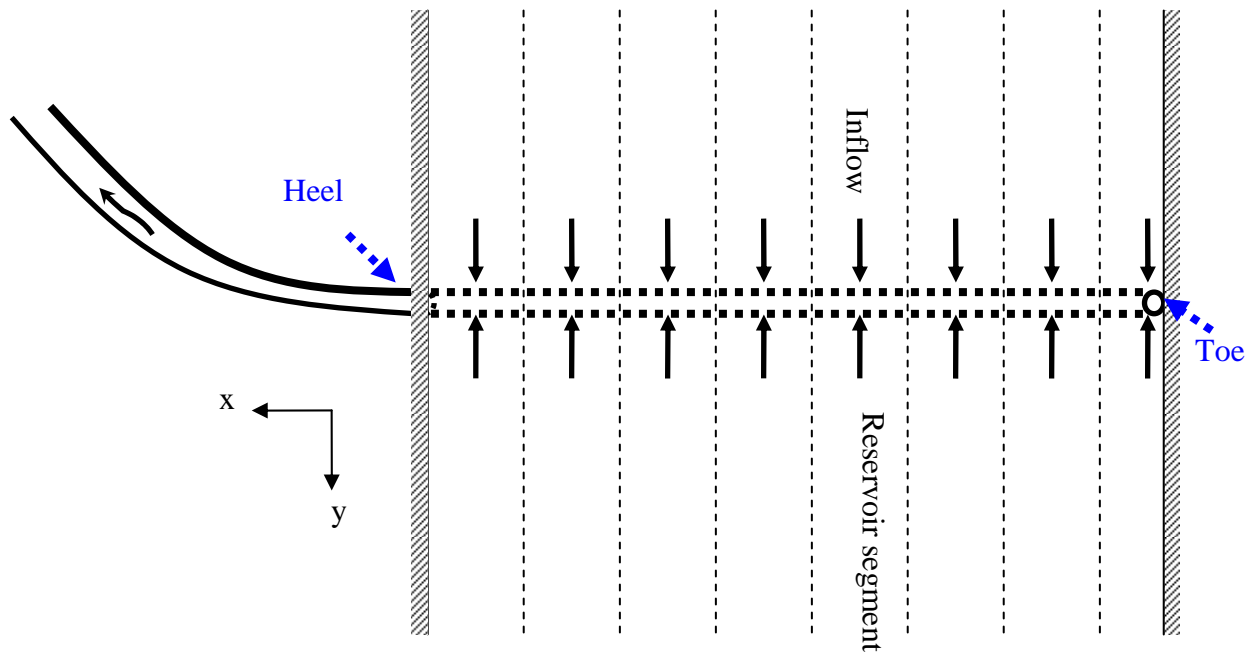
Figure 3.2 Geometry of the model shows the combination of multi-segmented reservoirs containing a horizontal wellbore at the center.

36

3.2 DERIVATION OF GOVERNING EQUATIONS FOR FLOW IN RESERVOIR

The fundamental equations describing fluid flow in a reservoir are mass balances, Darcy's law, and energy balance. These equations are very general and used in many engineering applications. They are discussed and formulated to fit the scope of this study.

3.2.1 Mass balance

A starting point for studying fluid flow is the mass balance. It is the conservation of mass that transports through a unit area in unit time. By understanding the mechanisms of mass flow, we can infer the velocity or pressure distribution of the fluid in a reservoir. The velocity or pressure distribution is then coupled with the energy equation to obtain temperature profiles in the reservoir.

The general form of the mass balance that can apply directly to fluid flow in permeable media for any number of components, phases, and chemical reactions is explained in Chapter 2 of Lake (1989). It is simplified here for single phase and steady-state flow condition.

$$\vec{\nabla} \cdot \left(\rho \vec{u} \right) = 0 \tag{3.1}$$

where the velocity $\vec{u}$ is defined by Darcy's Law.

$$\vec{u} = -\frac{\vec{\vec{k}}}{\mu} \cdot (\vec{\nabla} p + \rho \vec{g})$$

The mass balance is typically expressed in terms of pressure by substituting Darcy's Law into equation (3.1). For isotropic permeable media with negligible gravity, this equation become

$$\bar{\nabla}^2 p + c \left(\bar{\nabla} p \right)^2 = 0 \tag{3.2}$$

where c is the compressibility of the fluid. For slightly compressible fluid, the term $c \left(\bar{\nabla} p \right)^2$ is negligible because both the compressibility and the pressure squared gradient are small.

3.2.2 Energy balance

In production and reservoir engineering, the temperature change caused by the heat that is generated by fluid flow is commonly ignored because this type of heat is relatively small and only slightly affects the flowing fluid properties. So assuming isothermal flow in the reservoir is suitable when the focus is on the amount of production. However, this study does not assume isothermal flow in reservoir because the focus is on the meaning of temperature related to flows. Thus, the small temperature change resulting from fluid expansion, viscous dissipation, and heat conduction are to be investigated. One of the interests of this study is to solve the energy balance to predict temperature profiles, so it is necessary to understand the derivation of thermal energy balance.

A brief derivation of the thermal energy balance is presented here. Rigorous detail is presented in Bird *et al.* (2002) and Sandler (1999). Note that the notation $\bar{v}$ is an interstitial velocity and $\bar{u}$ is a superficial velocity, also known as the Darcy velocity for flow in permeable media. First, start from the momentum balance on the flowing fluid.

$$\frac{\partial}{\partial t}(\rho\vec{v}) = -\left[\vec{\nabla}\cdot\rho\vec{v}\vec{v}\right] - \vec{\nabla}p - \left[\vec{\nabla}\cdot\vec{\vec{\tau}}\right] + \rho\vec{g} \qquad (3.3)$$

The momentum is usually viewed as a force, thus; multiplying force by velocity gives the mechanical energy. Knowing that, we can take the dot product of the velocity vector, $\vec{v}$, with the momentum balance in equation (3.3). The result is the mechanical energy balance shown in equation (3.4).

$$\frac{\partial}{\partial t}\left(\frac{1}{2}\rho v^2\right) = -\vec{\nabla}\cdot\left(\frac{1}{2}\rho v^2\vec{v}\right) - \vec{\nabla}\cdot(p\vec{v}) - p\left(-\vec{\nabla}\cdot\vec{v}\right) - \vec{\nabla}\cdot\left[\vec{\vec{\tau}}\cdot\vec{v}\right] - \left(-\vec{\vec{\tau}}:\vec{\nabla}\vec{v}\right) + \rho(\vec{v}\cdot\vec{g})$$

$$(3.4)$$

The general form of the total energy balance includes kinetic energy, internal energy, heat conduction, work done on the flowing fluid by pressure forces, external forces (gravity) and viscous forces. This total energy balance can be written below.

$$\frac{\partial}{\partial t}\left(\frac{1}{2}\rho v^2 + \rho U\right) = -\vec{\nabla}\cdot\left((\frac{1}{2}\rho v^2 + \rho U)\vec{v}\right) + \vec{\nabla}\cdot\left(K_T\vec{\nabla}T\right) - \vec{\nabla}\cdot(p\vec{v}) - \vec{\nabla}\cdot\left[\vec{\vec{\tau}}\cdot\vec{v}\right] + \rho(\vec{v}\cdot\vec{g})$$

$$(3.5)$$

In this study, we are interested in the temperature of the flowing fluid. Subtracting the mechanical energy balance in equation (3.4) from the total energy balance in equation (3.5), to yield the thermal energy balance from which temperature of fluid can be obtained.

$$\frac{\partial}{\partial t}(\rho U) = -\vec{\nabla}\cdot(\rho U\vec{v}) + \vec{\nabla}\cdot\left(K_T\vec{\nabla}T\right) - p\left(\vec{\nabla}\cdot\vec{v}\right) + \left(-\vec{\vec{\tau}}:\vec{\nabla}\vec{v}\right) \qquad (3.6)$$

Equation (3.6) is one of the most useful forms of the microscopic energy balance in engineering thermodynamics and fluid mechanics. The left side describes the accumulation of internal energy per unit volume. The transport terms on the right side are the internal energy changes caused by convection, conduction, fluid expansion, and viscous dissipation, respectively. For steady-state flow, the time derivative is dropped. The equation is in the following form.

$$\vec{\nabla} \cdot (\rho U \vec{v}) + p(\vec{\nabla} \cdot \vec{v}) - \vec{\nabla} \cdot (K_T \vec{\nabla} T) - (-\bar{\bar{\tau}} : \vec{\nabla} \vec{v}) = 0 \tag{3.7}$$

To express the thermal energy balance in terms of measurable (sensible) quantities (p, T), we substitute the definition of enthalpy, which is $H = U + \dfrac{p}{\rho}$, into the equation. The equation becomes

$$\vec{\nabla} \cdot (\rho \vec{v} H) - \vec{\nabla} \cdot (p \vec{v}) + p(\vec{\nabla} \cdot \vec{v}) - \vec{\nabla} \cdot (K_T \vec{\nabla} T) - (-\bar{\bar{\tau}} : \vec{\nabla} \vec{v}) = 0 \tag{3.8}$$

The first term includes the enthalpy, which, expanded by using the mass balance for steady-state flow, which is $\vec{\nabla} \cdot (\rho \vec{v}) = 0$ and yields $\rho \vec{v} = \text{constant}$

$$\rho \vec{v} \cdot \vec{\nabla} H - \vec{\nabla} \cdot (p \vec{v}) + p(\vec{\nabla} \cdot \vec{v}) - \vec{\nabla} \cdot (K_T \vec{\nabla} T) - (-\bar{\bar{\tau}} : \vec{\nabla} \vec{v}) = 0 \tag{3.9}$$

The following steps show the rearrangement of terms that relate the enthalpy to the pressure and temperature using thermodynamic relationships.

$$\rho \vec{v} \cdot \left\{ \left[\left(\frac{\partial H}{\partial p} \right)_T \vec{\nabla} p + \left(\frac{\partial H}{\partial T} \right)_p \vec{\nabla} T \right] \right\} - \vec{\nabla} \cdot (p \vec{v}) + p(\vec{\nabla} \cdot \vec{v}) - \vec{\nabla} \cdot (K_T \vec{\nabla} T) - (-\bar{\bar{\tau}} : \vec{\nabla} \vec{v}) = 0$$

Substituting the definition of C_p and Maxwell's relation of thermodynamics in the first term of the left side yield

$$\rho\vec{v}\cdot\left\{\left[V-T\left(\frac{\partial V}{\partial T}\right)_p\right]\vec{\nabla}p+C_p\vec{\nabla}T\right\}-\vec{\nabla}\cdot(p\vec{v})+p(\vec{\nabla}\cdot\vec{v})-\vec{\nabla}\cdot\left(K_T\vec{\nabla}T\right)-(-\bar{\bar{\tau}}:\vec{\nabla}\vec{v})=0$$

Substitute the definition of a thermal expansion coefficient (β), and replace the specific volume (V) with the reciprocal of density ($1/\rho$).

$$\rho\vec{v}\cdot\left\{\left[\frac{1}{\rho}-\frac{\beta T}{\rho}\right]\vec{\nabla}p+C_p\vec{\nabla}T\right\}-\vec{\nabla}\cdot(p\vec{v})+p(\vec{\nabla}\cdot\vec{v})-\vec{\nabla}\cdot\left(K_T\vec{\nabla}T\right)-(-\bar{\bar{\tau}}:\vec{\nabla}\vec{v})=0$$

where β is a thermal expansion coefficient defined as $\beta=-\frac{1}{\rho}\left(\frac{\partial\rho}{\partial T}\right)_p=\frac{1}{V}\left(\frac{\partial V}{\partial T}\right)_p$.

Expand the terms in the bracket.

$$\rho C_p\left(\vec{v}\cdot\vec{\nabla}T\right)-\beta T\left(\vec{v}\cdot\vec{\nabla}p\right)+\vec{v}\cdot\left(\vec{\nabla}p\right)-\vec{\nabla}\cdot(p\vec{v})+p(\vec{\nabla}\cdot\vec{v})-\vec{\nabla}\cdot\left(K_T\vec{\nabla}T\right)-(-\bar{\bar{\tau}}:\vec{\nabla}\vec{v})=0$$

The third, fourth, and fifth terms cancel out, and the equation becomes

$$\rho C_p\left(\vec{v}\cdot\vec{\nabla}T\right)-\beta T\left(\vec{v}\cdot\vec{\nabla}p\right)-\vec{\nabla}\cdot\left(K_T\vec{\nabla}T\right)-(-\bar{\bar{\tau}}:\vec{\nabla}\vec{v})=0 \qquad (3.10)$$

where $\left(-\bar{\bar{\tau}}:\vec{\nabla}\vec{v}\right)$ can be expressed in Cartesian coordinates as

$$\left(\bar{\bar{\tau}} : \nabla \vec{v}\right) = \tau_{xx} \frac{\partial v_x}{\partial x} + \tau_{xy} \frac{\partial v_x}{\partial y} + \tau_{xz} \frac{\partial v_x}{\partial z}$$

$$+ \tau_{yx} \frac{\partial v_y}{\partial x} + \tau_{yy} \frac{\partial v_y}{\partial y} + \tau_{yz} \frac{\partial v_y}{\partial z}$$

$$+ \tau_{zx} \frac{\partial v_z}{\partial x} + \tau_{zy} \frac{\partial v_z}{\partial y} + \tau_{zz} \frac{\partial v_z}{\partial z}$$

The $\left(-\bar{\bar{\tau}} : \nabla \vec{v}\right)$ term is the viscous dissipation heating that describes the irreversible degradation of mechanical energy into thermal energy. It is too complicated to solve for directly. The research and discussion on it is ongoing. This term is sometimes viewed as an entropy generation in thermodynamics, which means that it is always positive (heating) for a Newtonian fluid. For special fluids, the term can be negative because some energy may be stored as elastic energy (Bird *et al*., 2002).

$\left(-\bar{\bar{\tau}} : \nabla \vec{v}\right)$ is commonly substituted by $\left(-\vec{u} \cdot \nabla p\right)$ for a flow governed by Darcy's law; see Ingham *et al*. (1990) and Al-Hadhrami *et al*. (2002) for details. This substitution makes equation (3.10) become a complete energy balance of steady-state flow.

In permeable media, the fluid velocity, $\vec{v}$, is replaced by the Darcy velocity, $\frac{\vec{u}}{\phi}$. And, the heat conductivity is the effective heat conductivity, K_{Tt}, which combines both fluid and rock conductivity. Empirical expressions for K_{Tt} can be found in the literature (Lake, 1989). For a fluid-filled consolidated sandstone, an example expression is

$$K_{Tt} = K_d \left\{ 1 + 0.299 \left[\left(\frac{K_{fl}}{K_a}\right)^{0.33} - 1 \right] + 4.57 \left[\frac{\phi K_{fl}}{(1-\phi)K_d} \right]^{0.482} \left[\frac{\rho}{\rho_s} \right]^{-4.30} \right\}$$

where the subscripts t, f, a, and d refer to total, fluid, air and dry respectively. K_{Tt} depends weakly on temperature and is treated as a constant here. The main assumption is that the temperature of flowing fluid is identical to the temperature of the rock. This assumption is valid for continuous flow (steady-state) because changes in a flow rate are much slower than the response time of any sensor. Finally, the equation becomes,

$$\rho C_p\left(\bar{u}\cdot\bar{\nabla}T\right)-\beta T\left(\bar{u}\cdot\bar{\nabla}p\right)-\bar{\nabla}\cdot\left(K_{Tt}\bar{\nabla}T\right)+\bar{u}\cdot\bar{\nabla}p=0 \tag{3.11}$$

The first term is thermal energy transported by convection. The second term is thermal energy (cooling) caused by fluid expansion. The third term is thermal energy by heat conduction, and the last term represents viscous dissipation. The heat conduction term, $\bar{\nabla}\cdot\left(K_{Tt}\bar{\nabla}T\right)$, makes equation (3.11) become a second-order differential equation. Equation (3.11) is going to be used to describe the temperature of non-isothermal flow in reservoir.

If we were to use the energy equation (3.11) to describe the Joule-Thomson experiment, which is a steady-state isenthalpic process with no heat conduction, we would arrive at

$$\rho C_p\left(\bar{u}\cdot\bar{\nabla}T\right)-\beta T\left(\bar{u}\cdot\bar{\nabla}p\right)+\bar{u}\cdot\bar{\nabla}p=0 \tag{3.12}$$

All of the terms are products of $\bar{u}$, so the equation can be rearranged as

$$\bar{u}\cdot\left(\rho C_p\bar{\nabla}T+\bar{\nabla}p-\beta T\bar{\nabla}p\right)=0$$

43

If $\bar{u}$ is not zero, we can divide both sides by $\bar{u}$. The equation becomes

$$\bar{\nabla}T = \left(\frac{\beta T - 1}{\rho C_p}\right)\bar{\nabla}p$$

The term $\dfrac{\beta T - 1}{\rho C_p}$ is the Joule-Thomson coefficient, C_{JT}. This is a well-known

relationship that describes the change in temperature of a fluid upon expansion in a

steady-state flow with neither heat nor work done on the system. An example of this

kind of process is a flow through an expansion valve illustrated in Figure 3.3 . Thus, we

can fairly conclude that the governing equation (3.11) includes the Joule-Thomson effect.

$$T_1 , p_1 \qquad\qquad H_1 = H_2 \qquad\qquad p_2 , T_2 = ?$$
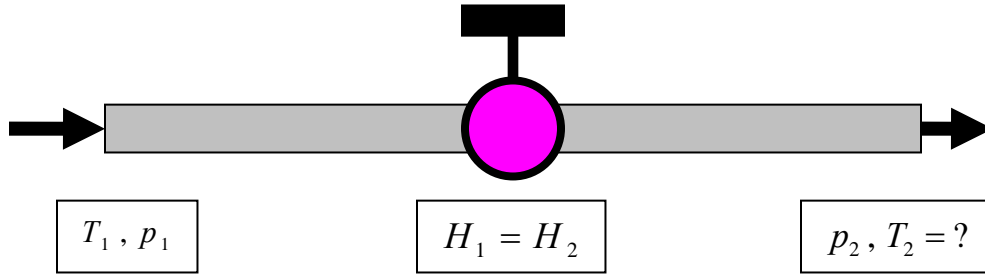
Figure 3.3   Sketch shows a flow through an expansion valve.

The meaning of equation (3.12) is that there are two main causes of thermal

energy change; fluid expansion, $\beta T\left(-\bar{u}\cdot\bar{\nabla}p\right)$, and viscous dissipation, $\left(-\bar{u}\cdot\bar{\nabla}p\right)$. Note

that the term $\left(-\bar{u}\cdot\bar{\nabla}p\right)$ is always positive. For most gases, $\beta T\left(-\bar{u}\cdot\bar{\nabla}p\right)$ is greater

44

than $\left(-\bar{u} \cdot \bar{\nabla} p\right)$, and the temperature of a flowing gas decreases. On the other hand, if $\left(-\bar{u} \cdot \bar{\nabla} p\right)$ is greater than $\beta T\left(-\bar{u} \cdot \bar{\nabla} p\right)$, the temperature of a flowing liquid increases. If there is no change in pressure or $\beta T\left(-\bar{u} \cdot \bar{\nabla} p\right) = \left(-\bar{u} \cdot \bar{\nabla} p\right)$ such as a flow of ideal gas (i.e. low pressure gas) in which $\beta = \dfrac{1}{T}$, the temperature of a fluid is constant.

It should be emphasized that the thermal energy balance can only be simplified to describe the Joule-Thomson effect if we model the viscous dissipation, $(-\bar{\bar{\tau}} : \bar{\nabla} v)$, as $\left(-\bar{u} \cdot \bar{\nabla} p\right)$ and $\bar{u}$ is not zero. For example, if we modeled that $(-\bar{\bar{\tau}} : \bar{\nabla} v) = a\left(-\bar{u} \cdot \bar{\nabla} p\right)$ where a is a constant, the equation (3.12) could not be simplified to the Joule-Thomson coefficient.

3.3 APPROXIMATE TEMPERATURE MODEL

The governing equations both for reservoir and wellbore flows are highly non-linear, so it is important to initially estimate a wellbore temperature profile that is close to the right solution. Later in Section 3.4, we present an iteratively coupled temperature model. In this section, we only present how to obtain the approximate wellbore temperature profile.

A wellbore temperature profile can be approximated by assuming that the wellbore flow does not affect the reservoir flow; in other words, wellbore and reservoir flows are decoupled. With this assumption and the geometry of the model discussed in Section 3.1, we can analytically solve the governing equations for the inflow temperature of the fluid in each reservoir segment. Once the inflow temperature is known, the mixing temperature inside the wellbore can be explicitly calculated from the non-isothermal wellbore flow model presented in Section 2.3.

3.3.1 Analytical inflow temperature model of a reservoir segment

We first develop an analytical inflow temperature model of a reservoir segment as shown in Figure 3.1. Since the energy balance presented in Section 3.2 is a second-order differential equation and the flow geometry is a composite of radial and linear flows, we need four boundary conditions. They are

1) Temperature is finite at the center of the well.

$$T = finite, \quad as \quad r \to 0$$

2) Temperature is continuous at the transition between radial and linear flows.

$$(T)_{y=h/2} = (T)_{r=h/2}$$

3) Heat flux is continuous at the transition between radial and linear flows.

$$\left(\frac{dT}{dy}\right)_{y=h/2} = \left(\frac{dT}{dr}\right)_{r=h/2}$$

4) Geothermal temperature at the external reservoir boundary is known.

$$(T)_{y=Y/2} = T_o$$

3.3.1.1 Analytical inflow temperature model

With the flow geometry shown in Figure 3.1, mass and energy balances are solved by employing the boundary condition that temperature is finite as the fluid flows to the center of the wellbore ($r = 0$), but the inflow temperature is actually evaluated at the sandface where $r = r_w$. Physically this means that both mass and energy fluxes are constantly feeding to a wellbore. Once fluid enters a wellbore, it is isolated from the reservoir. This is an approximation where the wellbore flow does not lose/gain conductive heat through the wellbore wall. The rest of boundary conditions were stated below.

46

Consider steady-state radial flow near the wellbore region as discussed in Section 3.1. The pressure relationship is described by Darcy's law

$$u_r = -\frac{k}{\mu}\frac{dp}{dr} \tag{3.13}$$

Equation (3.13) can be expressed in terms of a flow rate as

$$\frac{q}{2\pi r L} = -\frac{k}{\mu}\frac{dp}{dr} \tag{3.14}$$

In this study, the reservoir pressure described by equation (3.14) at a constant flow rate is used for both slightly compressible fluid (oil/water) flow and a high pressure gas flow. The cutoff point of this high pressure gas is about 2,000 psia (Katz and Lee, 1990). If the wellbore/reservoir pressure is less than 2,000 psia, the flow equation will be in terms of pressure square, p^2, and the energy balance becomes a non-linear equation, which will be difficult to solve analytically. The energy balance, which is derived generally in Section 3.2.2, is expressed in the radial coordinate system as

$$\rho C_p \, u_r \frac{dT}{dr} - \beta T \, u_r \frac{dp}{dr} + u_r \frac{dp}{dr} - K_{Tt}\frac{1}{r}\frac{d}{dr}\left(r\frac{dT}{dr}\right) = 0 \tag{3.15}$$

Substituting equation (3.14) into equation (3.15) gives

$$-\frac{2\pi L \, K_{Tt}}{q}r^2\frac{d^2T}{dr^2} + \left(\rho C_p - \frac{2\pi L \, K_{Tt}}{q}\right)r\frac{dT}{dr} + \frac{\mu q \beta T}{2\pi k h} - \frac{\mu q}{2\pi k L} = 0 \tag{3.16}$$

Solving this second-order differential equation by assuming that the coefficients of the derivatives are independent of temperature gives the general solution with two constants of integration.

$$T(r) = \frac{1}{\beta} + c_0 r^{m_0} + c_r r^{m_r} \tag{3.17}$$

where

$$m_0 = \frac{q}{4\pi L} \left[\frac{\rho C_p}{K_{Tt}} + \sqrt{\left(\frac{\rho C_p}{K_{Tt}} \right)^2 + \frac{4\mu\beta}{kK_{Tt}}} \right] = \text{negative value} \tag{3.18}$$

$$m_r = \frac{q}{4\pi L} \left[\frac{\rho C_p}{K_{Tt}} - \sqrt{\left(\frac{\rho C_p}{K_{Tt}} \right)^2 + \frac{4\mu\beta}{kK_{Tt}}} \right] = \text{positive value} \tag{3.19}$$

Note that q, the constant production rate, is negative because the flow is in the opposite direction of increasing r. Next, apply the first boundary condition, which is T is finite as r approaches zero; thus, the constant of integration (c_0) must be zero. Equation (3.17) becomes

$$T(r) = \frac{1}{\beta} + c_r r^{m_r} \tag{3.20}$$

Applying the second boundary condition, which is $T_{r=h/2} = T_{y=h/2} = T_e$ at $r = h/2$, then c_r can be evaluated

$$c_r = \left(T_e - \frac{1}{\beta} \right) \left(\frac{1}{h/2} \right)^{m_r} \tag{3.21}$$

48

T_e is still an unknown.

Substituting equation (3.21) into equation (3.20), the temperature solution in radial flow is

$$T(r) = \frac{1}{\beta} + \left(T_e - \frac{1}{\beta} \right) \left(\frac{r}{h/2} \right)^{m_r} \tag{3.22}$$

Next, consider the linear flow region. The pressure distribution in the linear flow region is from

$$u_y = -\frac{k}{\mu} \frac{dp}{dy} \tag{3.23}$$

The equation can be expressed by replacing u_y with production rate per area.

$$\frac{q}{2Lh} = -\frac{k}{\mu} \frac{dp}{dy} \tag{3.24}$$

Note that the above equation can be applied to oil, water, or gas (above 2,000 psia). The energy balance for the linear flow in the y-direction is

$$\rho C_p u_y \frac{dT}{dy} - \beta T u_y \frac{dp}{dy} + u_y \frac{dp}{dy} - K_{Tt} \frac{d^2T}{dy^2} = 0 \tag{3.25}$$

Substituting equation (3.24) into equation (3.25) gives

$$\frac{d^2T}{dy^2} - \frac{\rho C_p}{K_{Tt}}\left(\frac{q}{2hL}\right)\frac{dT}{dy} - \frac{\beta\mu}{kK_{Tt}}\left(\frac{q}{2hL}\right)^2 T + \frac{\mu}{kK_{Tt}}\left(\frac{q}{2hL}\right)^2 = 0 \tag{3.26}$$

Solving the resulting second-order differential equation gives

$$T(y) = \frac{1}{\beta} + c_1 e^{m_1 y} + c_2 e^{m_2 y} \tag{3.27}$$

where

$$m_1 = \frac{q}{4hL}\left[\frac{\rho C_p}{K_{Tt}} + \sqrt{\left(\frac{\rho C_p}{K_{Tt}}\right)^2 + \frac{4\beta\mu}{kK_{Tt}}}\right] = \text{negative value} \tag{3.28}$$

$$m_2 = \frac{q}{4hL}\left[\frac{\rho C_p}{K_{Tt}} - \sqrt{\left(\frac{\rho C_p}{K_{Tt}}\right)^2 + \frac{4\beta\mu}{kK_{Tt}}}\right] = \text{positive value} \tag{3.29}$$

Now, apply the two boundary conditions. The first is $T = T_0$ at $y = \frac{Y}{2}$. T_0 is the geothermal temperature at the external boundary. The second is that the heat flux is continuous at the transition of radial and linear flows; in other words, $\left(\frac{dT}{dr}\right)_{r=h/2} = \left(\frac{dT}{dy}\right)_{y=h/2}$. Then we can evaluate the integration constants (c_1, c_2), and the temperature at the transition of radial and linear flows (T_e) in terms of known parameters.

$$c_1 = \frac{(2/h)m_r(T_e - 1/\beta)e^{m_2 Y/2} - (T_o - 1/\beta)m_2 e^{m_2 h/2}}{m_1 e^{m_1 h/2 + m_2 Y/2} - m_2 e^{m_2 h/2 + m_1 Y/2}} \tag{3.30}$$

$$c_2 = \frac{(T_o - 1/\beta)m_1 e^{m_1 h/2} - (2/h)m_r(T_e - 1/\beta)e^{m_1 Y/2}}{m_1 e^{m_1 h/2 + m_2 Y/2} - m_2 e^{m_2 h/2 + m_1 Y/2}} \tag{3.31}$$

50

$$T_e = \frac{1}{\beta} + c_1\,e^{m_1 h/2} + c_2\,e^{m_2 h/2} \tag{3.32}$$

T_e in equation (3.32) is not explicit because c_1 and c_2 depend on T_e, but we can easily solve equation (3.32) for T_e. The explicit form of T_e is written as below.

$$T_e = \frac{1}{\beta} + \frac{-b\,e^{m_1 h/2} + c\,e^{m_2 h/2}}{a - d + g} \tag{3.33}$$

where the parameters a, b, c, d, and g in equation (3.33) are

$$a = m_1 e^{m_1 h/2 + m_2 Y/2} - m_2 e^{m_1 Y/2 + m_2 h/2}$$

$$b = (T_o - \frac{1}{\beta})m_2 e^{m_2 h/2}$$

$$c = (T_o - \frac{1}{\beta})m_1 e^{m_1 h/2}$$

$$d = m_r (\frac{2}{h})e^{m_2 Y/2 + m_1 h/2}$$

$$g = m_r (\frac{2}{h})e^{m_1 Y/2 + m_2 h/2}$$

Finally, the inflow temperature of fluid entering the wellbore at $r = r_w$ is obtained from equation (3.22)

$$T_I = T(r = r_w) = \frac{1}{\beta} + \left(T_e - \frac{1}{\beta}\right)\left(\frac{r_w}{h/2}\right)^{m_r} \tag{3.34}$$

where

T_I is the inflow temperature of the fluid

β is the thermal expansion coefficient of the fluid

T_e is defined by equation (3.33)

r_w is the wellbore radius

h is the thickness of reservoir

m_r is defined by equation (3.19)

Equation (3.34) can be expressed in terms of three main dimensionless groups that represent the causes of the temperature change, which are fluid expansion, viscous dissipation, and convection.   The dimensionless groups are presented in Appendix E.

To illustrate the size of inflow temperature from equation (3.34), we use the fluid and reservoir properties in Table 3.1 to plot the temperature profiles perpendicular to the wellbore for a fluid flowing into a wellbore for various inflow rates, permeabilities and fluid types.   Results are plotted both in linear scale and semi-log scale to see the detail near wellbore (i.e. radial flow region).

Table 3.1   Fluid and reservoir properties at 4,000 psi and 180 ^{o}F

Parameters	Reservoir	Fluids		
		Oil	Gas	Water
Viscosity [cp]		0.38	0.0257	0.48
Heat capacity [Btu/(lb-^{o}F)]		0.524	0.587	1.002
Density [lbm/ft^3]		40	13	63.044
Thermal expansion coefficient [1/^{o}F]		0.000679	0.00236	0.000311
Total thermal conductivity [Btu/(hr-ft-^{o}F)]		2	1.3	2.5
Permeability [md]	50			
Length [ft]	1000			
Width [ft]	3000			
Thickness [ft]	50			
Temperature at external boundary [^{o}F] (see T_o in Figure 3.1)	180			
Pressure at external boundary [psi] (see P_e in Figure 3.1)	4000			
Wellbore diameter [inches]	6			

Figure 3.4 shows how the temperature in the reservoir varies with different oil flow rates. As flow rate increases, the temperature change increases because larger drawdown pressure causes more viscous dissipative heating. As a result, the inflow temperature deviated from the geothermal temperature can infer the inflow rates if the rates are large and cause a detectable change in temperature.
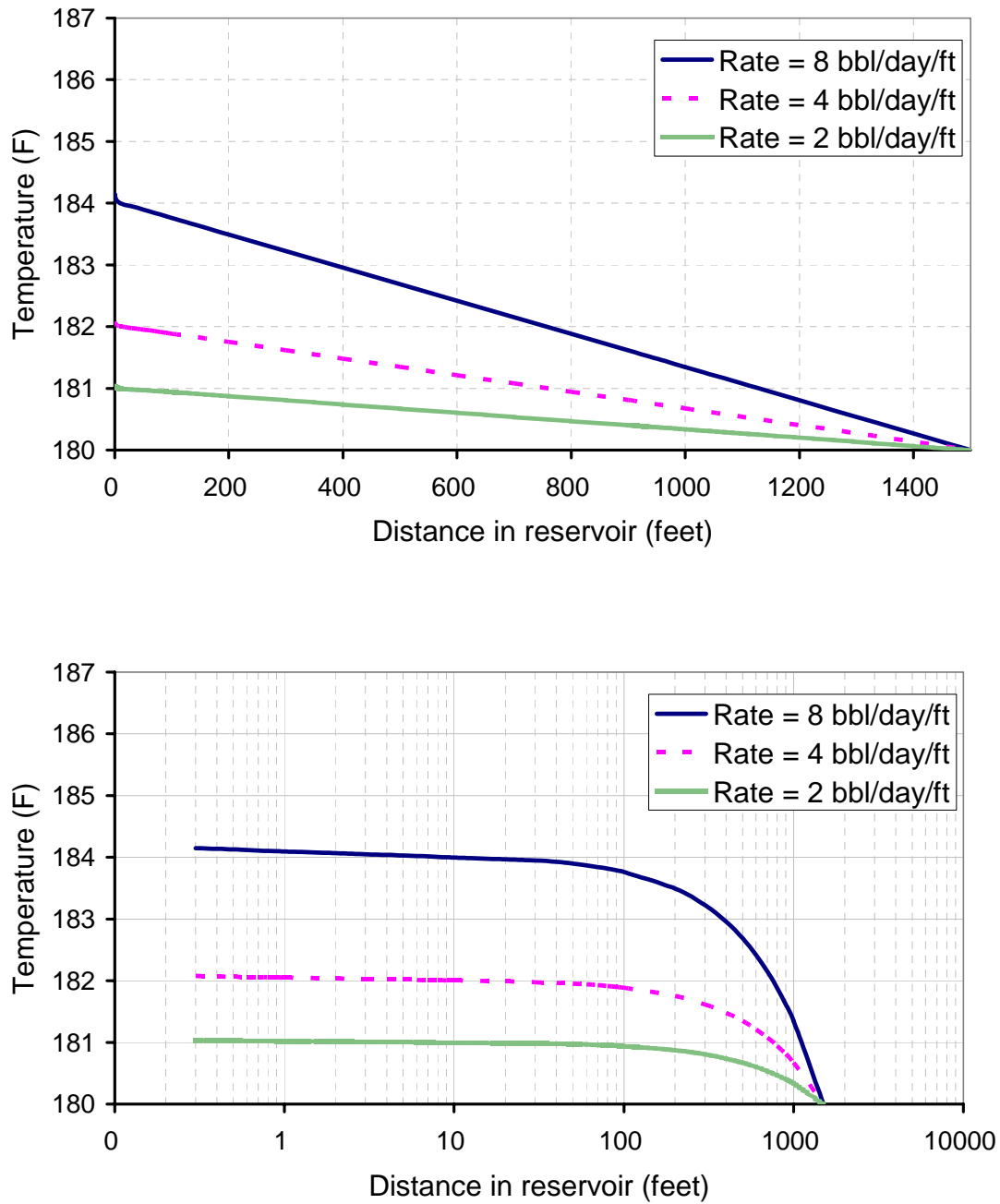
Figure 3.4   Reservoir temperature profiles for different inflow rates in linear (top) and
semi-log (bottom) scales.

Figure 3.5 shows the effect of permeability on the temperature distribution with a fixed inflow rate (4 bbl/d/ft). The inflow temperature decreases as permeability increases because the smaller pressure drop caused by higher permeability leads to a smaller viscous dissipative heating.
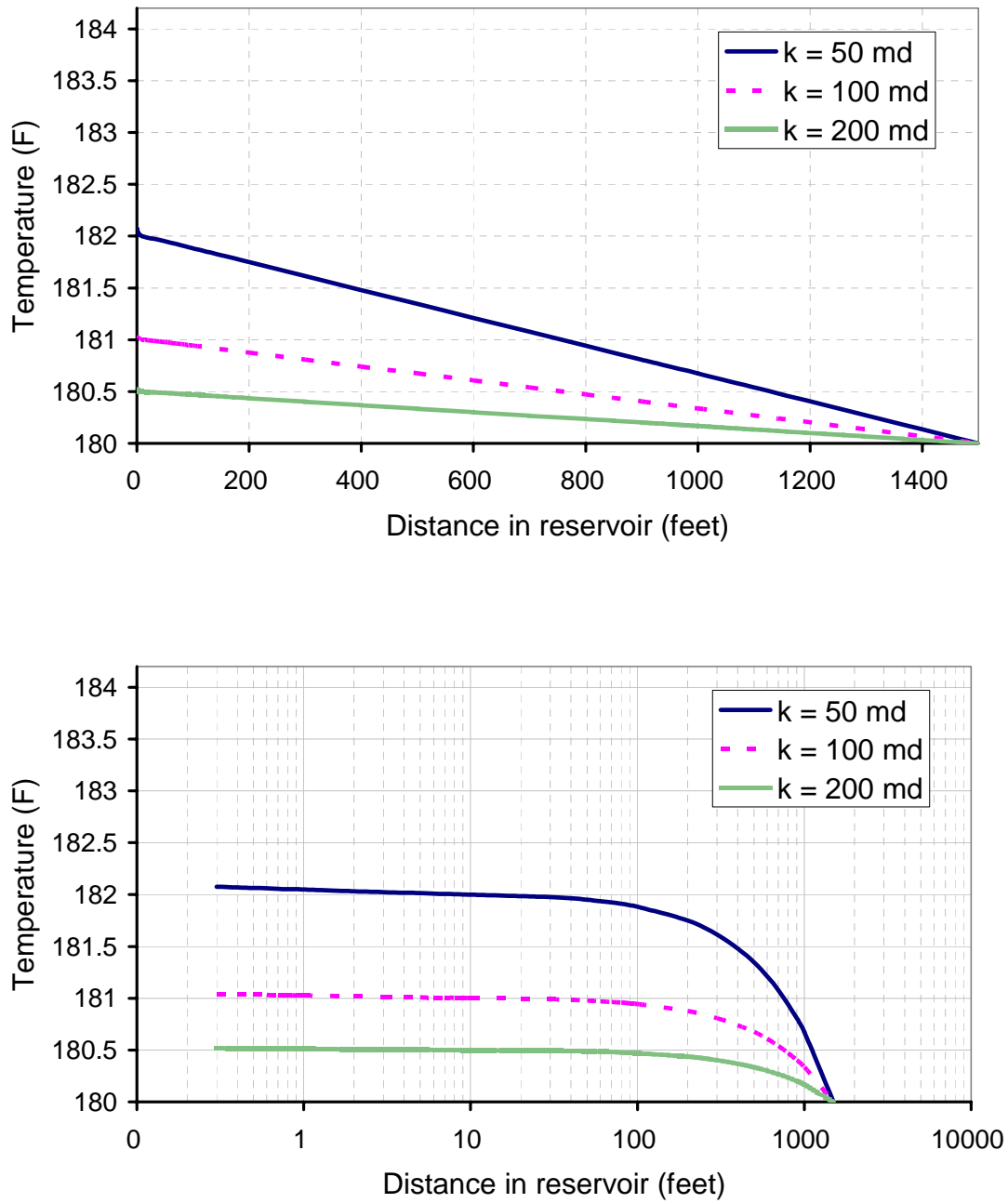
Figure 3.5   Reservoir temperature profiles for different permeabilities at fixed rate in linear (top) and semi-log (bottom) scales.

Figure 3.6 presents the reservoir temperature profiles with different fluids at fixed drawdown pressure (400 psi). It is obvious that the temperature of the gas is substantially smaller than the geothermal temperature because the cooling caused by fluid expansion is much greater than viscous dissipation. On the other hand, liquid (oil/water) experiences the heating because the temperature change caused by the viscous dissipation is greater than by fluid expansion. The temperature of the water is slightly smaller than for the oil because water has a greater heat capacity.
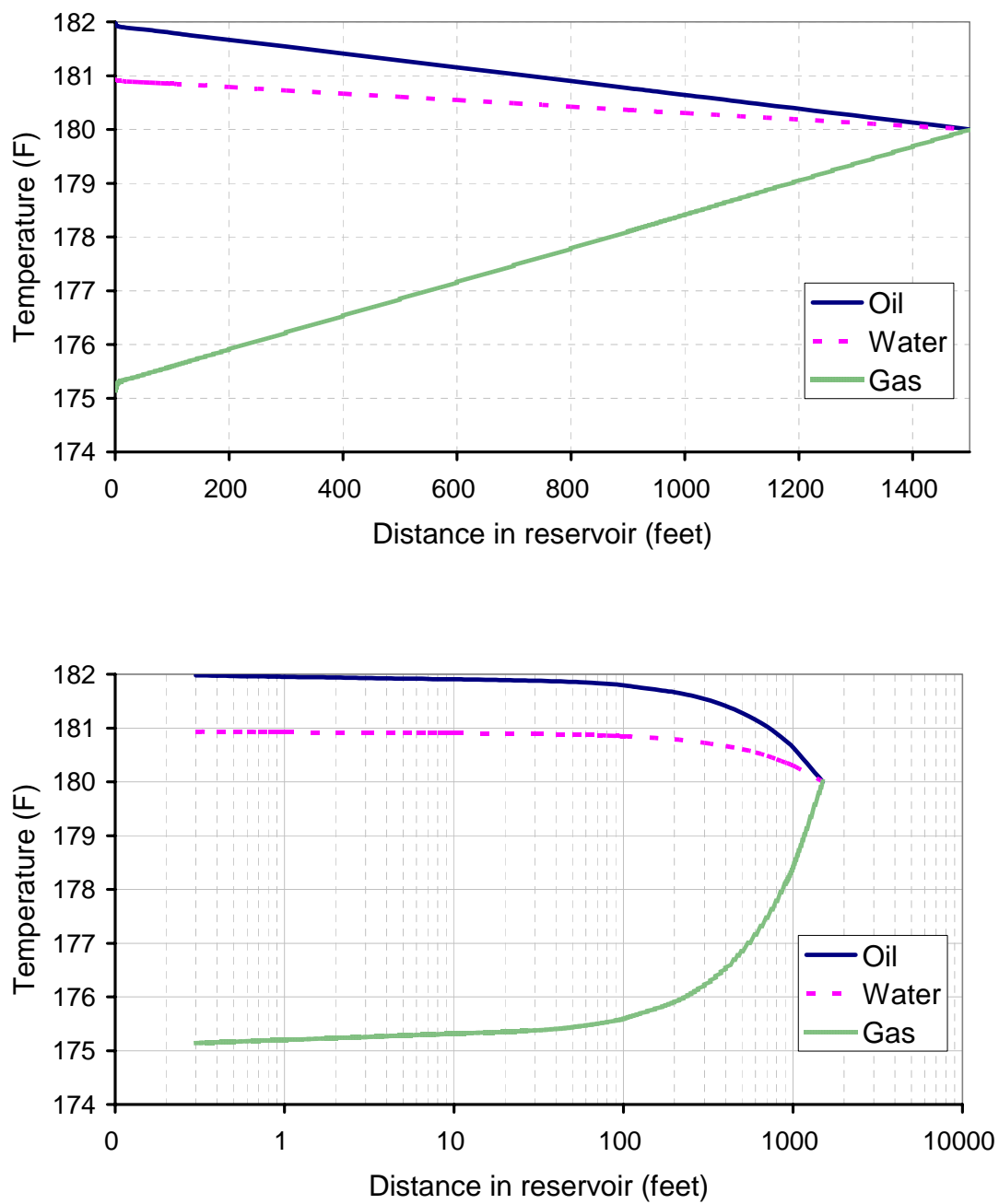
Figure 3.6   Reservoir temperature profiles for different fluid types in linear (top) and
semi-log (bottom) scales.

3.3.1.2   Verification of the analytical inflow temperature model

In developing a new model, a typical practice is to verify the model by using a different approach or testing whether or not the model predicts the correct limiting situation.   This section shows how to verify the analytical inflow temperature model, equation (3.34).

When there is no flow ($q = 0$) the model should reduce to a simple heat conduction solution, which means the geothermal temperature at the external boundary (T_o) should be equal to the inflow temperature (T_I).   Since we would end up with zero divided by zero if we simply substituted $q = 0$ into the solution equation (3.34), we will verify the model by taking the limit as the flow rate (q) approaching zero together with L'Hopital's rule.   For the purpose of making the long equations short, let us name the coefficients of q in the equation (3.28), (3.29), and (3.19) as α, σ, and δ respectively.   Those are written below.

$$\alpha = \frac{1}{4hL} \left[\frac{\rho C_p}{K_{Tt}} + \sqrt{\left(\frac{\rho C_p}{K_{Tt}} \right)^2 + \frac{4\beta\mu}{kK_{Tt}}} \right] \tag{3.35}$$

$$\sigma = \frac{1}{4hL} \left[\frac{\rho C_p}{K_{Tt}} - \sqrt{\left(\frac{\rho C_p}{K_{Tt}} \right)^2 + \frac{4\beta\mu}{kK_{Tt}}} \right] \tag{3.36}$$

$$\delta = \frac{1}{4\pi h} \left[\frac{\rho C_p}{K_{Tt}} - \sqrt{\left(\frac{\rho C_p}{K_{Tt}} \right)^2 + \frac{4\mu\beta}{kK_{Tt}}} \right] \tag{3.37}$$

The inflow temperature model that we want to verify is

59

$$T_I = \frac{1}{\beta} + \left(T_e - \frac{1}{\beta}\right)\left(\frac{r_w}{h/2}\right)^{m_r} \tag{3.34}$$

First, take the limit of the equation (3.34).

$$\lim_{q \to 0} T_I = \lim_{q \to 0}\left(\frac{1}{\beta} + (T_e - \frac{1}{\beta})\left(\frac{r_w}{h/2}\right)^{m_r}\right) \tag{3.38}$$

Since when $q = 0$, $m_r = 0$. The term $\left(\dfrac{r_w}{h/2}\right)^{m_r} = 1$. Equation (3.38) becomes

$$\lim_{q \to 0} T_I = \frac{1}{\beta} + \lim_{q \to 0}(T_e) - \frac{1}{\beta} \tag{3.39}$$

Note that T_e, m_1, m_2, m_r, a, b, c, d, and g are in terms of q. T_e is defined in equation (3.33). Substitute equation (3.33) into equation (3.39)

$$\lim_{q \to 0} T_I = \lim_{q \to 0}\left(\frac{a/\beta - d/\beta + g/\beta - b e^{m_1 h/2} + c e^{m_2 h/2}}{a - d + g}\right) \tag{3.40}$$

Apply L'Hopital's rule by taking the derivative of the numerator and denominator with respect to q.

$$\lim_{q \to 0} T_I = \lim_{q \to 0}\left(\frac{\dfrac{d}{dq}(a/\beta - d/\beta + g/\beta - b e^{m_1 h/2} + c e^{m_2 h/2})}{\dfrac{d}{dq}(a - d + g)}\right) \tag{3.41}$$

60

Take the derivatives and the limits as q approaches zero. These are treated separately in Appendix B. The results are

$$\lim_{q \to 0} T_I = \frac{(-1/\beta)(2/h)\delta - (T_0 - 1/\beta)\sigma + (T_0 - 1/\beta)\alpha + (1/\beta)(2/h)\delta + (1/\beta)(\alpha - \sigma)}{\alpha - \sigma - (2/h)\delta + (2/h)\delta}$$

$$\lim_{q \to 0} T_I = \frac{T_0(\alpha - \sigma)}{(\alpha - \sigma)}$$

$$\lim_{q \to 0} T_I = T_0 \tag{3.42}$$

As expected the model predicts the correct limiting situation. Equation (3.42) means that temperature in the reservoir segment is the same as at the external boundary temperature when there is no flow, so there is no thermal energy generated.

3.3.2 Illustration of initial guess for the wellbore temperature profile

As mentioned earlier, the general reservoir model is iteratively coupled with wellbore model to generate temperature profiles along the horizontal well. An initial guess of the temperature profile is required to start the iterations. With the analytical inflow temperature model developed in Section 3.3.1 together with the multi-segment technique, we can easily calculate the initial wellbore temperature profile because the inflow temperature of the fluid is pre-determined by viewing the production well as an isolated sink, which means the mixing temperature in the wellbore does not affect the temperature of inflow fluid. This section only intends to illustrate the effect of an initial guess. A detailed discussion will be presented later in Section 3.5.

Figure 3.7 shows the inflow temperature of a fluid entering a wellbore and the initial guess for the wellbore temperature profile for an oil and gas production case. In

61

this case, the gas zone begins at the heel of the well and extends 300 feet along the wellbore. The remainder of the 700 feet long wellbore is producing oil. The pressure at the heel was set to 3,400 psi for this illustration. Other input parameters used to plot Figure 3.7 are the same as the ones used before in Table 3.1.
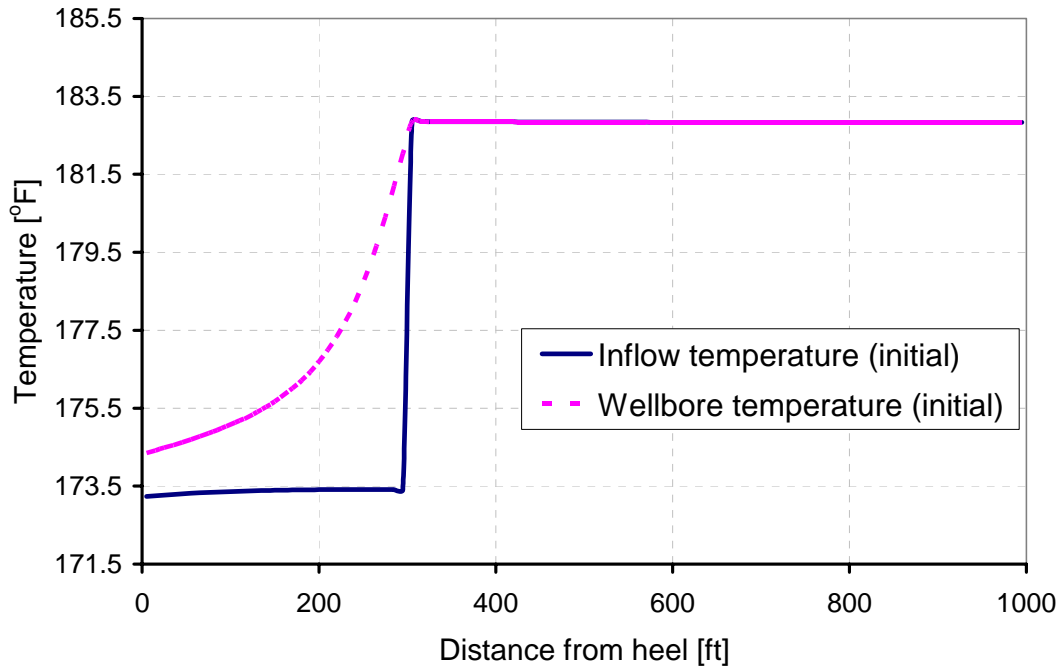
Figure 3.7   Initial wellbore temperature profile calculated from initial inflow temperature (oil inflow from 300-1000 ft, gas inflow from 0-300 ft).

3.4   TEMPERATURE MODEL

Unlike the decoupled model presented in Section 3.3.1, the temperature model in this section accounts for the fact that the sink can lose/gain conductive heat if the temperature of the fluid inside the wellbore is higher/lower than the sandface. The only

difference is the boundary condition at the wellbore, which is the continuity of heat flux at the wellbore radius (r_w).

$$K_{Tt}\left(\frac{dT}{dr}\right)_{r=rw} = U_o(T_I - T_{well}) \tag{3.43}$$

Only heat conduction is considered in equation (3.43) because the heat convection both from the wellbore upstream and from the reservoir constitute T_{well}. The wellbore temperature (T_{well}) is known from a previous iteration. When the wellbore temperature profile is unchanged from one iteration to another, the temperature profile is reached and the iteration stops. The inflow temperature (T_I) is then expressed in terms of known T_{well} and U_o. U_o is the overall heat transfer coefficient between the fluid inside the wellbore and the sandface. It is assumed to be known from experimental work.

The four boundary conditions are necessary to solve the energy balance of the radial and linear composite flow. They are listed below.

1) Heat flux is continuous at the wellbore.

$$K_{Tt}\left(\frac{dT}{dr}\right)_{r=rw} = U_o(T_I - T_{well})$$

2) Heat flux is continuous at the transition between radial and linear flows.

$$\left(\frac{dT}{dy}\right)_{y=h/2} = \left(\frac{dT}{dr}\right)_{r=h/2}$$

3) Temperature is continuous at the transition between radial and linear flows.

$$(T)_{y=h/2} = (T)_{r=h/2}$$

4) Geothermal temperature at the external reservoir boundary is known.

$$(T)_{y=Y/2} = T_o$$

63

In Section 3.3.1, we have already obtained the general solutions of the mass and energy balance for radial and linear composite flows. The general solutions and their resulting derivatives in radial and linear regions are

Radial region:

$$T(r) = \frac{1}{\beta} + c_0 r^{m_0} + c_r r^{m_r} \tag{3.17}$$

$$\frac{dT}{dr} = c_o m_o (r)^{m_o - 1} + c_r m_r (r)^{m_r - 1} \tag{3.44}$$

Linear region:

$$T(y) = \frac{1}{\beta} + c_1 e^{m_1 y} + c_2 e^{m_2 y} \tag{3.27}$$

$$\frac{dT}{dy} = c_1 m_1 e^{m_1 y} + c_2 m_2 e^{m_2 y} \tag{3.45}$$

The particular solution is obtained by evaluating the four integration constants (c_o, c_r, c_1, and c_2). These constants are evaluated by applying the four boundary conditions stated. Substituting the general solutions (3.17), (3.27) and their derivatives (3.44, 3.45) into the boundary conditions gives the four equations and four unknowns below.

$$K_{Tt}\left(c_o m_o r_w^{m_o - 1} + c_r m_r r_w^{m_r - 1} \right) = U_o \left(\frac{1}{\beta} + c_o r_w^{m_o} + c_r r_w^{m_r} - T_{well} \right) \tag{3.46}$$

$$c_1 m_1 e^{m_1 \frac{h}{2}} + c_2 m_2 e^{m_2 \frac{h}{2}} = c_o m_o \left(\frac{h}{2} \right)^{m_o - 1} + c_r m_r \left(\frac{h}{2} \right)^{m_r - 1} \tag{3.47}$$

64

$$\frac{1}{\beta} + c_1 e^{m_1 \frac{h}{2}} + c_2 e^{m_2 \frac{h}{2}} = \frac{1}{\beta} + c_o \left(\frac{h}{2}\right)^{m_o} + c_r \left(\frac{h}{2}\right)^{m_r}$$ (3.48)

$$\frac{1}{\beta} + c_1 e^{m_1 \frac{Y}{2}} + c_2 e^{m_2 \frac{Y}{2}} = T_o$$ (3.49)

The results of solving the equations (3.46), (3.47), (3.48), and (3.49) for the c_o, c_r, c_1, and c_2 are given below. Note that m_o, m_r, m_1, m_2 have already been defined by equation (3.18),(3.19),(3.28),and (3.29), respectively.

$$c_o = \frac{\theta_3 + \theta_4}{\psi_+ + \psi_-}$$ (3.50)

$$c_r = \frac{\theta_1 + \theta_2}{\psi_+ + \psi_-}$$ (3.51)

$$c_1 = \frac{l_3 + l_4}{\psi_+ + \psi_-}$$ (3.52)

$$c_2 = \frac{l_1 + l_2}{\psi_+ + \psi_-}$$ (3.53)

$$\theta_1 = e^{\frac{h}{2}(m_2 + m_1)} \frac{h}{2} r_w^{m_o} (m_2 - m_1)(K_{Tt} m_o - U_o r_w)(\beta T_o - 1)$$

$$\theta_2 = \left(\frac{h}{2}\right)^{m_o} (\beta T_{well} - 1) U_o r_w \left[e^{\frac{h}{2} m_2 + \frac{Y}{2} m_1} \left(\frac{h}{2} m_2 - m_1\right) + e^{\frac{Y}{2} m_2 + \frac{h}{2} m_1} \left(-\frac{h}{2} m_1 + m_o\right) \right]$$

$$\theta_3 = e^{\frac{h}{2}(m_2 + m_1)} \frac{h}{2} r_w^{m_r} (m_2 - m_1)(-K_{Tt} m_r + U_o r_w)(\beta T_o - 1)$$

$$\theta_4 = \left(\frac{h}{2}\right)^{m_r} (\beta T_{well} - 1) U_o r_w \left[e^{\frac{h}{2}m_1 + \frac{Y}{2}m_2} \left(\frac{h}{2}m_1 - m_r\right) + e^{\frac{Y}{2}m_1 + \frac{h}{2}m_2} \left(-\frac{h}{2}m_2 + m_r\right) \right]$$

$$\psi_+ = \beta r_w^{m_r} \left(\frac{h}{2}\right)^{m_o} (K_{Tt} m_r - U_o r_w) \left[e^{\frac{Y}{2}m_2 + \frac{h}{2}m_1} \left(\frac{h}{2}m_1 - m_o\right) + e^{\frac{h}{2}m_2 + \frac{Y}{2}m_1} \left(-\frac{h}{2}m_2 + m_o\right) \right]$$

$$\psi_- = \beta r_w^{m_o} \left(\frac{h}{2}\right)^{m_r} (K_{Tt} m_o - U_o r_w) \left[e^{\frac{Y}{2}m_1 + \frac{h}{2}m_2} \left(\frac{h}{2}m_2 - m_r\right) + e^{\frac{h}{2}m_1 + \frac{Y}{2}m_2} \left(-\frac{h}{2}m_1 + m_r\right) \right]$$

$$l_1 = r_w^{m_o} e^{\frac{h}{2}m_1} (-K_{Tt} m_o + U_o r_w)(\beta T_o - 1)\left(\frac{h}{2}\right)^{m_r} \left(\frac{h}{2}m_1 - m_r\right)$$

$$l_2 = \left(\frac{h}{2}\right)^{m_o} \left[e^{\frac{h}{2}m_1} r_w^{m_r} \left(-\frac{h}{2}m_1 + m_o\right)(-K_{Tt} m_r + U_o r_w)(\beta T_o - 1) + e^{\frac{Y}{2}m_1} U_o r_w \left(\frac{h}{2}\right)^{m_r} (\beta T_{well} - 1)(m_r - m_o) \right]$$

$$l_3 = r_w^{m_r} e^{\frac{h}{2}m_1} (K_{Tt} m_o - U_o r_w)(\beta T_o - 1)\left(\frac{h}{2}\right)^{m_r} \left(\frac{h}{2}m_2 + m_r\right)$$

$$l_4 = \left(\frac{h}{2}\right)^{m_o} \left[e^{\frac{h}{2}m_2} r_w^{m_r} \left(\frac{h}{2}m_2 - m_o\right)(-K_{Tt} m_r + U_o r_w)(\beta T_o - 1) - e^{\frac{Y}{2}m_2} U_o r_w \left(\frac{h}{2}\right)^{m_r} (\beta T_{well} - 1)(m_r - m_o) \right]$$

Once the integration constants are known, the inflow temperature model for a reservoir segment is

$$T_I = T(r = r_w) = \frac{1}{\beta} + c_o r_w^{m_o} + c_r r_w^{m_r} \tag{3.54}$$

where

T_I is the inflow temperature of the fluid

c_o is defined by equation (3.50)

c_r is defined by equation (3.51)

m_o is defined by equation (3.18)

66

m_r is defined by equation (3.19)

This inflow temperature is for each segment along the horizontal wellbore. Each reservoir segment produces a single-phase while the wellbore flow can be a multi-phase flow. Based on these inflow temperature, the wellbore temperature profile is then calculated by using the non-isothermal wellbore model discussed in Section 2.3. For the next iteration, the inflow temperature in each segment is again calculated based on the information from the previous iteration. The iteration process stops when the wellbore temperature profile is unchanged from one iteration to another, which means the wellbore temperature profile is converged. The condition for convergence is when the relative error is less than 10^{-6}. The relative error is calculated by the equation below.

$$\frac{(\widetilde{\mathbf{T}}_{well}^{l} - \widetilde{\mathbf{T}}_{well}^{l+1})^{T} (\widetilde{\mathbf{T}}_{well}^{l} - \widetilde{\mathbf{T}}_{well}^{l+1})}{(\widetilde{\mathbf{T}}_{well}^{l})^{T} (\widetilde{\mathbf{T}}_{well}^{l})} < 10^{-6}$$

where $\widetilde{\mathbf{T}}_{well}$ is the matrix of wellbore temperature. Superscript T means the transpose of the matrix. Superscripts l and $l+1$ indicate a previous iteration and a new iteration, respectively.

To illustrate the converged temperature profile along the wellbore, we again consider the case where a gas zone begins at the heel of the well and extends 300 feet along the wellbore, and the remaining 700 feet of the wellbore is producing oil. Figure 3.8 shows the converged inflow temperature of fluid entering the wellbore, and the converged temperature profile inside the well. A detailed discussion is deferred to the next section (Section 3.5).
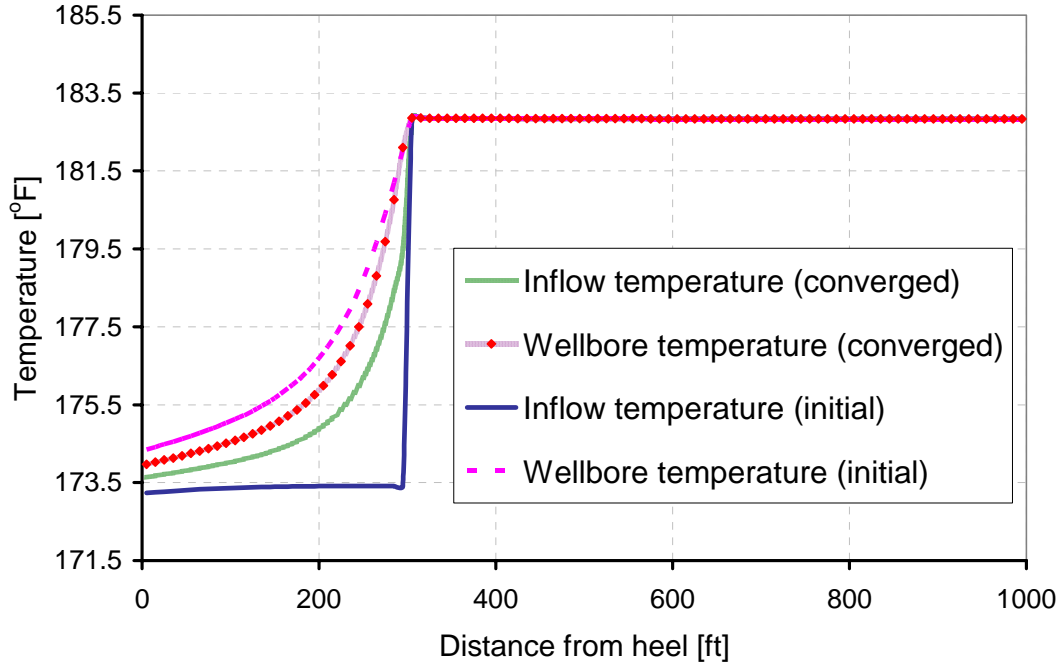
Figure 3.8   Converged wellbore temperature profile calculated from iteratively coupled
            model (oil inflow from 300-1000 ft, gas inflow from 0-300 ft).

3.5   RESULTS AND DISCUSSION

As stated in the objectives, we want to develop a model to investigate the link between the temperature profiles in the horizontal well and the reservoir performance. Specifically, we want to examine the size of the temperature change in a production well, aiming to quantitatively relate the inflow rates and types of fluid entering the wellbore with distributed temperature data.   We use the model to demonstrate the link under specific production scenarios.   Results of this study should help assess the potential value of distributed temperature data.

Table 3.1 presents the input parameters used to generate results.   Fluid property correlations are presented in Appendix A.   The horizontal well is completed open hole

68

with inside diameter of 6 inches.   The reservoir is divided into several 10 foot segments containing the wellbore in the center of the reservoir segments.   Each segment of the reservoir can produce a different fluid into the wellbore (oil, water or gas) or assign to be a non-producing segment.   There are several parameters that affect the temperature data, including fluid and rock properties, wellbore and reservoir dimensions.   Those parameters are fixed so that the simulated results are purturbed from the same reference to allow fair comparisons between the cases.

We study the temperature behavior by varying flow rates, fluid types, and locations of fluid entries. We present three production scenarios in which temperature profiles are most likely to be used in a horizontal production well; the first use is to infer inflow profiles, the second is to identify water or gas entry, and the third is to locate no-flow sections.

3.5.1   Temperature profiles for single-phase production

This section shows that the temperature profiles can be used as a means to provide information about the inflow rates along a horizontal well.   We assume that the geothermal temperature at the well depth is known, and a single phase is producing from the entire length of the horizontal well.

For oil, Figure 3.9 shows the temperature and pressure profiles for two inflow rate profiles, which resulted from setting the heel pressure to 3,600, and 3,400 psi.   All of the temperatures are greater than the geothermal temperature at the well depth because the oil expands because of the pressure drop, and gains temperature because of the Joule-Thomson effect.   The temperature profile shows a slight increase towards the heel of the horizontal well.   This increase corresponds to the inflow rate profile and the wellbore pressure drop along the well.   The only interesting point here is how much the

temperature profiles deviate from the geothermal temperature; the deviation is directly proportional to the inflow rates.

The strong sensitivity between temperature and inflow rate promises that the measured temperature profiles can be used to infer inflow rate profiles by using the temperature model developed. Since the wellbore is large (6 inches) for this open-hole completion, the oil velocity in the wellbore is small; thus, the temperature, pressure, and inflow rate profiles do not change significantly along the well from toe to heel. If we were interested in wellbore flow effect, we could simply reduce the wellbore diameter; as a result, the wellbore flow would be dominant, and the wellbore temperature, pressure, and inflow rate profiles would show dramatic changes along the well from toe to heel.

For water, Figure 3.10 shows similar plots to that from the oil production case but the size of temperature change is smaller than for oil because water has a greater heat capacity and density, so the Joule-Thomson effect of water is smaller than that of oil. Besides, water has larger viscosity than this oil at reservoir condition (180 ^{o}F, 4,000 psi), so the water flow rate is less than the oil rate under the same drawdown pressure.

For gas, Figure 3.11 shows the temperatures are significantly (5-6 ^{o}F) lower than the geothermal temperature at the well location, especially near the heel. Moreover, the decrease in temperature (1-2 ^{o}F) along the well from toe to heel is much larger than the liquid production cases. This temperature change is caused mainly by Joule-Thomson cooling resulted from the pressure drop in both the wellbore and the reservoir. Contrary to the liquid temperature profiles, the gas temperature profiles decrease toward the heel. The size of the temperature decrease corresponds to the inflow rate and the pressure drop along the well. At the same heel pressure, the inflow rates are much larger for gas than for the oil because the gas viscosity is much smaller than the oil viscosity.
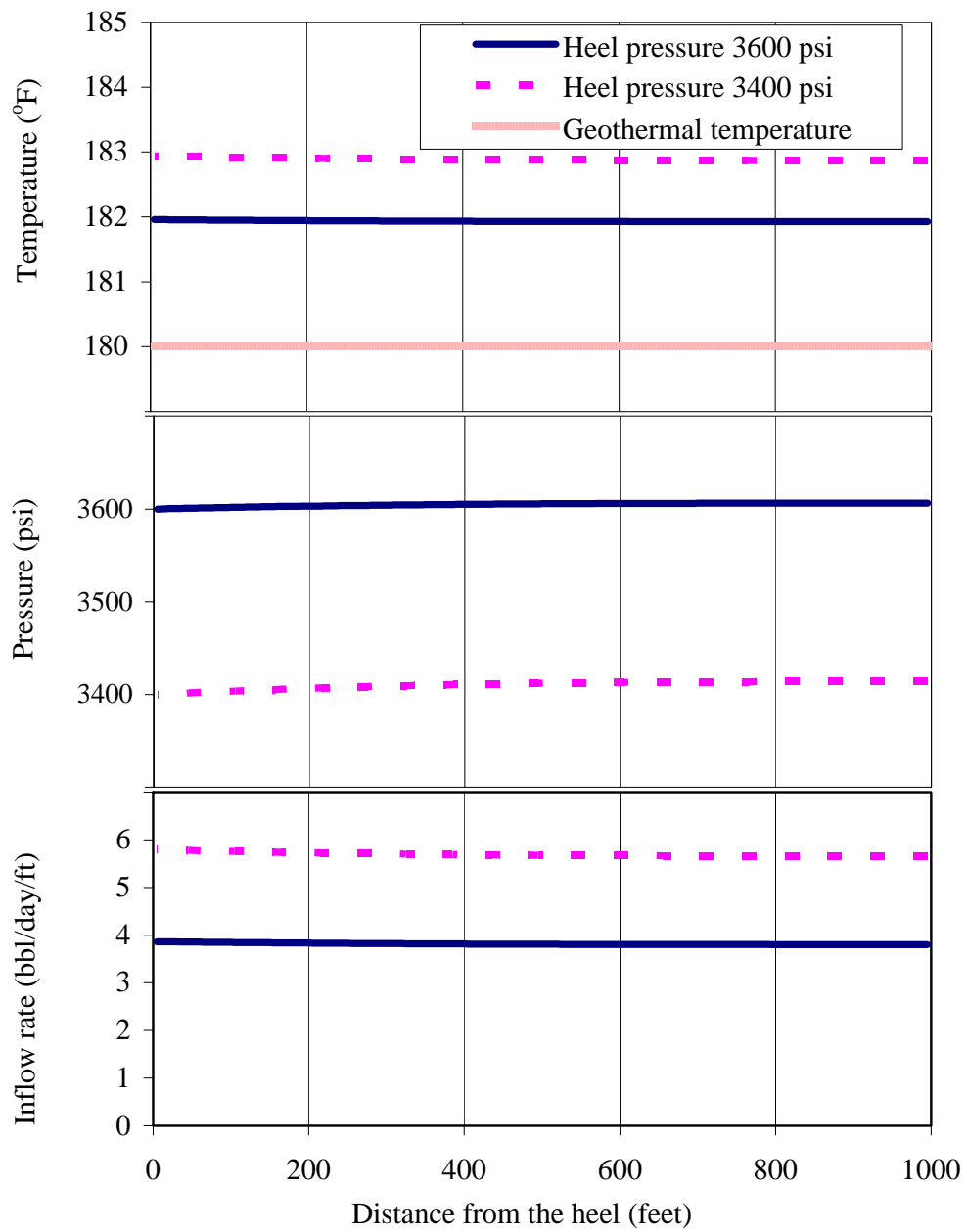
Figure 3.9   Temperature, pressure, and inflow oil rate profiles for a comparison of
different heel pressures.

71
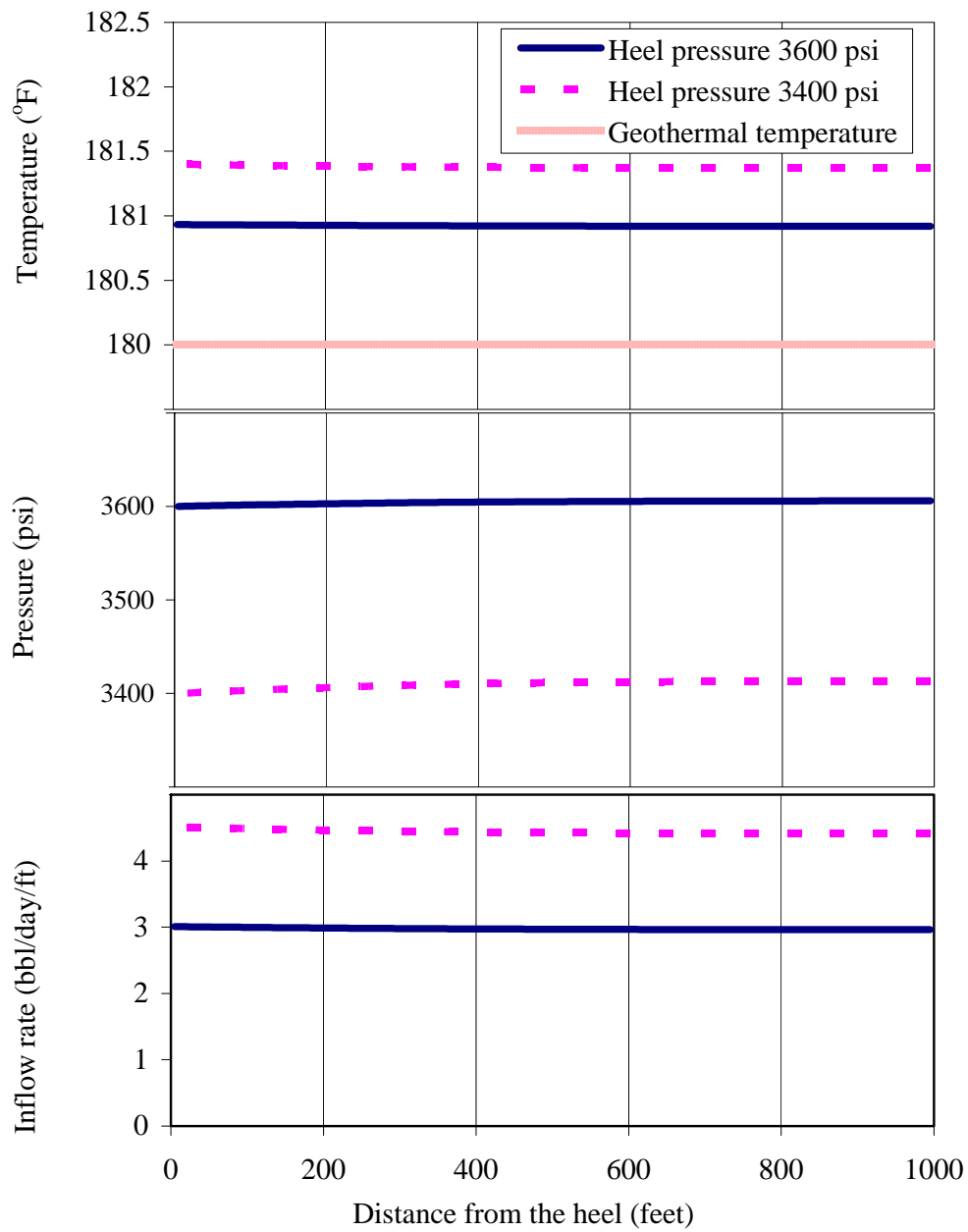
Figure 3.10   Temperature, pressure, and inflow water rate profiles for a comparison of different heel pressures.
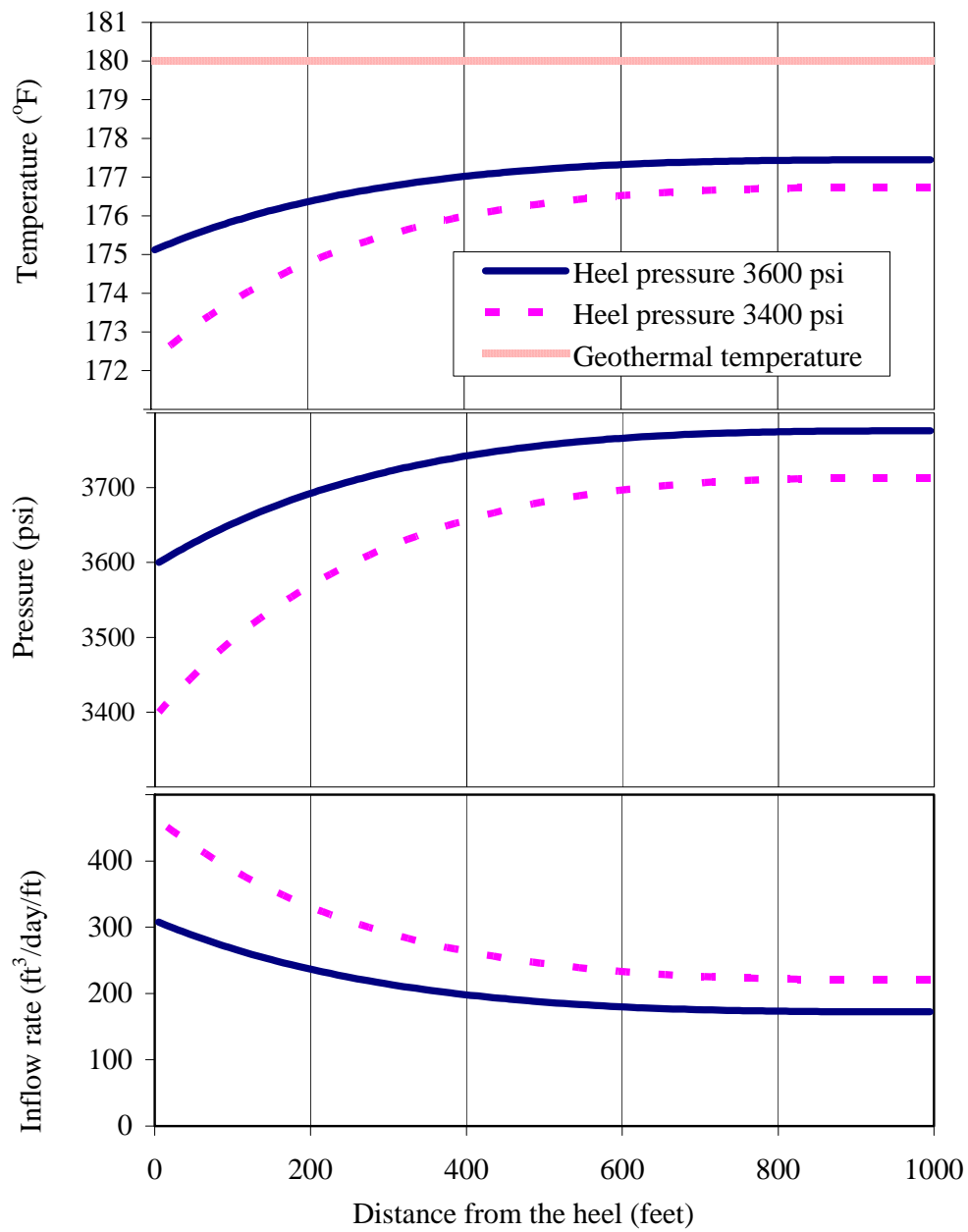
Figure 3.11   Temperature, pressure, and inflow gas rate profiles for a comparison of different heel pressures.

3.5.2 Temperature profiles for commingled production

A horizontal well is typically thousands of feet long, and its horizontal sections can be producing water or gas instead of oil. We use two production scenarios to illustrated how the temperature profile can be used to identify gas or water entry. We first consider a case in which water is produced from a middle section while oil is produced from the others. Figure 3.12 illustrates this case. The water sections are 300 feet long, and the rest of 700 feet sections are producing oil. We set the heel pressure at 3,400 psi, and then use the model developed to compute the temperature, pressure, and inflow rate profiles.

Oil inflow   Water inflow   Oil inflow
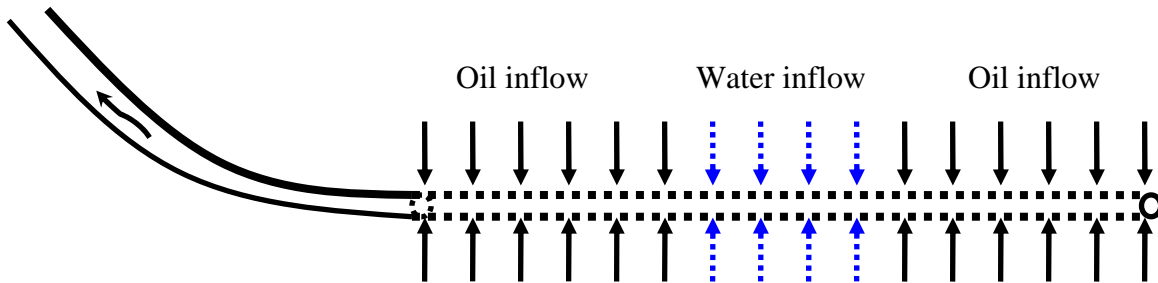
Figure 3.12   Sketch illustrates commingled production of oil and water.

The inflow rate profile in Figure 3.13 shows that the inflow water rate in the middle section is less than for oil because of its larger viscosity, so the productivity index of the water zone is less than that of oil. In addition, water or oil enters the wellbore with a different temperature as presented in Figure 3.6. Water enters at a lower temperature than oil because of its larger heat capacity and density. Thus, the temperature in the well begins to drop at the start of the water zone (650 feet from the

74

heel) and continues to decrease across this entire zone.   After the end of the water zone (350 feet from the heel), oil production that is relatively higher inflow temperature warms up the wellbore flowing fluids, and the wellbore temperature increases gradually toward the heel of the horizontal well.   A conclusion drawn from Figure 3.13 is that the water zone can be identified as the sections over which the wellbore temperature is decreasing toward the heel.   The size of the temperature change is relatively large (0.6 ^{o}F) and within the resolution to be detected by DTS.   The pressure profile in Figure 3.13 is relatively smooth; it would be difficult to get any information about the water zone from it alone.
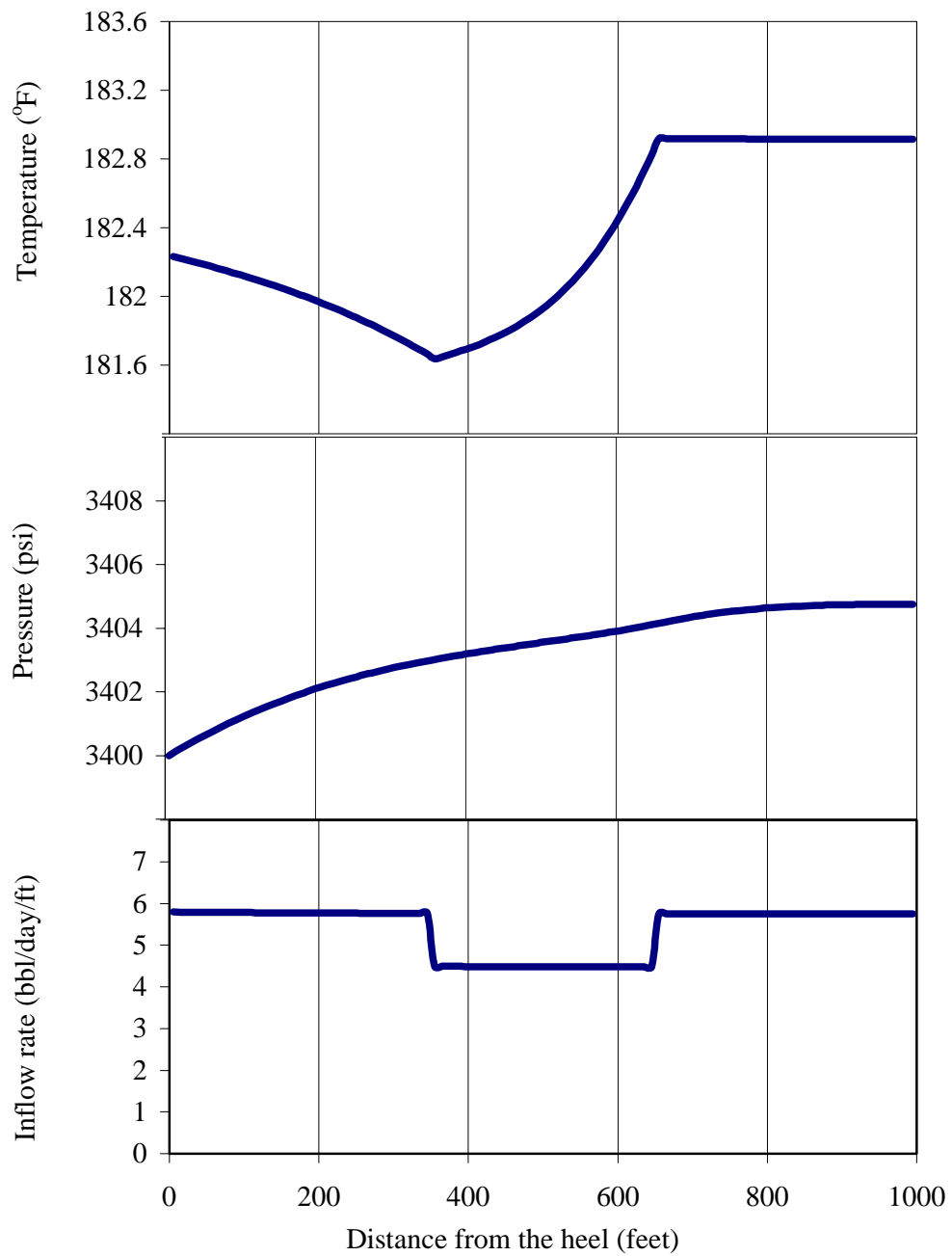
Figure 3.13   Temperature, pressure, and inflow rate profiles for oil and water commingled production.

Another use of the temperature profile is to identify a gas zone. We consider a case in which gas is produced from the 300 feet near the heel section while oil is produced from the others. Figure 3.14 illustrates this case. The heel pressure, the well constraint, is kept the same (3,400 psia) as the water and oil production case discussed before.

Gas inflow   Oil inflow
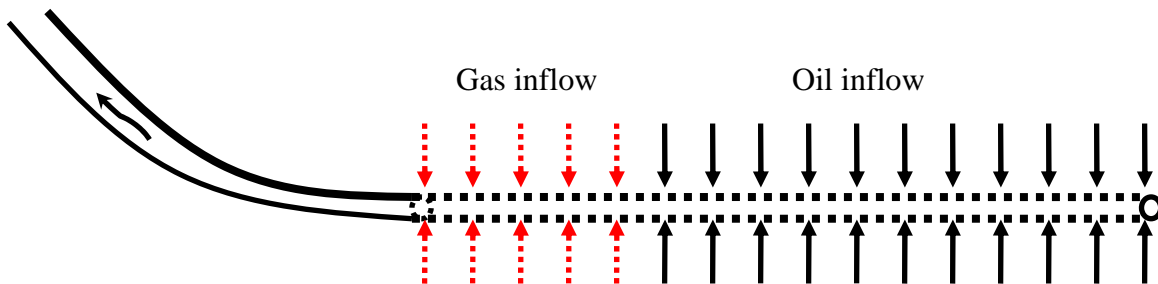
Figure 3.14   Sketch illustrates commingled production of oil and gas.

Figure 3.15 shows the calculation results of this case from the temperature model developed. The large inflow rate indicates the location of the gas zone. The gas production rate is much larger than the oil rate because of its much smaller viscosity. The pressure profile also indicates that there are two pressure gradients ($\frac{dp}{dx}$) along the entire producing length; first is the small pressure gradient over the oil production zone, the second is the large pressure gradient over the gas production zone where the wellbore flow velocity is large and the mixing properties between gas and oil cause the pressure gradient to be dramatically changed. However, the most obvious indicator of the gas zone is the sharp decrease in the temperature over the gas zone as shown in Figure 3.15 (top plot). Although a water zone in the previous case (Figure 3.12 and 3.13) is also identified as the region over which the temperature decreases, we should not be confused

between the two cases because the size of the temperature decrease in the gas production zone is much larger than in the water zone, and the temperature profile over the gas zone is lower than the geothermal temperature if the gas inflow rate is large enough, which is the most likely the case.
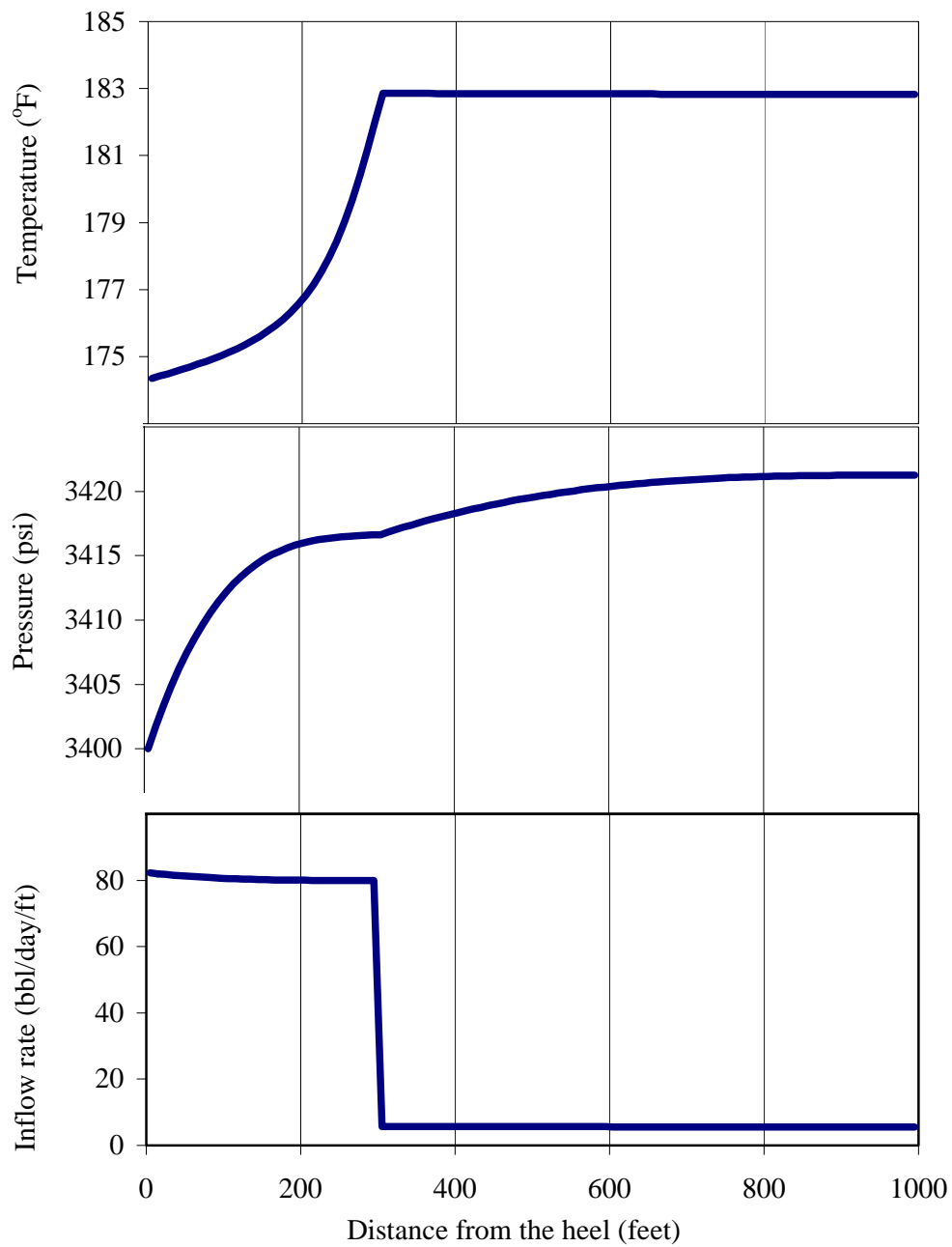
Figure 3.15   Temperature, pressure, and inflow rate profiles for oil and gas commingled
production.

3.5.3 Temperature profiles for identifying no-flow zone

In a long horizontal production well, it is possible that some sections along the wellbore are not producing as expected. Knowing the location of a no-flow zone helps tell where to perform a well stimulation (acidizing, fracturing, etc.) if the job is needed over that zone. To explore whether temperature profile could locate the no-flow zone, we demonstrate two example cases; the first case shows the temperature profile from an oil production well with a no-flow zone in the middle, and the second shows the temperature profile from a gas production well with a no-flow zone in the middle.

We first consider a case in which there is a no-flow zone with a length of 300 feet in the middle of the well while oil is producing from the rest of the well. Figure 3.16 illustrates the case. We again set the heel pressure at 3,400 psi and use the temperature model to calculate the results. The results are presented in Figure 3.17, which includes the temperature, pressure, and inflow rate profiles. The inflow rate profile shows a no-flow zone in the middle (between 350 and 650 feet from the heel). The inflow rates are relatively uniform over the producing sections because the pressure drop along the wellbore is small as a result of the large wellbore size (6 inches). The temperature slightly increases from toe to heel but over the no-flow zone the profiles is flatter than the oil producing zone because there is no heat convection into the wellbore and the heat because of the wellbore flow is small, so the warmer oil inside the well loses heat conduction through the sandface. However, the size of the temperature change in this case is very small because the inflow oil enters the entire length of wellbore at relatively the same temperature, so the change in temperature is solely caused by wellbore flow effect.
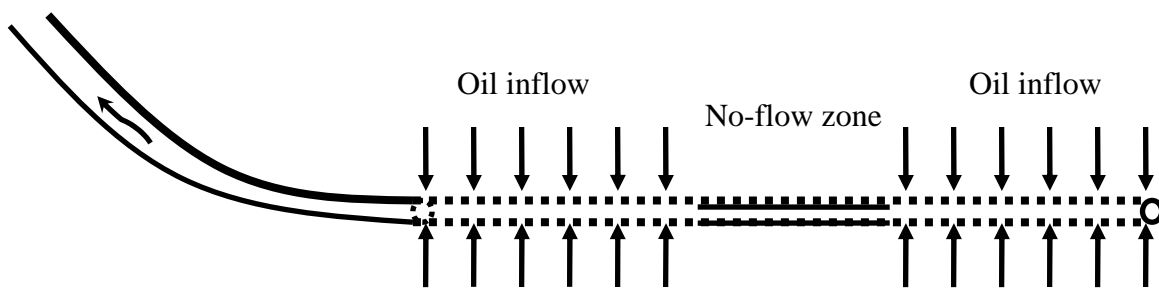
Figure 3.16   Sketch illustrates a no-flow zone in an oil production well.
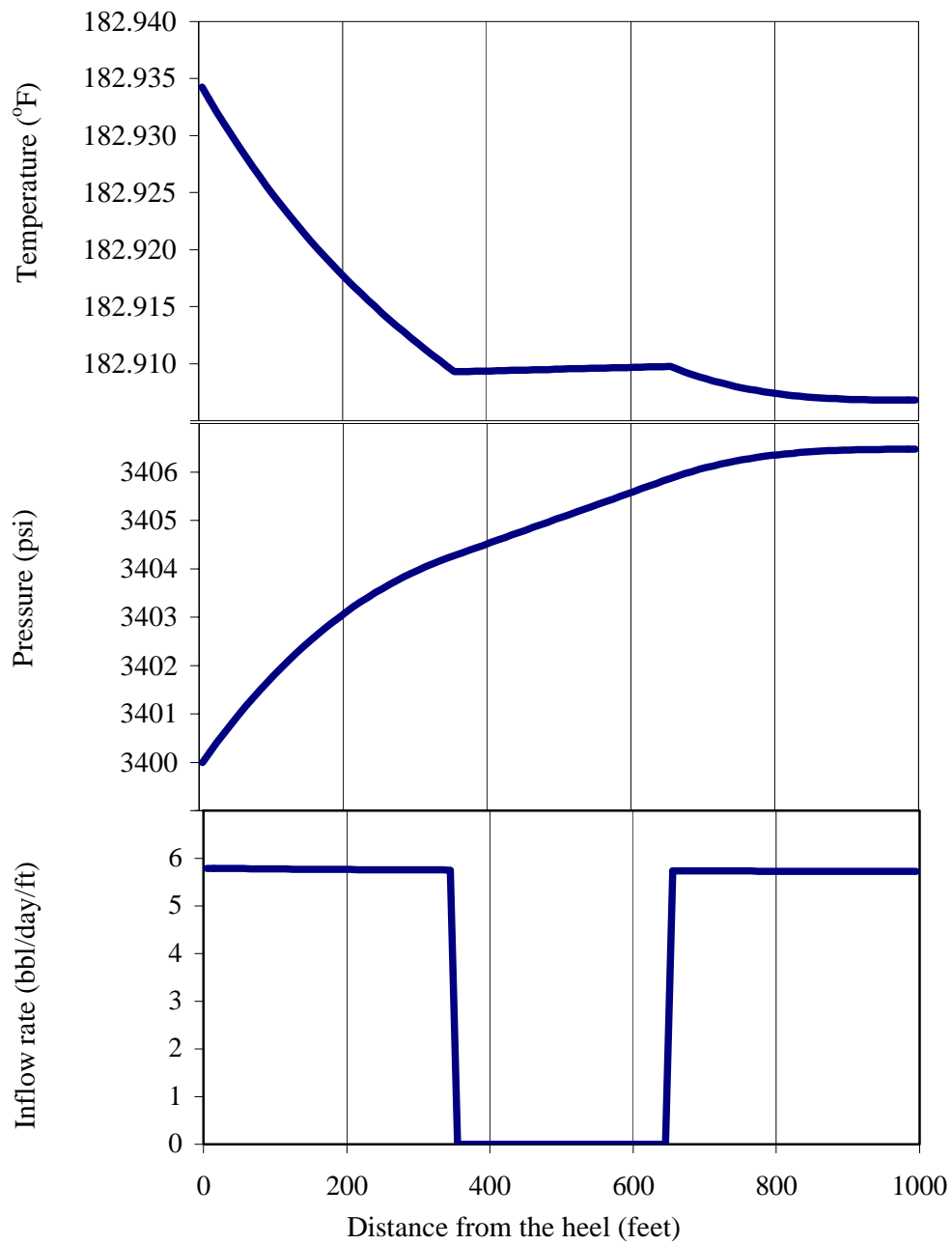
Figure 3.17   Temperature, pressure, and inflow rate profiles for a no-flow zone in an oil production well.

For the next example, we further study a no-flow zone in the middle of a gas production well. Similar to the previous case, we set the no-flow zone to have a length of 300 feet but the well is now producing gas instead of oil. We again keep the heel pressure at 3,400 psi. Figure 3.18 illustrates this case. The plots of the temperature, pressure, and inflow rate profiles are presented in Figure 3.19.

As shown from the plots, the inflow is large, and causes a large pressure drop along the well. As the pressure drops, the gas expands and the temperature decreases because of the Joule-Thomson effect in the wellbore. The size of the temperature change is large both for the wellbore flow and the reservoir inflow. Although there is a slight change in the slope of the temperature profile over the no-flow zone, because the flowing gas in the wellbore gains conductive heat from the sandface, the temperature change caused by the wellbore flow effect is relatively dominant and smoothes out the temperature profile. As a result, it would be difficult to detect a no-flow zone in a gas production well. However, if the temperature sensors were able to measure the inflow temperature (i.e. the fiber optic sensors were inserted directly into the sandface and isolated from the wellbore flow effect), the no-flow zone could be easily located because the temperature over the no-flow zone is close to the geothermal temperature while the inflow temperature over the rest of the well is a few degrees larger that the geothermal temperature for an oil production well, or 5-6 ^{o}F smaller than the geothermal temperature for a gas production well case.
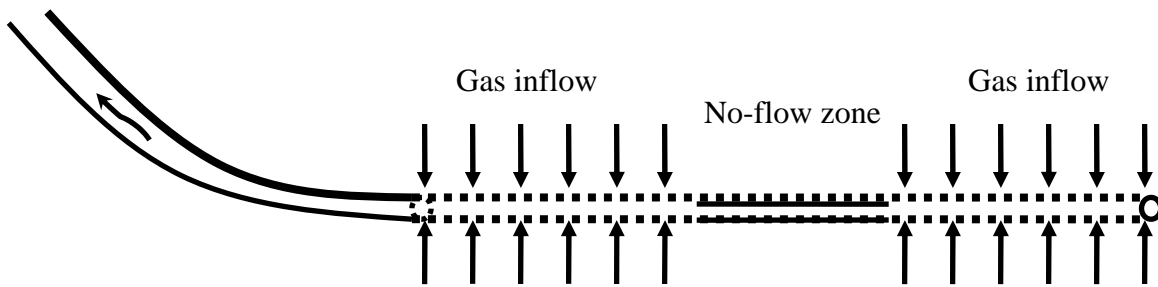
Figure 3.18   Sketch illustrates a no-flow zone in a gas production well.
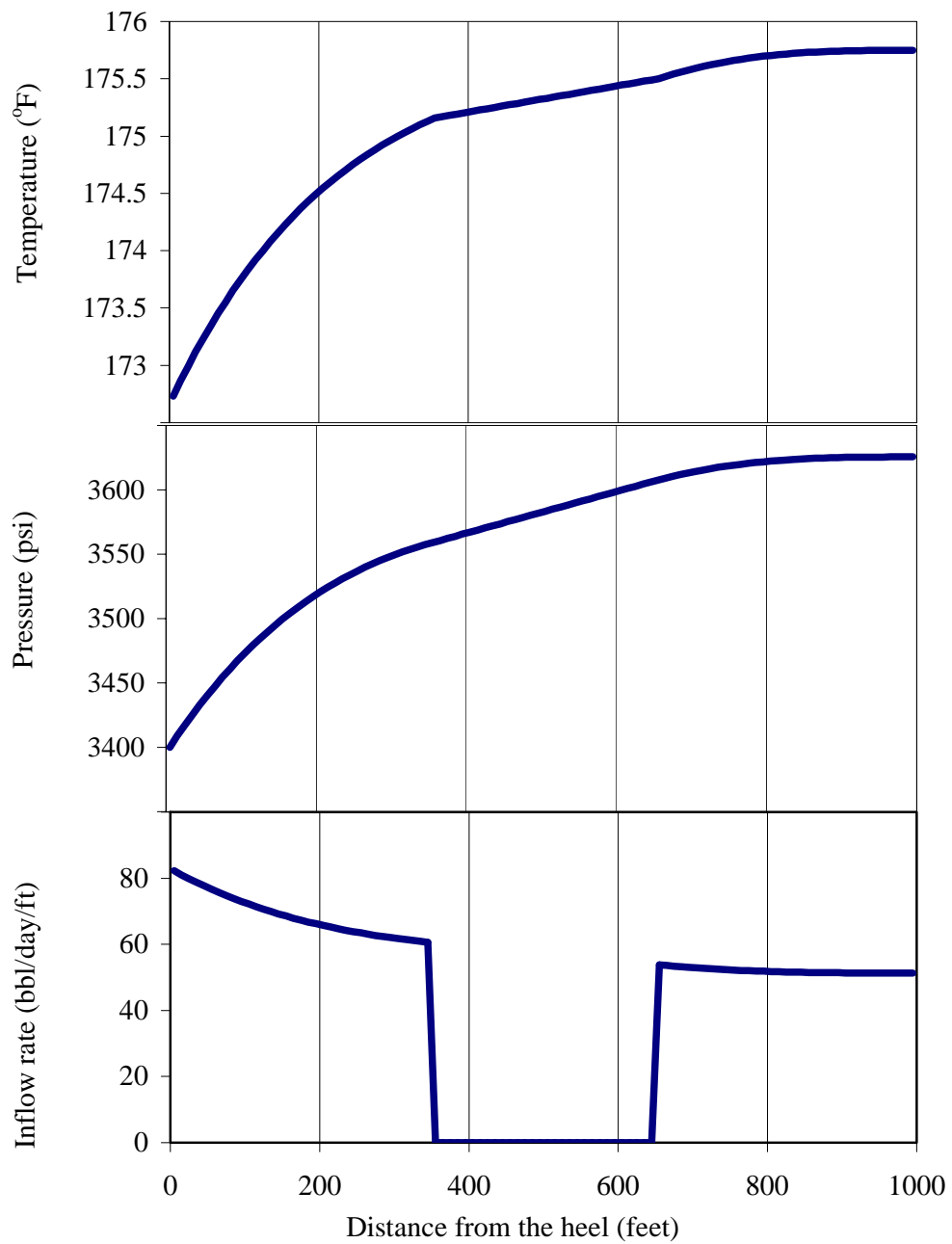
Figure 3.19   Temperature, pressure, and inflow rate profiles for a no-flow zone in a gas
production well.

CHAPTER 4

Numerical Temperature Model of Two-Phase Flow

Chapter 3 presented an inflow temperature model that resulted from analytically solving the mass and energy balances of single-phase flow in a box-shaped isotropic reservoir with no-flow lateral boundaries. The model predicts wellbore temperature under the assumption that gas, oil, and water are flowing at the same geothermal temperature or from the same depth. Based on this assumption, the model predicts that water enters at a lower temperature than oil because of its larger heat capacity. The prediction seems to be in conflict with field observation where we commonly see water entering at the higher temperature than oil (Foucault *et al.*, 2004).

This chapter further studies the temperature behavior in a horizontal well subjected to bottom water drive. Water in this case is initially located in a deeper and warmer zone below a horizontal well.

Unlike the previous analytical temperature model, this model numerically solves mass and energy balances for two-phase flow both in the reservoir and wellbore. The fluid properties also vary with temperature and pressure while flowing. The key difference from typical thermal oil recovery simulators is that the model includes a temperature change caused by pressure drops, which is usually neglected by those simulators. Since the temperature change in the context of monitoring a production well is expected to be small, all of the subtle energy changes in the reservoir must be included. Neglecting the Joule-Thomson effect for liquid flow will result in an underestimation of the size of the temperature change.

We will focus our study only on a bottom water drive reservoir, in which water coning is prone to occur. Although there are pressure-based models that can predict water breakthrough time for water coning toward horizontal wells, what we are seeking here is an alternative way to detect water breakthrough by assuming that the DTS are permanently installed in a horizontal well. We will develop a basis to detect water entry and breakthrough time based on temporal changes of the temperature profiles. A similar basis could also detect gas entry in a gas-cap drive reservoir because gas properties are much different from oil. The size of the temperature decrease for gas flowing into the well should be larger and the gas inflow easier to locate than for oil-water flow.

Before presenting the results in Section 4.4, we first describe the model geometry and finite-difference formulation of the governing equations. Section 4.1 gives a physical description of the model. Section 4.2 shows finite-difference formulation of mass and energy balances. Section 4.3 discusses how the numerical model was validated.

4.1. PHYSICAL DESCRIPTION OF THE MODEL

Figure 4.1 shows a schematic of the reservoir and well geometry. We consider a horizontal well fully penetrated through a box-shaped reservoir with no-flow boundaries at the top and the sides of the reservoir. Initial pressures are at static equilibrium at which the water pressures are function of the elevation only. For convenience, water in the reservoir is initialized at irreducible water saturation. Temperature of the five boundaries is fixed at its initial geothermal temperature. We assume that an active aquifer at the bottom of the reservoir gives a constant pressure and temperature boundary (4,000 psi, 180 ^{o}F) located at the original water-oil contact. A straight horizontal well is placed in the center of the oil reservoir having horizontal to vertical permeability ratio of five ($k_h/k_z = 5$). The horizontal well is modeled as an open hole over its entire length.

87
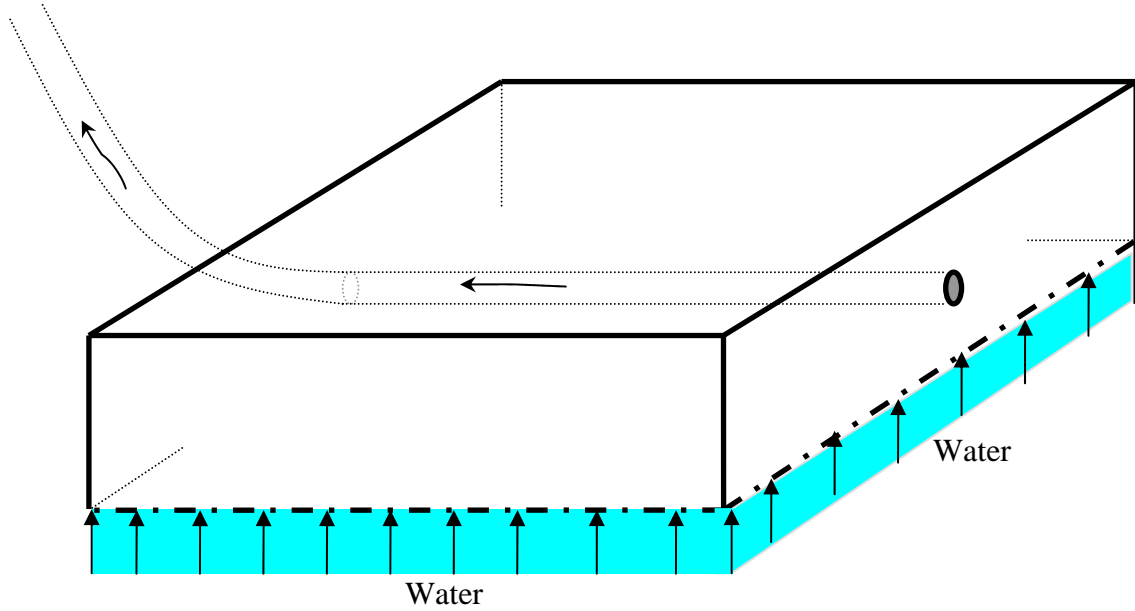
Figure 4.1   Schematic of bottom water drive reservoir and well at the initial condition.

For two-phase flow in a reservoir, we are required to have a capillary pressure model and a relative permeability model.   Although these models are not the main causes of temperature changes, they are commonly used to describe two-phase flow in reservoir simulation.   In this study, we have chosen a model and consistently used it throughout example cases.

Capillary pressure is expressed as a function of interfacial tension, permeability, porosity and saturation.   For water and oil flow, the capillary pressure curve is modeled as

$$P_{cow} = C \sigma \sqrt{\frac{\phi}{k}} (1 - S_w)^E$$

where k is the geometric mean of permeability in the x, y, z directions. The parameters C and E are usually determined from matching a water/oil experimental capillary pressure curve. Here we choose $C = 10 \dfrac{psi\,(md)^{1/2}}{(dyne/cm)}$ and $E = 3$. σ is interfacial tension between water and oil, $\sigma = 42$ dynes/cm. ϕ is porosity, which is 0.2.

Relative permeability for the water and oil flow is calculated from Corey's model (Corey, 1986).

$$k_{rw} = k_{rw}^o \left(\frac{S_w - S_{wr}}{1 - S_{wr} - S_{or}} \right)^{ew}$$

$$k_{ro} = k_{ro}^o \left(\frac{1 - S_w - S_{or}}{1 - S_{wr} - S_{or}} \right)^{eo}$$

where water end point relative permeability (k_{rw}^o) is 0.3, and oil end point relative permeability (k_{ro}^o) is 0.9. Both oil and water relative permeability exponents are 2.

4.2. FINITE DIFFERENCE FORMULATIONS AND CALCULATION PROCEDURE

Mathematical formulations of mass and energy balances for oil and water flow in the reservoir and the wellbore are developed in this section. Although the formulation of mass balance is not new and commonly appears in reservoir simulation literature, it is presented here for showing the steps taken in obtaining results (temperature, pressure, and inflow rate profiles). The formulation of the energy balance is relatively new because it includes the heat resulting from fluid expansion, viscous dissipation,

convection, and conduction. Section 4.2.1 presents how to formulate the mass balance into a set of linear equations that are solved for pressure and saturations. Section 4.2.2 presents how to formulate the energy balance into a set of linear equations that are solved for temperature after pressure and saturations are known. Section 4.2.3 summarizes the calculation procedure.

4.2.1　Mass balance

Reservoir flow: For two-phase flow in a reservoir, the differential form (strong form) of the mass balance can be written as follows.

For oil:
$$-\bar{\nabla} \cdot (\rho_o \bar{u}_o) = \frac{\partial}{\partial t}(\phi \rho_o S_o)$$
(4.1)

For water:
$$-\bar{\nabla} \cdot (\rho_w \bar{u}_w) = \frac{\partial}{\partial t}(\phi \rho_w S_w)$$
(4.2)

The divergence operator ($\bar{\nabla}$) on the left side of the above equations could be expanded into any coordinate system. ϕ is the porosity of the reservoir and assumed constant in this study. $\bar{u}$ is the Darcy velocity that is extended to describe the two-phase flow by relative permeability. The subscripts "w" and "o" denote the water and oil phases, respectively. The right side of above equations can be rearranged and expressed in term of phase pressure and fluid compressibility.

For oil:
$$-\frac{1}{\rho_o}\bar{\nabla} \cdot (\rho_o \bar{u}_o) = \phi \frac{\partial S_o}{\partial t} + \phi S_o c_o \left(\frac{\partial p_o}{\partial t} \right)$$
(4.3)

For water:
$$-\frac{1}{\rho_w}\bar{\nabla} \cdot (\rho_w \bar{u}_w) = \phi \frac{\partial S_w}{\partial t} + \phi S_w c_w \left(\frac{\partial p_w}{\partial t} \right)$$
(4.4)

Equation (4.3) and (4.4) are added to eliminate the time derivative term of the saturations so that the IMPES (implicit pressure explicit saturation) formulation can be used.

$$-\frac{1}{\rho_o}\bar{\nabla}\cdot(\rho_o\bar{u}_o)-\frac{1}{\rho_w}\bar{\nabla}\cdot(\rho_w\bar{u}_w)=\phi S_o c_o\left(\frac{\partial p_o}{\partial t}\right)+\phi S_w c_w\left(\frac{\partial p_w}{\partial t}\right) \qquad (4.5)$$

For three-dimension flow in a Cartesian coordinate system, equation (4.5) can be integrated over a box-shaped control volume ($\Delta x\Delta y\Delta z$). This leads to the mass balance before taking the limit as $\Delta x, \Delta y, \Delta z$ approach zero.

$$-\frac{\Delta y\Delta z}{\rho_o}\Delta_x(\rho_o u_o)-\frac{\Delta x\Delta z}{\rho_o}\Delta_y(\rho_o u_o)-\frac{\Delta x\Delta y}{\rho_o}\Delta_z(\rho_o u_o)$$
$$-\frac{\Delta y\Delta z}{\rho_w}\Delta_x(\rho_w u_w)-\frac{\Delta x\Delta z}{\rho_w}\Delta_y(\rho_w u_w)-\frac{\Delta x\Delta y}{\rho_w}\Delta_z(\rho_w u_w) \qquad (4.6)$$
$$=\phi S_o c_o\left(\frac{\Delta x\Delta y\Delta z}{\Delta t}\right)\Delta_t p_o+\phi S_w c_w\left(\frac{\Delta x\Delta y\Delta z}{\Delta t}\right)\Delta_t p_w$$

Equation (4.6) is approximated by finite differencing. Details are given in Appendix C. With the auxiliary relations of capillary pressure ($p_c = p_o - p_w$) and saturation ($S_o + S_w = 1$), the finite-difference form of equation (4.6) is

$$A_{ijk}\,p_{wi+1,jk}^{n+1}+B_{ijk}\,p_{wi-1,jk}^{n+1}+C_{ijk}\,p_{wi,j+1,k}^{n+1}+D_{ijk}\,p_{wi,j-1,k}^{n+1}+E_{ijk}\,p_{wi+1,j,k}^{n+1}+F_{ijk}\,p_{wi-1,jk}^{n+1}$$
$$+G_{ijk}\,p_{wijk}^{n+1}=RHS_{ijk}$$

$$(4.7)$$

where the subscripts i, j, and k refer to spatial coordinates. The coefficients (A, B, C, D, E, F, G, RHS) resulting from doing a typical finite difference are presented in Appendix C.

Well grid blocks: For grid blocks containing a wellbore, equation (4.7) has to include the source/sink terms on the left side as written below.

$$A_{ijk}\, p_{wi+1,jk}^{n+1} + B_{ijk}\, p_{wi-1,jk}^{n+1} + C_{ijk}\, p_{wi,j+1,k}^{n+1} + D_{ijk}\, p_{wi,j-1,k}^{n+1} + E_{ijk}\, p_{wi+1,j,k}^{n+1} + F_{ijk}\, p_{wi-1,jk}^{n+1}$$
$$+ G_{ijk}\, p_{wijk}^{n+1} + q_{oiJK} + q_{wiJK} = RHS_{ijk}$$

(4.8)

where the subscript J and K denote the well grid blocks. The production term, q, represents volume produced at reservoir condition, per unit time. The relationship between volumetric flow rate, grid block pressure, and wellbore pressure is expressed as

$$q_{oiJK} = -PI_o\left(p_{wiJK}^{n+1} + p_{ciJK} - p_{well,i}^{n+1}\right)$$ (4.9)

$$q_{wiJK} = -PI_w\left(p_{wiJK}^{n+1} - p_{well,i}^{n+1}\right)$$ (4.10)

$$PI_l = \frac{2\pi\sqrt{k_y k_z}\,\Delta x\, k_{rl}}{\mu \ln\left(\dfrac{r_e}{r_w}\right)} \qquad \text{where } l = o, w$$ (4.11)

$$r_e = 0.28 \frac{\left[\left(\dfrac{k_z}{k_y}\right)^{\frac{1}{2}}\Delta y^2 + \left(\dfrac{k_y}{k_z}\right)^{\frac{1}{2}}\Delta z^2\right]^{\frac{1}{2}}}{\left(\dfrac{k_z}{k_y}\right)^{\frac{1}{4}} + \left(\dfrac{k_y}{k_z}\right)^{\frac{1}{4}}}$$ (4.12)

where PI_l is the phase productivity index. We use an expression developed by Peaceman (1983) to represent effective drainage radius (r_e) in the well grid blocks. Once we substitute equations (4.9) and (4.10) into the equation (4.8), the unknowns are the pressure in the grid blocks and the wellbore pressure. Thus, the wellbore flow is required to describe the pressure in the wellbore.

Wellbore flow: For wellbore flow, we use the model developed by Yoshioka *et al.* (2005) given as

$$\frac{dp_{well}}{dx} = -\frac{\rho_m v_m^2 f_m}{r_w} - \frac{d}{dx}\left(\rho_m v_m^2\right) - \rho_m g \sin\theta \tag{4.13}$$

The right side of the equation (4.13) is evaluated from a previous iteration. The finite-difference form of equation (4.13) is

$$p_{well,i+1}^{n+1} - p_{well,i}^{n+1} = R_i^n \tag{4.14}$$

Equation (4.14) only describes the difference between pressure at two points, so we need another equation, which is a well constraint. In a total rate-constrained well, we have an additional equation written as

$$q_{total} = \sum_{i=1}^{I_{max}} q_{oiJK} + \sum_{i=1}^{I_{max}} q_{wiJK} \tag{4.15}$$

where I_{max} is the maximum number of grid blocks in x-direction (along the well). J_{max} is the maximum number of grid blocks in y-direction (perpendicular to the well). K_{max} is the maximum number of grid blocks in z-direction (vertical depth).

Set of linear equations: In solving a set of linear equations, the total number of unknowns must be the same as the total number of equations.   In this set, the unknowns are water pressure of each grid block and wellbore pressure.   Below is the summary of equations and unknowns.

Unknowns:
1. Water pressure in grid blocks = $I_{max} \times J_{max} \times K_{max}$ unknowns
2. Wellbore pressure = I_{max} unknowns

Total number of unknowns = $I_{max} \times J_{max} \times K_{max} + I_{max}$

Equations:
1. Reservoir flow in all grid blocks = $I_{max} \times J_{max} \times K_{max}$ equations
   [from equations (4.7) and (4.8)]

2. Wellbore flow = $I_{max} - 1$ equations
   [from equation (4.14)]

3. Well constraint = 1 equation
   [from equation (4.15)]

Total number of equations = $I_{max} \times J_{max} \times K_{max} + I_{max}$

Once grid block and wellbore pressure are known, water saturations are determined explicitly from the water mass balance equation (4.4).   This solution method is also known as Implicit Pressure Explicit Saturation (IMPES).

4.2.2 Energy balance

Reservoir flow: For non-isothermal flow in a reservoir, the general energy balance that describes multi-phase flow is given in the literature (Lake, 1989). We begin with this general energy balance, and rearrange the equation to express it in terms of temperature and pressure. The general energy balance without kinetic energy is written as below.

$$\bar{\nabla} \cdot \left[\sum_{l=1}^{N_p} \rho_l \bar{u}_l (H_l - gD) \right] - \bar{\nabla} \cdot \left(K_{Tt} \cdot \bar{\nabla}T \right) = -\frac{\partial}{\partial t} \left[\phi \sum_{l=1}^{N_p} \rho_l S_l U_l + (1-\phi)\rho_s U_s + \rho g D \right]$$

(4.16)

where l denotes the water and oil phases for $N_p = 2$.

To avoid writing unnecessarily long equations, we first simplify the equation (4.16) to single-phase flow and then present a derivation. Equation (4.16) for $N_p = 1$ is

$$\bar{\nabla} \cdot \left[\rho \bar{u} H + \rho \bar{u} g D \right] - \bar{\nabla} \cdot \left(K_{Tt} \cdot \bar{\nabla}T \right) = -\frac{\partial}{\partial t} \left[\phi \rho U + (1-\phi)\rho_s U_s + \rho g D \right] \qquad (4.17)$$

On the right side of the equation (4.17), we can replace the internal energy by enthalpy from the relation, $\rho U = \rho H - p$. The equation becomes

$$\rho \bar{u} \cdot \bar{\nabla} H + H \bar{\nabla} \cdot (\rho \bar{u}) + \bar{\nabla} \cdot \rho \bar{u} g D - \bar{\nabla} \cdot \left(K_{Tt} \cdot \bar{\nabla}T \right) = -\frac{\partial}{\partial t} \left[\phi (\rho H - p) + (1-\phi)\rho_s U_s + \rho g D \right]$$

(4.18)

Substituting the mass balance , $\bar{\nabla} \cdot (\rho \bar{u}) = -\phi \frac{\partial \rho}{\partial t}$, into the second term, equation (4.18) becomes

$$\rho\bar{u}\cdot\bar{\nabla}H + H\left(-\frac{\partial}{\partial t}\phi\rho\right) + \bar{\nabla}\cdot\rho\bar{u}\,gD - \bar{\nabla}\cdot\left(K_{Tt}\cdot\bar{\nabla}T\right)$$

$$= -\phi\rho\frac{\partial H}{\partial t} - H\frac{\partial}{\partial t}\phi\rho + \frac{\partial}{\partial t}\phi P - (1-\phi)\rho_s\frac{\partial U_s}{\partial t} - \frac{\partial}{\partial t}\rho gD \tag{4.19}$$

We assume that the temperature of the flowing fluid is the same as the temperature of the rock $(T = T_s)$. The internal energy of the rock can be expressed in terms of the temperature as $\Delta U_s \cong \Delta H_s = C_{ps}\Delta T$. The fluid enthalpy is also replaced by the definition of C_p and Maxwell's relation of thermodynamics. Equation (4.19) becomes

$$\rho\bar{u}C_p\cdot\bar{\nabla}T - \beta T\bar{u}\cdot\bar{\nabla}P + \bar{u}\cdot\bar{\nabla}P + \bar{\nabla}\cdot\left(K_{Tt}\cdot\bar{\nabla}T\right) + \bar{\nabla}\cdot\left(\rho\bar{u}\,gD\right)$$

$$= -[(1-\phi)\rho_s C_{ps} + \phi\rho C_p]\frac{\partial T}{\partial t} + \phi\beta T\frac{\partial T}{\partial t} + \phi\beta T\frac{\partial p}{\partial t} + \phi\beta T\frac{\partial p}{\partial t} - \frac{\partial}{\partial t}\rho gD \tag{4.20}$$

For oil-water flow, the final equation to be discretized is

$$(\rho_o\bar{u}_o C_{po} + \rho_w\bar{u}_w C_{pw})\bar{\nabla}T - \left(\beta_o\bar{u}_o\cdot\bar{\nabla}p_o + \beta_w\bar{u}_w\cdot\bar{\nabla}p_w\right)T - \bar{\nabla}\cdot\left(K_{Tt}\cdot\bar{\nabla}T\right) + \bar{u}_o\cdot\bar{\nabla}p_o$$

$$+ \bar{u}_w\cdot\bar{\nabla}p_w + \bar{\nabla}\cdot\left(\rho_o\bar{u}_o gD + \rho_w\bar{u}_w gD\right) = -[(1-\phi)\rho_s C_{ps} + \phi(S_o\rho_o C_{po} + S_w\rho_w C_{pw})]\frac{\partial T}{\partial t}$$

$$+ T\left(S_o\beta_o\phi_o\frac{\partial p_o}{\partial t} + S_w\beta_w\phi\frac{\partial p_w}{\partial t}\right) - \frac{\partial}{\partial t}\left(S_o\rho_o gD + S_w\rho_w gD\right) \tag{4.21}$$

Equation (4.21) will be approximated using finite difference. Details are given in Appendix D. The finite-difference form of the equation (4.21) is

$$A_{ijk}T^{n+1}_{i+1,jk} + B_{ijk}T^{n+1}_{i-1,jk} + C_{ijk}T^{n+1}_{i,j+1,k} + D_{ijk}T^{n+1}_{i,j-1,k} + E_{ijk}T^{n+1}_{i+1,j,k} + F_{ijk}T^{n+1}_{i-1,jk} + G_{ijk}T^{n+1}_{ijk}$$
$$= RHS_{ijk}$$

where the subscript i, j, and k refer to spatial coordinates. The coefficients (A, B, C, D, E, F, G, RHS) resulting from doing a typical finite difference presents in Appendix D.

Well grid blocks: For grid blocks containing a wellbore, equation (4.22) must include source/sink terms on the left side as written below.

$$A_{ijk}T_{i+1,jk}^{n+1} + B_{ijk}T_{i-1,jk}^{n+1} + C_{ijk}T_{i,j+1,k}^{n+1} + D_{ijk}T_{i,j-1,k}^{n+1} + E_{ijk}T_{i+1,j,k}^{n+1} + F_{ijk}T_{i-1,jk}^{n+1} + G_{ijk}T_{ijk}^{n+1}$$
$$+ q_{iJK}^{energy} = RHS_{ijk}$$

(4.23)

where

$$q_{iJK}^{energy} = -\left[K_{Tt}\left(\frac{2\pi\Delta x}{\ln(r_e/r_w)} \right) - \left(q\rho C_p\right)_T \right]\left(T_{iJK} - T_{well,i}\right)$$

(4.24)

$$\left(q\rho C_p\right)_T = q_{oiJK}\rho_o C_{po} + q_{wiJK}\rho_w C_{pw}$$

In equations (4.23) and (4.24), the subscripts J and K denote the well grid blocks.   We use an expression developed by Peaceman (1983) to represent radius (r_e) in well grid blocks given by the equation (4.12).   Once we substitute equation (4.24) into equation (4.23), the only unknowns are the temperature in the grid blocks and the wellbore temperature.   Thus, a non-isothermal wellbore flow model is required to describe the temperature in the wellbore.

Wellbore flow: For non-isothermal wellbore flow, the steady-state energy balance is given by Yoshioka *et al*. (2005) below.

$$\frac{dT_{well}}{dx} = \frac{2(\rho v C_p)_{T,I}}{r_w(\rho v C_p)_T}(T_{iJK} - T_{well}) + \frac{(\rho v C_p C_{JT})_T}{(\rho v C_p)_T}\frac{dp}{dx} + \frac{(\rho v)_T}{(\rho v C_p)_T}g\sin\theta$$

(4.25)

where

$$(\rho v)_T = \sum_i \rho_i v_i y_i$$

$$(\rho v C_p)_T = \sum_i \rho_i v_i y_i C_{p,i}$$

$$(\rho v C_p C_{JT})_T = \sum_i \rho_i v_i y_i C_{p,i} C_{JT,i}$$

(4.26)

An additional equation comes from the fact that inflow temperature is equal to wellbore temperature at the toe end ($i = 1$) of the horizontal well.

$$T_{well,1} = T_{1,JK}$$

(4.27)

Set of linear equations: In solving a set of linear equations, the total number of unknowns must be the same as the total number of equations.   In this set, the unknowns are temperature of each grid block and wellbore temperature.   Below is the summary of equations and unknowns.

Unknowns:

1.   Temperature in all grid blocks = $I_{max} \times J_{max} \times K_{max}$ unknowns

2.   Wellbore temperature = I_{max} unknowns

Total number of unknowns = $I_{max} \times J_{max} \times K_{max} + I_{max}$

Equations:
1.   Reservoir flow in all grid blocks = $I_{max} \times J_{max} \times K_{max}$ equations
     [from equations (4.22) and (4.23)]

2. Wellbore flow = $I_{max} - 1$ equations
   [from equation (4.25)]

3. A constraint = 1 equation
   [from equation (4.27)]

Total number of equations = $I_{max} \times J_{max} \times K_{max} + I_{max}$

Note that I_{max} is the maximum number of grid blocks in the x-direction (along the well). J_{max} is the maximum number of grid blocks in the y-direction (perpendicular to the well). K_{max} is the maximum number of grid blocks in the z-direction (vertical depth).

4.2.3 Calculation procedure

The calculation procedure is presented in Figure 4.2. We first initialize water pressure at static equilibrium at which the water pressures are functions of the elevation only. Water in the reservoir is initialized at irreducible water saturation. Initial temperature is at geothermal temperature with a gradient of 0.01 ^{o}F/ft, ($\frac{dT}{dz}$). The initialization is for all grid blocks and inside the wellbore. Next, we calculate fluid properties, and velocity and friction factor inside the wellbore. After that, water pressure is calculated from the total (water and oil) mass balance, equation (4.5). After the water pressure solution is obtained, the water saturation is explicitly updated by substituting the results into the water mass balance, equation (4.4), and the capillary pressure is calculated according to the new water saturation. When all the pressures and saturations are known, the temperature is explicitly calculated from the energy balance, equation (4.21). The procedure is then repeated for the next time step.
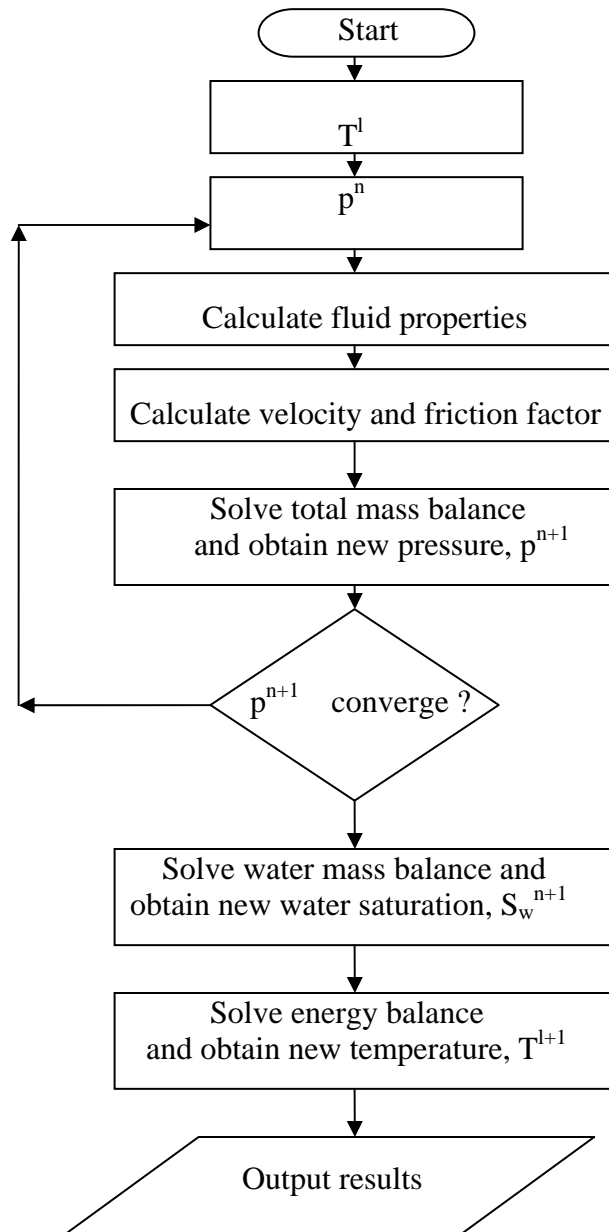
Figure 4.2   Flow chart of the calculation procedure.

In solving the mass balance for the next iteration of pressure, we used the Newton-Raphson method. The method is discussed below.

Let $\tilde{x}$ be an unknown column matrix. We are seeking the solution, $\tilde{x}^{n+1}$. We have an equation in the following form.

$$\tilde{A}\tilde{x} = \tilde{b} \tag{4.28}$$

where

$\tilde{A}$; square matrix

$\tilde{x}$; column matrix

$\tilde{b}$; column matrix

The structure of square matrix $\tilde{A}$ in this case is the banded matrix including extra bands from wellbore flow equations as show below.

$$\tilde{A} \cong$$

We first rearrange the equation (4.28) and solve for the changes in $\tilde{x}$.

$$\tilde{f} = \tilde{A}\tilde{x} - \tilde{b} = 0 \tag{4.29}$$

The column matrix, $\tilde{f}$, contains f_1, f_2, ..., f_{max}, which are in terms of x_1, x_2, ..., x_{max}. The changes in $\tilde{x}$ are obtained from inverting the equation below.

$$\begin{bmatrix} \dfrac{\partial f_1}{\partial x_1} & \dfrac{\partial f_1}{\partial x_2} & . & . & . & \dfrac{\partial f_1}{\partial x_{max}} \\ \dfrac{\partial f_2}{\partial x_1} & \dfrac{\partial f_2}{\partial x_2} & . & . & . & \dfrac{\partial f_2}{\partial x_{max}} \\ . \\ . \\ . \\ \dfrac{\partial f_{max}}{\partial x_1} & \dfrac{\partial f_{max}}{\partial x_2} & . & . & . & \dfrac{\partial f_{max}}{\partial x_{max}} \end{bmatrix} \begin{bmatrix} \delta x_1 \\ \delta x_2 \\ . \\ . \\ . \\ \delta x_{max} \end{bmatrix} = - \begin{bmatrix} f_1(x_1^n) \\ f_2(x_2^n) \\ . \\ . \\ . \\ f_{max}(x_{max}^n) \end{bmatrix} \tag{4.30}$$

The matrix that contains the partial derivatives is called the Jacobian matrix. Instead of taking the derivatives analytically, we numerically calculate each derivative from

$$\frac{\partial f_n}{\partial x_i} = \frac{f_n(x_i + \varepsilon) - f_n(x_i)}{\varepsilon} \tag{4.31}$$

where ε is a small increment $= 10^{-3}$

Finally, we can obtain $\tilde{x}^{n+1}$ from

$$\tilde{x}^{n+1} = \tilde{x}^n + \delta \tilde{x} \tag{4.32}$$

4.3 VALIDATION OF THE NUMERICAL MODEL DEVELOPED

A common practice in developing a numerical model is to validate the numerical result against an analytical solution. Validating the model is an important step, and can consume as much time as the program coding itself. Validation is necessary to ensure

that the program coding, the mathematical formulations, and the numerical solution techniques are correct. However, we do not have a direct analytical solution for temperature and pressure profiles of a horizontal well in a bottom water drive reservoir. We will validate the numerical model developed here with the analytical model developed in Chapter 3. We simplify the numerical model to match the flow geometry of the analytical model as the followings.

1. Permeability

$$k_x = 0$$
$$k_y = k_z = 50 \ md$$

2. Relative permeability

$$k_{ro} = 1$$
$$k_{rw} = 0$$

3. Capillary pressure is set to be zero ($p_c = 0$).

4. Irreducible water saturation is set to be zero ($S_{wr} = 0$).

5. No gravity effect ($g = 0$).

6. Reservoir fluid properties are evaluated at the same conditions as the analytical model, at 4,000 psi and 180 °F.

7. Boundary conditions

  - No-flow for the bottom and top boundaries

  - Pressure and temperature at external boundaries are 4,000 psi and 180 °F.

8. The accumulation terms on the right side of mass and energy balances are set to zero so that the flow is a steady-state flow.

The results from the numerical model were compared with the analytical solutions as shown in Figure 4.3. The temperature, pressure, and inflow rate profiles from both analytical and numerical models agree well with each other.
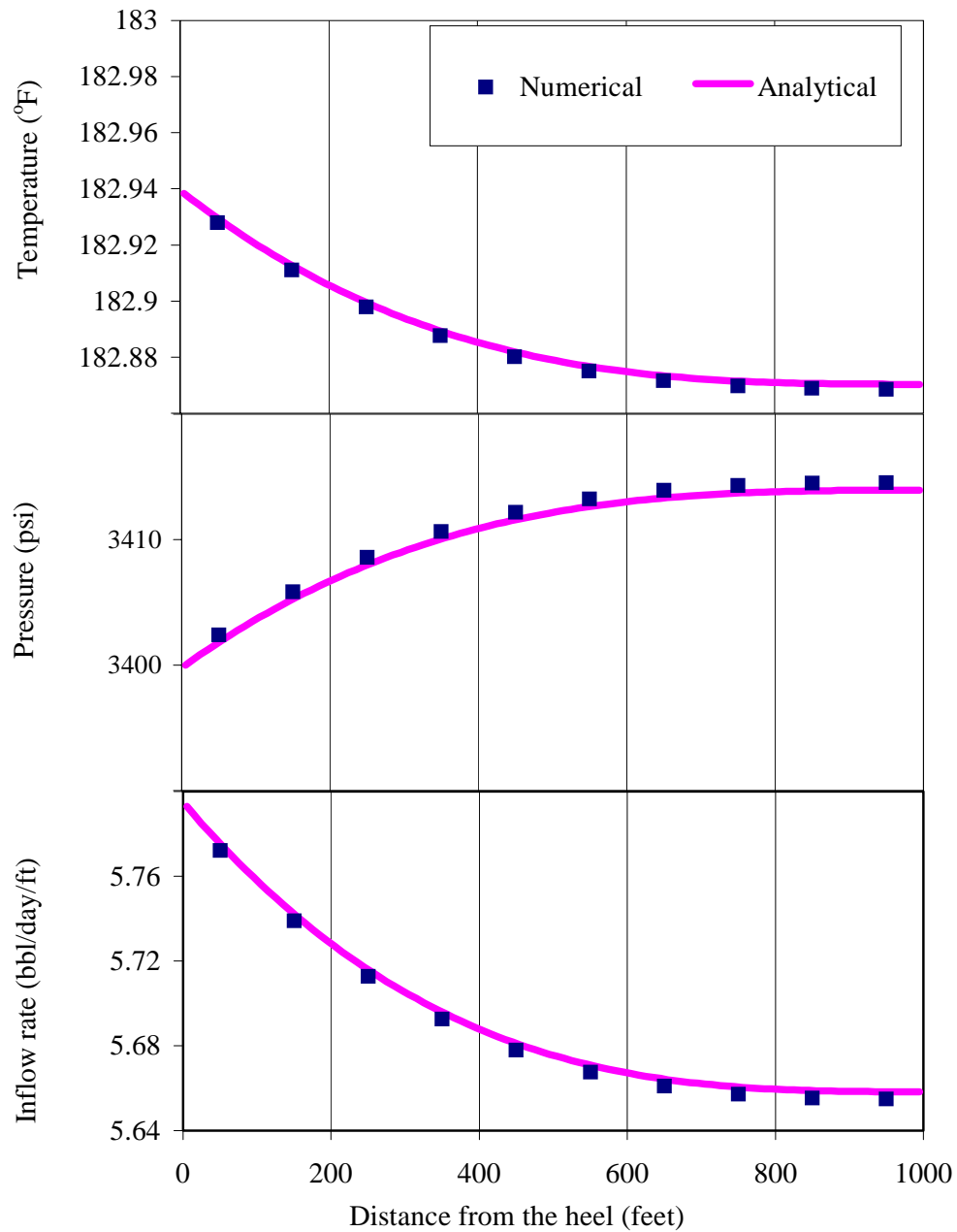
Figure 4.3   Comparison of numerical and analytical results.

Another approach that was used to validate the numerical model under the water and oil flow in a bottom water drive reservoir sketched in Figure 4.1 is to check the numerical model's mass balance calculation on the water component. We verify within the 5 percent of error that amount of water influx from the bottom is equal to amount of water produced and water remaining in reservoir for each time step.

4.4 RESULTS

Under the physical model described in Section 4.1, the oil reservoir is bounded with no-flow boundary except at the bottom of the boundary, which is initially in contact with water. The pressure and temperature at the bottom boundary are maintained at 4,000 psi and 180 ^{o}F. The temperature of the reservoir is initialized according to the geothermal gradient of 0.01 ^{o}F/ft. The reservoir is initially filled with oil while water is immobile at irreducible water saturation. We use fluid property correlations presented in Appendix A. Oil and water properties are correlated based on the oil gravity, the dissolved gas-oil ratio, the gas specific gravity, and the salinity of the water. The parameters of the numerical model are summarized in Tables 4.1 and 4.2.

Table 4.1   Wellbore and reservoir parameters

Parameters	Values
Well rate (base case), [bbl/d]	5,000
Horizontal length, [ft]	1,000
Well inside diameter, [in]	6
Relative pipe roughness	0.027
Skin factor	0
Pressure at water-oil contact (boundary condition), [psi]	4,000
Temperature at water-oil contact (boundary condition),[^{o}F]	180
Reservoir thickness, [ft]	110
Reservoir dimension, [ft x ft x ft]	1000 x 2150 x 110
Grids, [ft x ft x ft]	100 x 10 x 10

Table 4.2   Rock and fluid parameters

Parameters	Values
Porosity	0.20
Horizontal permeability (base case), [md]	50
Vertical permeability (base case), [md]	10
Irreducible water saturation	0.25
Residual oil saturation, fraction	0.1
Capillary pressure at irreducible water saturation, [psi]	11
Threshold capillary pressure, [psi]	0
Total thermal conductivity, [Btu/hr ft ^{o}F]	2
Rock density, [lb_m/ft^3]	165
Rock heat capacity, [Btu/lb_m ^{o}F]	0.22
Temperature gradient, [^{o}F/ft]	0.01
Low density oil (base case)	
Oil API	45
Dissolved gas-oil ratio, [SCF/STB]	800
Specific gravity of gas	0.75
High density oil	
Oil API	35
Dissolved gas-oil ratio, [SCF/STB]	500
Specific gravity of gas	0.75
Water	
Salinity, [wt. %]	5

In the following sections, we will present example cases using the developed numerical temperature model. We focus the study on how the temperature changes along a horizontal well before and after water breakthrough from a bottom water aquifer. Since the application of the study is to use DTS for monitoring a production well, we are interested in examining the temperature changes over the span of several days, a length of time that is much greater than the response time of the DTS.

We will show three main effects on the time-varying temperature profiles. A base case is fixed at a total (oil+water) rate of 5,000 bbl/d, horizontal permeability of 50 md, vertical permeability of 10 md, and an oil gravity of 45 $^\text{o}$API. We then compare the base case results with other cases, which are (1) total rate of 3,000 bbl/day, (2) a large permeability zone in the middle section of the reservoir, (3) an oil gravity of 35 $^\text{o}$API

4.4.1 Effect of flow rates on the temperature profiles

For the base case, Figure 4.4 shows snapshots of temperature, pressure and inflow water rate profiles along the horizontal well at three elapsed times. The toe-to-heel pressure drop is about 12 psi, most of which occurs around the heel section (first 300 ft of horizontal wellbore). Because of this additional drawdown imposed on the reservoir, the inflow profiles of water and oil also increase toward the heel as shown in Figure 4.5. Similar plots for the case of 3,000 bbl/d total rate are shown in Figure 4.6 and 4.7. Here, a smaller pressure drop is observed. As a result, the size of a temperature change is smaller than for the base case. The temperature change for 5,000 bbl/d case is in the range of 179.4-180.6 $^\text{o}$F while the temperature change for the 3,000 bbl/d case is in the range of 179.4-180.2 $^\text{o}$F. The size of the temperature change is a strong function of flow rate. The strong sensitivity of the temperature changes to production rate demonstrates that it is possible to evaluate the amount of inflow rate from the temperature profiles if

the rate is large. However, the results also show that it will be difficult to detect a temperature change in a small rate well.

To compare the two cases in time, we plotted temperature, pressure and inflow rate at the mid point of the horizontal well in Figure 4.8. After a few days of production, a relatively small pressure drop with time is observed. When the water breaks through, the reduction of total fluid mobility increases the drawdown to maintain a constant total rate of production. The distinguishing feature is the temperature versus time plot that shows different slopes before and after water breakthrough time. The slope of the temperature after breakthrough is less than the one before breakthrough. This is because water has a greater density and heat capacity than oil, causing the Joule-Thomson coefficient of water to be less than oil. The water-oil mixing property has caused the slope to decrease, at least for this type of fluid. This feature can be used to tell when water breakthrough occurs. Next, we reduced the total production rate to 4,000 bbl/day and 3,000 bbl/day. For the 3,000 bbl/day case we do not see the change in temperature slope because water production is not large enough to cause a significant change. The temperature gradually increases with time because friction (viscous dissipative heating) is always created when there is flow. This is similar to entropy generation in thermodynamics.
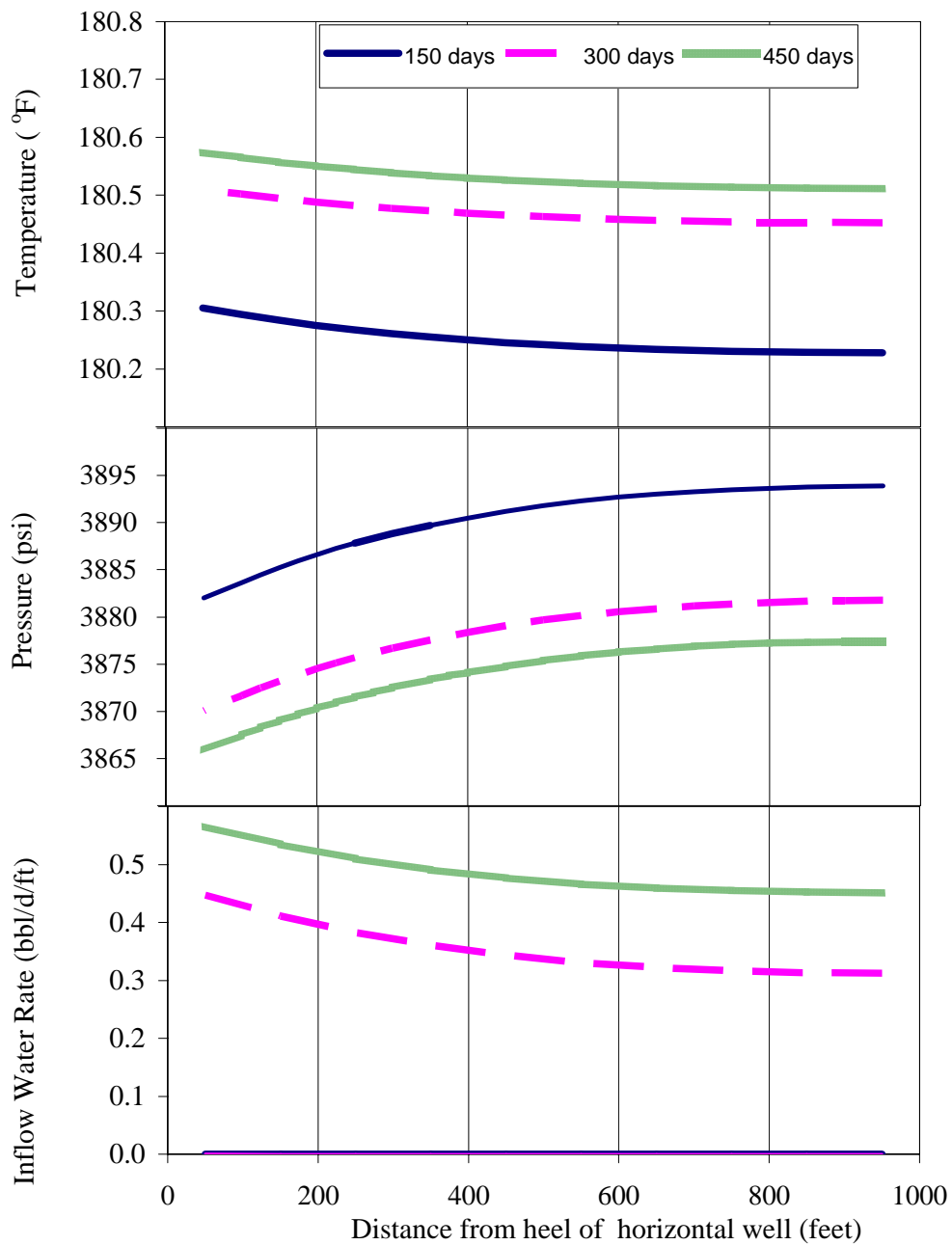
Figure 4.4   Temperature, pressure, and inflow water rate profiles for 5,000 bbl/d total (oil+water) production rate.   Initial pressure and temperature along the well are 3,973 psi and 179.4 °F, respectively.
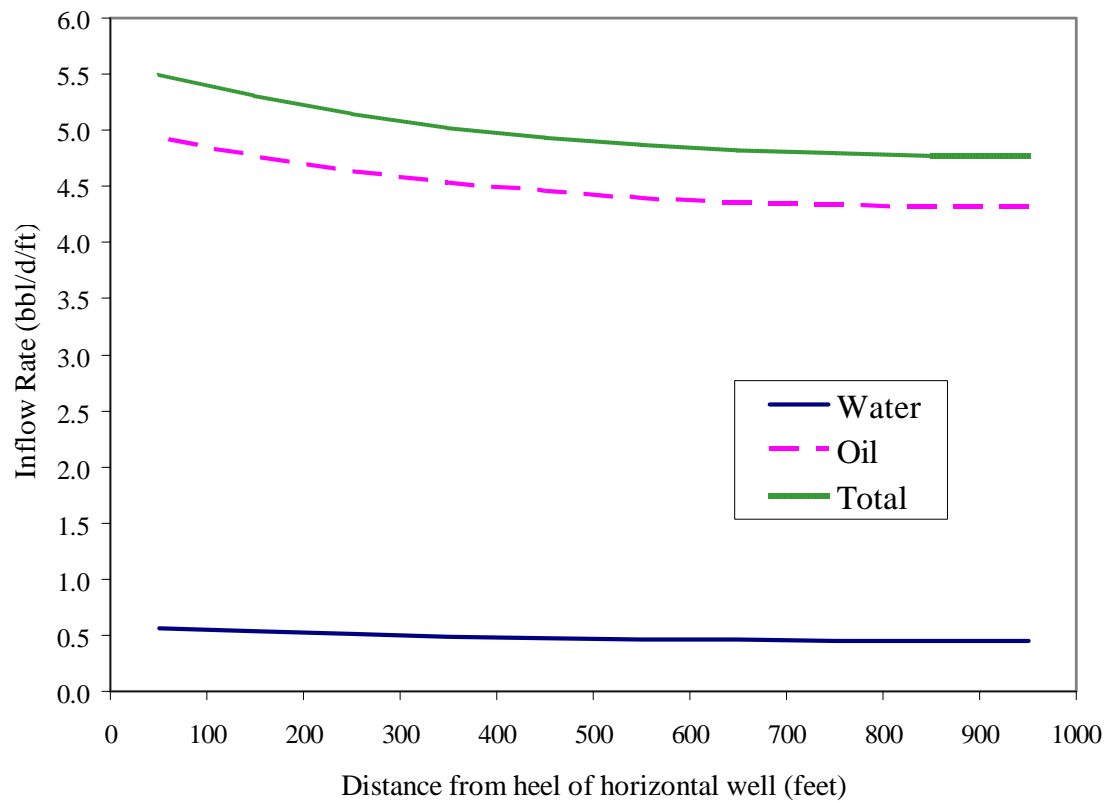
Figure 4.5   Inflow rates along the horizontal well for 5,000 bbl/d total (oil+water)
            production rate (at 450 days).
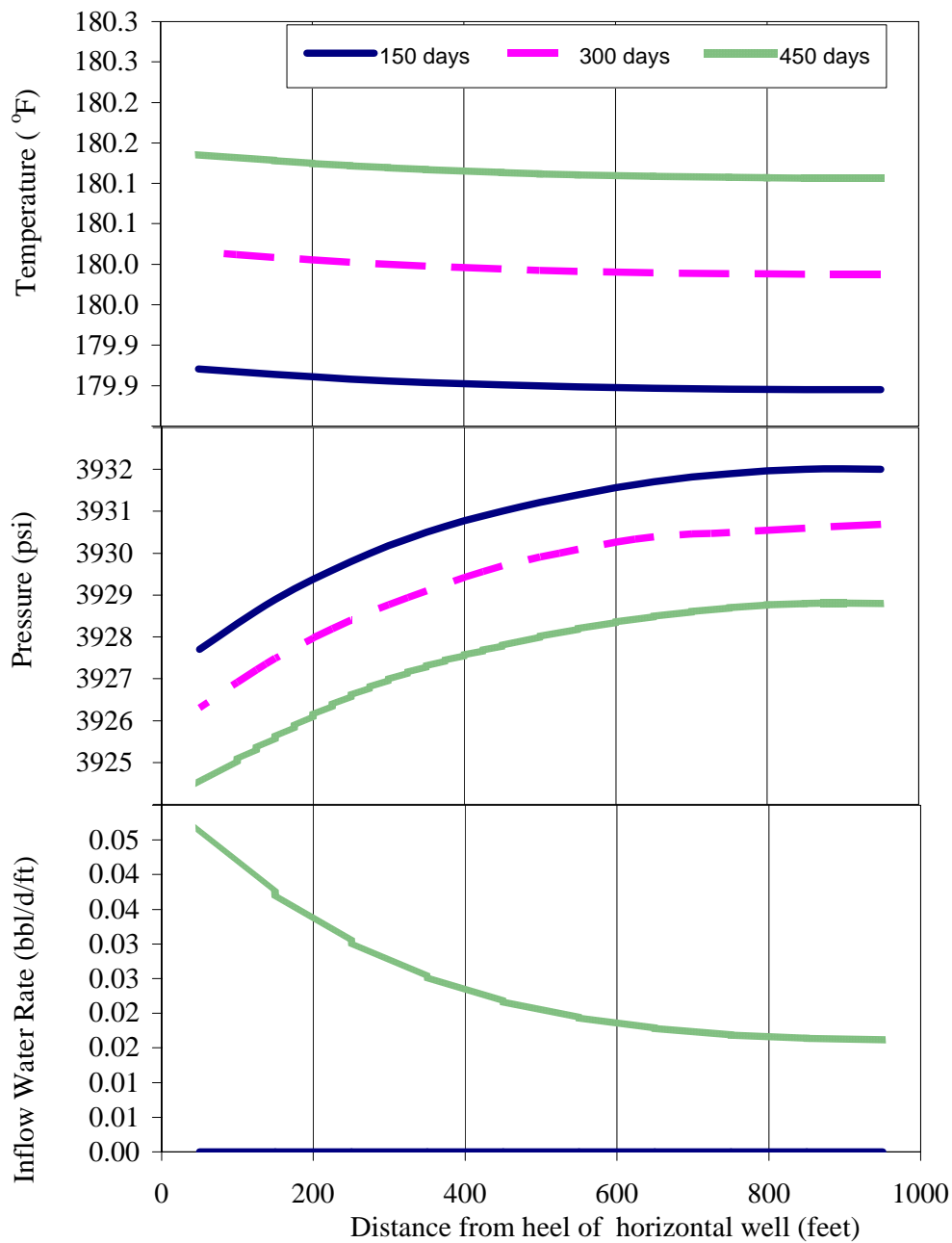
Figure 4.6   Temperature, pressure, and inflow water rate profiles for 3,000 bbl/d total (oil+water) production rate.   Initial pressure and temperature along the well are 3,973 psi and 179.4 ^{o}F, respectively.

112
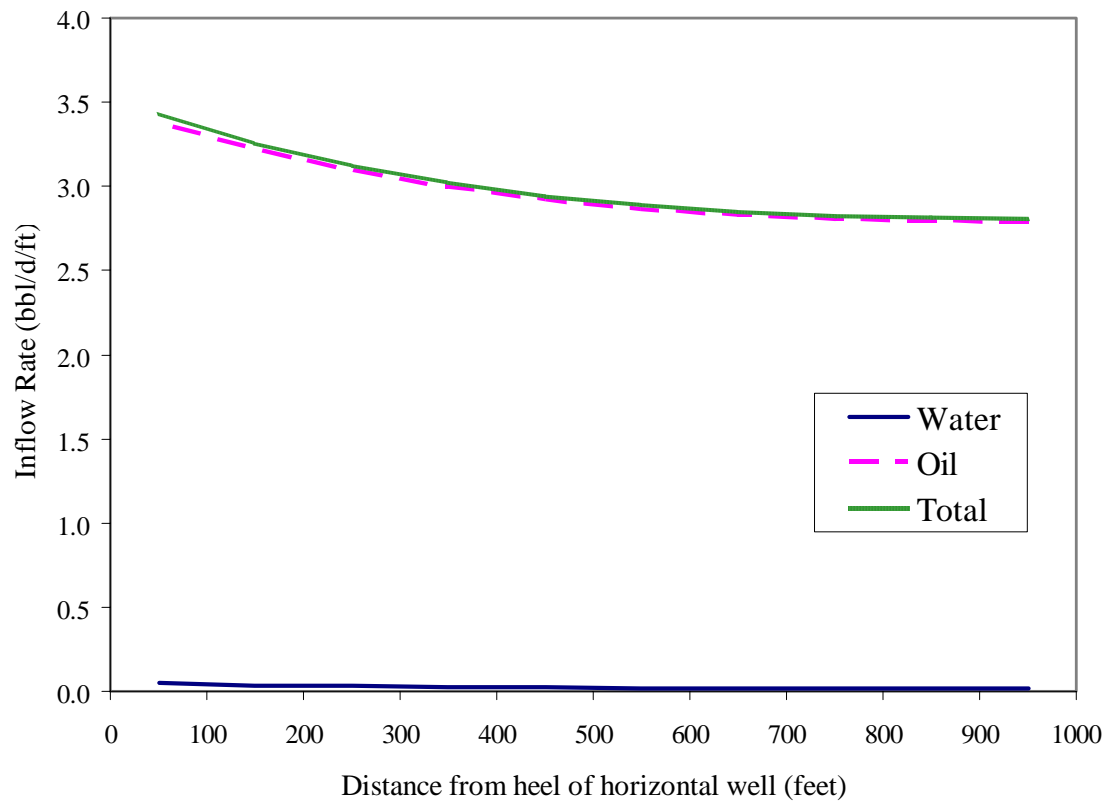
Figure 4.7   Inflow rates along the horizontal well for 3,000 bbl/d total (oil+water)
              production rate (at 450 days).

113

Figure 4.8   Wellbore temperature, wellbore pressure and inflow rate changes with time
for different production rates.   (at center of horizontal well)

114

4.4.2 Effect of large permeability zone on the temperature profiles

In this section, we will examine the wellbore temperature behavior where a large permeability compartment is in the middle 300 ft of the reservoir (k_h=100 md, k_z=20 md), from the interval from 400 to 700 feet from the heel of the well. The rest of the reservoir is the same as the base case (k_h=50 md, k_z=10 md). Figure 4.9 illustrates this case by showing the water saturation distribution in the reservoir at 170 days of production when the warm water from the bottom of reservoir reaches the middle intervals of the well, but water has not arrived in the rest of the intervals. Figure 4.10 shows snapshots of temperature, pressure, and inflow water rate profiles along the horizontal well at three elapsed times. Figure 4.11 shows the details of water, oil, and total inflow profiles at 450 days. As time progresses, the pressure profiles do not show an abrupt change along the well, which suggests that the snapshots of pressure profiles alone for this case cannot identify the high permeability zone.

On the other hand, the temperature profiles show a noticeable change in slope. For this example case, we therefore can conclude that the location of a high permeability zone (also the large flow rate) is certainly identified as the zone over which the slope of the temperature profiles is greater than the rest of the horizontal intervals that are producing at smaller inflow rates. This implies that locations of fractures (i.e. large permeability zone) can also be detected by the temporal change of the temperature profiles.

Figure 4.12 shows the plots of wellbore temperature, wellbore pressure and inflow water rate versus time at different locations along the well. We can see different slopes (dT/dt) before and after water breakthrough time in the near toe curve, but the slope differences are difficult to see in the middle and near heel curves. This is because the wellbore temperature contains the combined information both from inflow and from

the upstream wellbore flow.   The upstream wellbore flow tends to be dominant when moving toward the heel of the horizontal well.
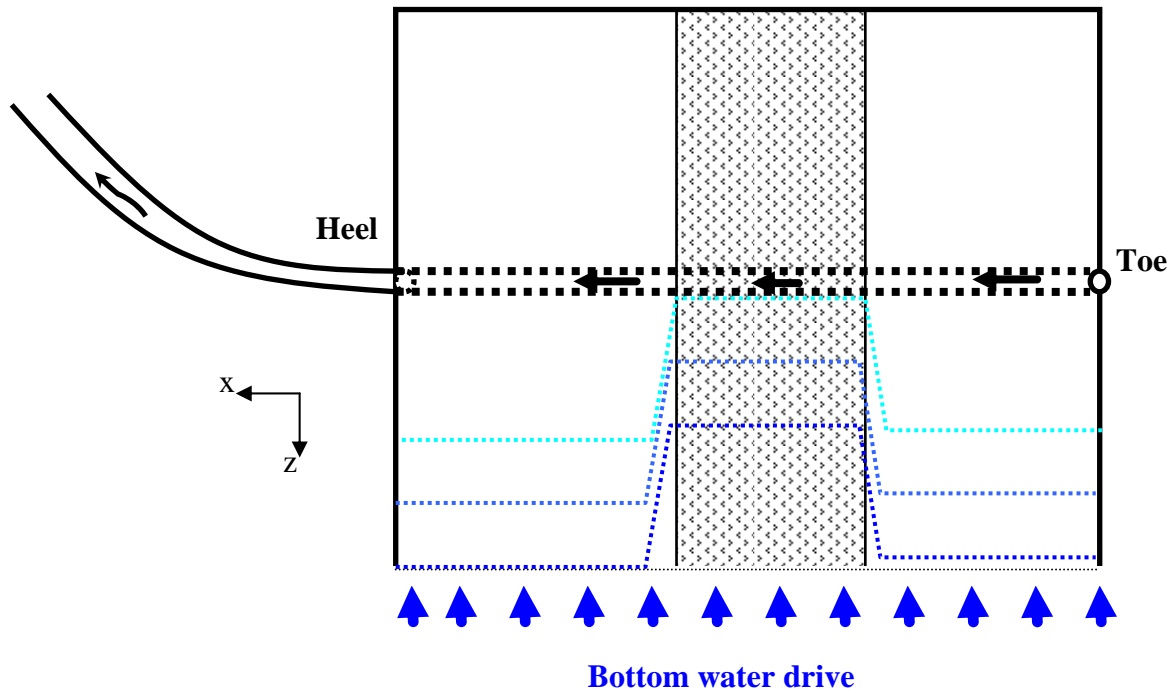
Figure 4.9   Water saturation distribution around well at 170 days of production.
Middle interval (400-700 ft shaded) k_h = 100 md/ k_z = 20 md; end intervals
k_h = 50 md/ k_z = 10 md.   Each dotted line represents an equal water
saturation in the reservoir.
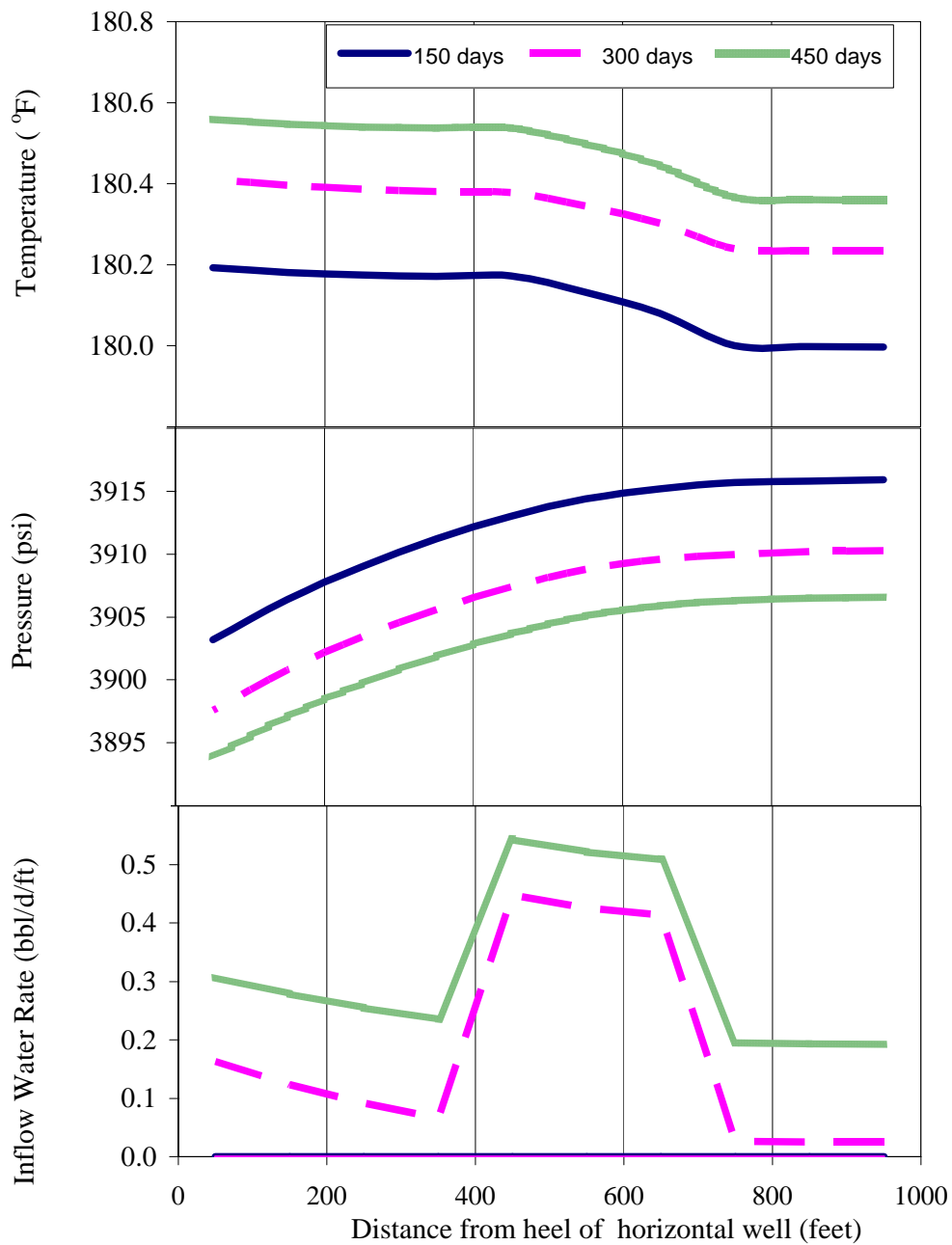
Figure 4.10   Temperature, pressure, and inflow water rate profiles for large permeability in middle section (400 -700 ft) of well.   Middle interval k_h=100 md/ k_z=20 md, end intervals k_h=50 md/ k_z=10 md.
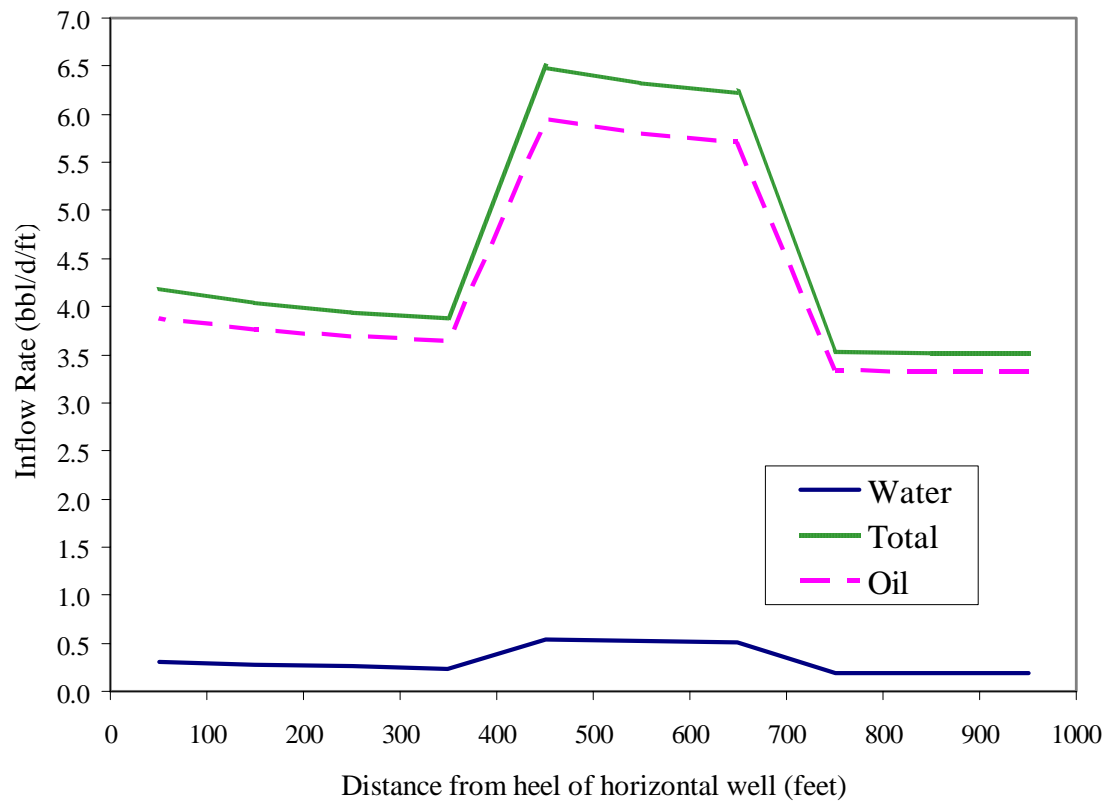
Figure 4.11   Inflow rates along horizontal well for large permeability in middle section
(400-700 ft) of well (at 450 days).   Middle interval k_h=100 md/ k_z=20
md, end intervals k_h=50 md/ k_z=10 md.
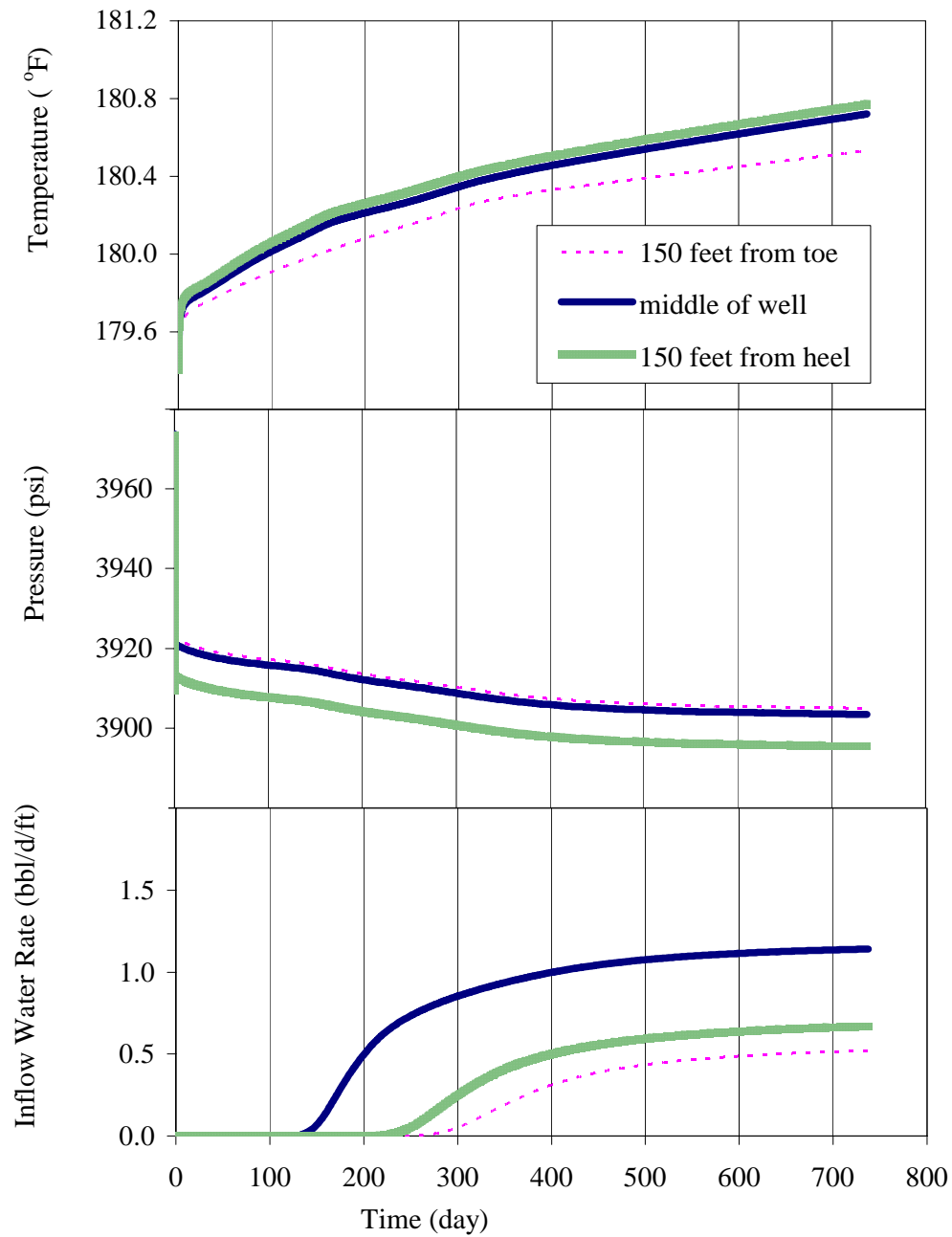
Figure 4.12   Wellbore temperature, wellbore pressure and inflow rate changes with time for different locations.   Middle interval k_h=100 md/ k_z=20 md, end intervals k_h=50 md/ k_z=10 md.

4.4.3 Effect of oil type on the profiles

The purpose here is to assess the size of the temperature change resulting from different types of oil. We model the oil properties by using commonly known correlations based on the oil gravity (^{o}API), dissolved gas-oil ratio, and gas specific gravity. Two oils of different densities are chosen for this purpose. Table 4.2 provides the fluid properties. Figure 4.13 shows profiles for an oil gravity of 35°API. Compared to the base case (Figure 4.4), the shapes of the profiles are similar, but the magnitude of changes is larger by a factor of two.

Figure 4.14 is a comparison of the base case (45 ^{o}API) and the denser-oil case (35 ^{o}API) with time. As production time progresses, wellbore pressure for the 35 ^{o}API oil case drops about 120 psi more than for the base case. The reduction of mobility caused by the larger viscosity oil results in greater drawdown to maintain a constant well rate. Temperature gradually increases with time, and the temperature increase reflects the pressure drop, notably where the wellbore pressure drops when water breaks through. After water breakthrough, the rate of temperature increase is smaller than before water breakthrough when only oil flows into the wellbore. The temperature difference between the two cases is quite large, which means that fluid properties have a great impact on temperature profiles. This suggests that a good description of fluid properties is required to quantitatively infer inflow rate profiles from temperature profiles.
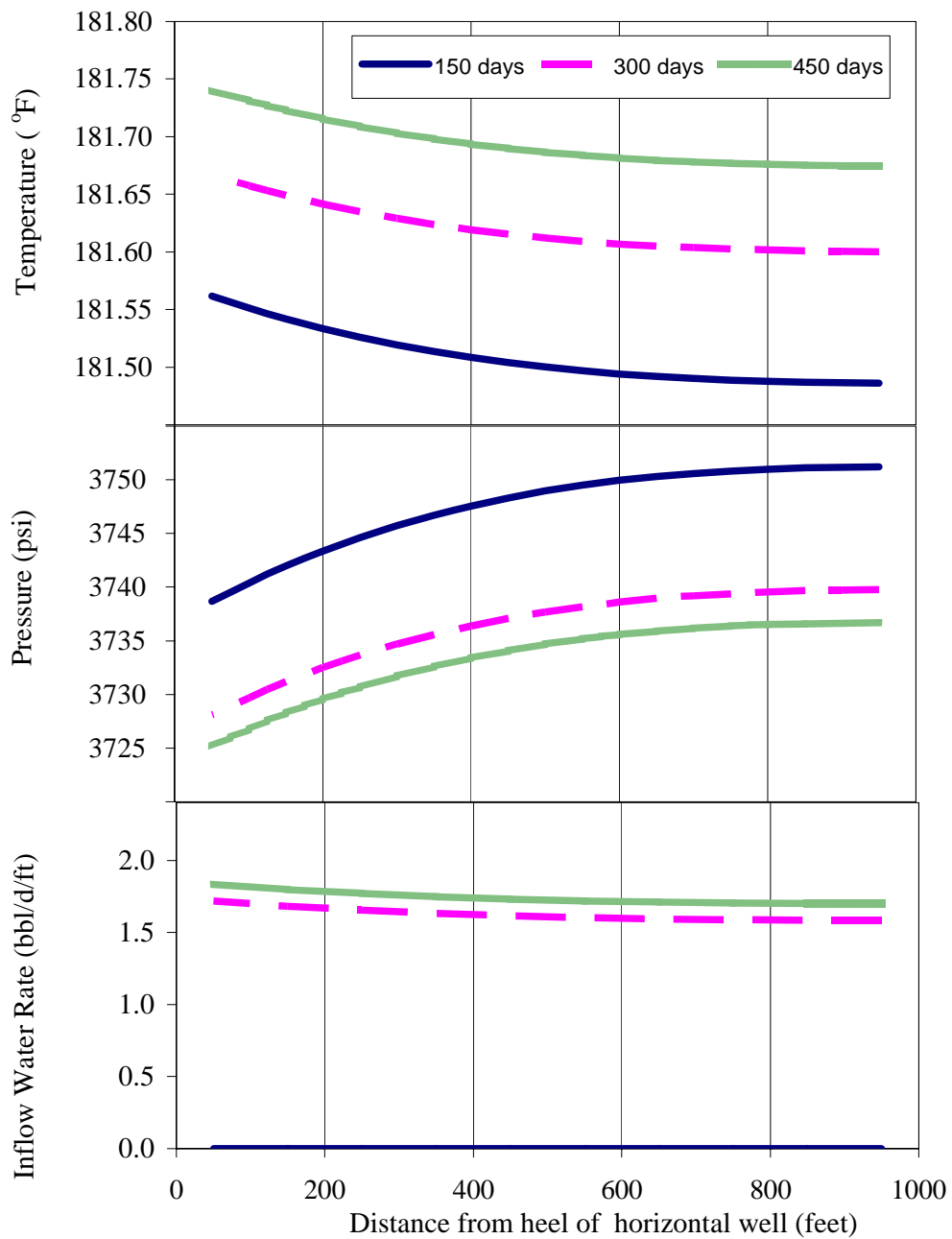
Figure 4.13   Temperature, pressure, and inflow water rate profiles for an oil gravity of 35 $^\circ$API.   Initial pressure and temperature along the well are 3,973 psi and 179.4 $^\circ$F respectively.
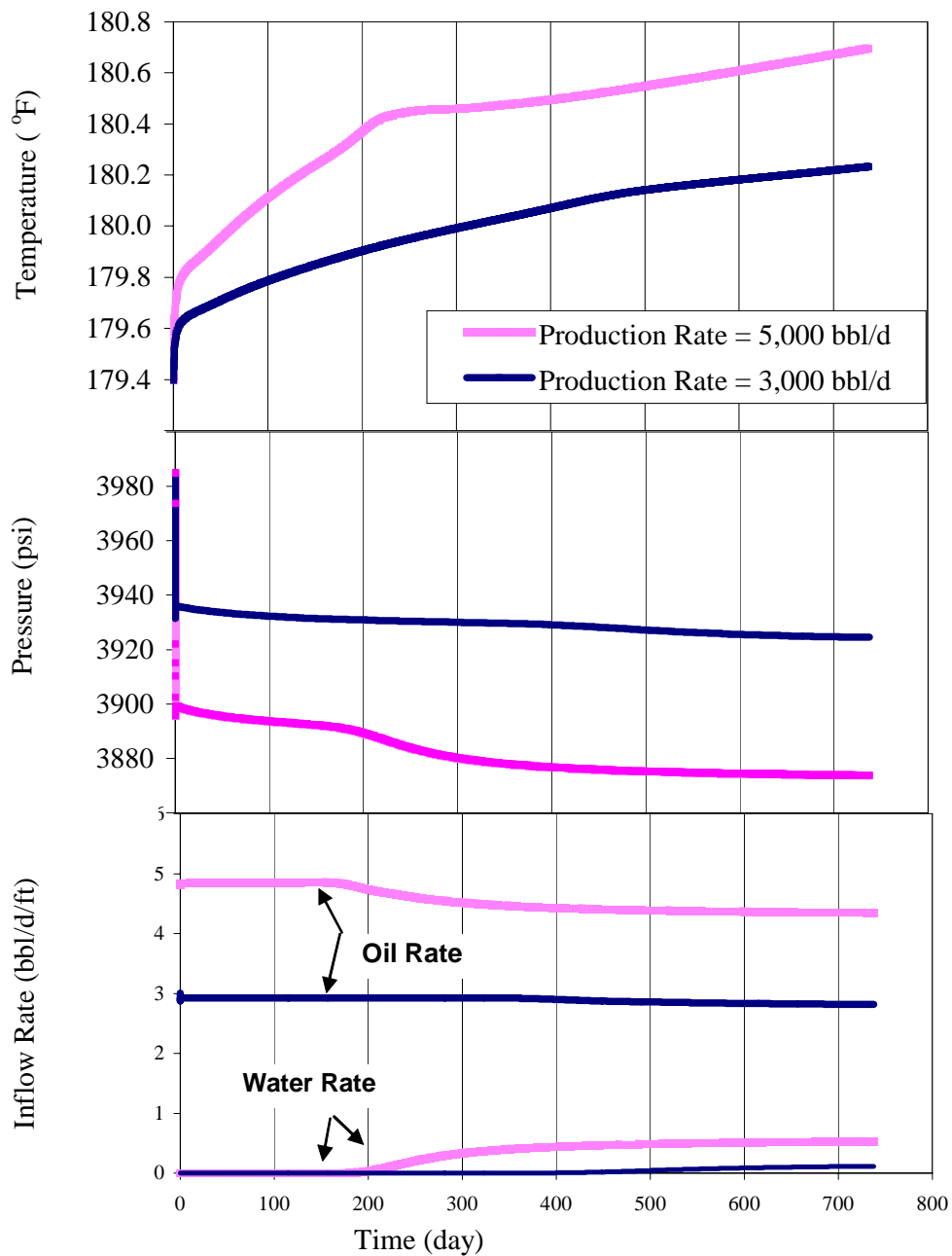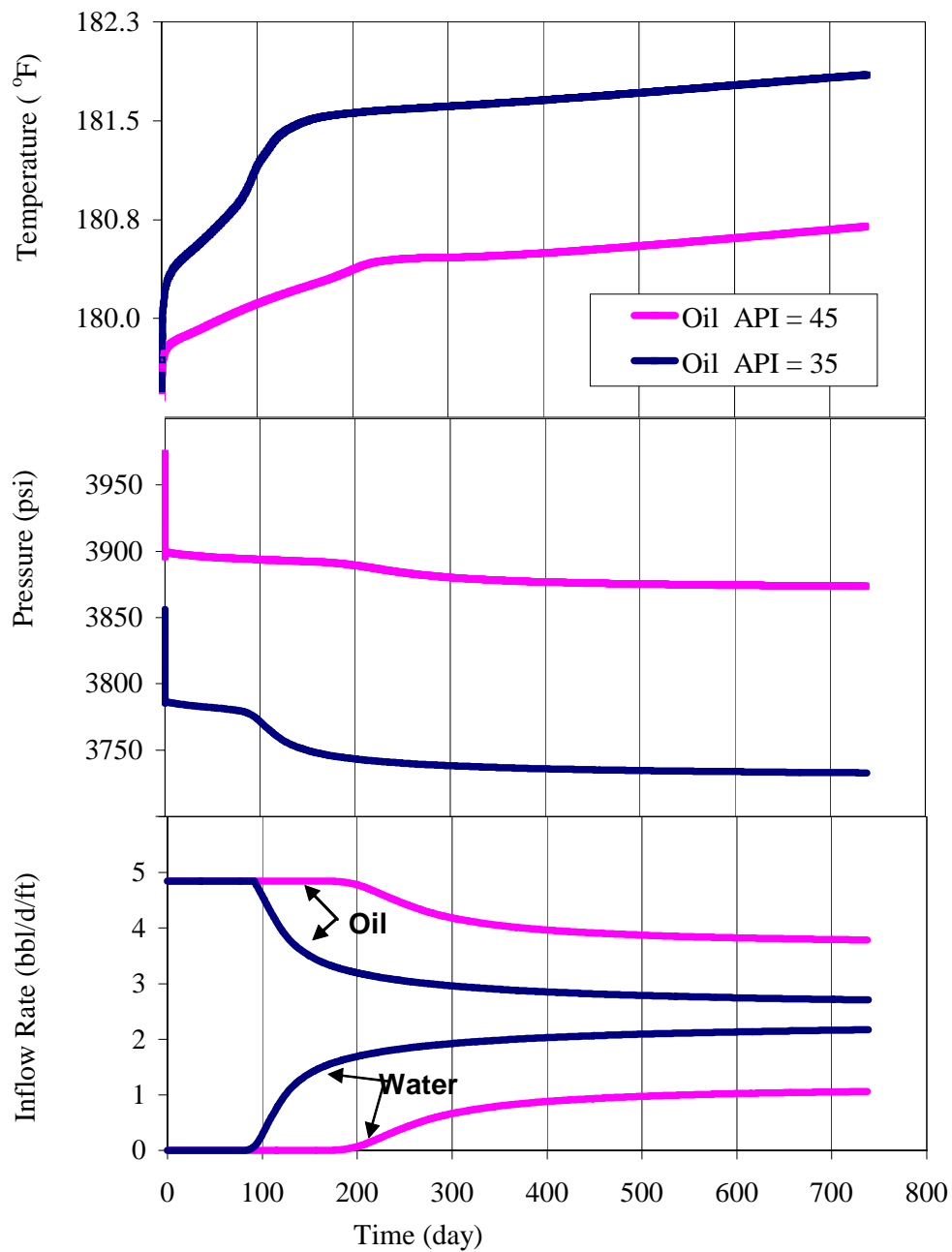
Figure 4.14   Wellbore temperature, wellbore pressure, and inflow rate changes with time for different oils. (at center of horizontal well)

CHAPTER   5

Conclusions and Recommendations

Temperature profiles of vertical wells are reasonably well understood, and are generally modeled using a radial geometry.   In recent years, however, the wide use of horizontal wells and attempts to continuously monitor horizontal wells by distributed temperature sensors (DTS) have required that knowledge from temperature logs be adapted to the horizontal well geometry.   Two major issues must be considered when analyzing temperature profiles for a horizontal well.   First, the geothermal temperature along a horizontal well is the same; so the only temperature change is caused by heat generated from thermal expansion of a fluid and viscous dissipation during fluid flow. Second, the flow geometry is at least two dimensional, which is different from vertical wells that are typically modeled as a one-dimensional radial flow.   It is therefore important that a new temperature model be developed for a horizontal well.

We have developed a temperature prediction model for a horizontal production well.   The model accounts for subtle energy effects including fluid expansion, viscous dissipation, heat convection, and heat conduction for flow in a reservoir.   The model developed is then used to illustrate the size of the temperature changes caused by different amount and types of fluids, and to demonstrate that wellbore temperature profiles can be used to locate a zone that is producing excessive water or gas.

This chapter presents what has been found and the conclusions from various examples.   Recommendations for future research work and toward the development of DTS are listed at the end of the chapter.

5.1 CONCLUSIONS

The following conclusions have been drawn based on the results of this study.

1.   The size of temperature changes is detectable with current technology (DTS) if the production rate is large enough.   In the examples presented, oil or water can enter the wellbore 2-3 ^{o}F higher, while gas can enter with 5-6 ^{o}F lower, than the geothermal temperature.

2.   The size of the temperature changes is sensitive to the inflow rate; as a result the inflow temperature is valuable to infer the rate profile along the horizontal well.   The inflow rate profile helps to decide if reservoir stimulation is needed in a small production section of a horizontal well.

3.   The slope of a wellbore temperature profile shows a notable change when different phases (oil, water, gas) enter the wellbore, and indicates where the production of one phase starts and another phase ends.   The most abrupt change is the slope over the zone that is producing gas.   The slope change over the water zone is small but it is still within the DTS's resolution to capture; by a recent fiber-optic sensor its resolution can be as fine as 0.0045 ^{o}F for the time and spatial average of 1 hour and 50 feet if the cable range is less than 3,000 feet.   Knowing the water or gas zone helps design a means to isolate the zone via an intelligent well equipments.

4.   A no-inflow zone along the horizontal wellbore is difficult to be identified by the wellbore temperature profile because the wellbore flow tends to mask this information.

5.   The size of the temperature change is sensitive to reservoir fluid properties, especially contrasts between the properties of each phase.   This suggests that we should have an accurate fluid properties before associating the temperature data to information such as flow rate or origin of water.

124

5.2 RECOMMENDATIONS

This study is only intended to establish a basic understanding of temperature behavior under specific examples, and to assess the potential uses of DTS in monitoring a horizontal production well. A more advanced and detailed modeling could be further done as follows.

1. Represent the viscous dissipation ($-\bar{\bar{\tau}}:\bar{\nabla}\bar{v}$) by a different model from the one used in this study.

2. Develop a model to account for the fact that horizontal wells have bends and curves, and may not be in the center of a reservoir.

3. Extend the model to include the presence of formation damage, other completions, and fracture reservoir.

4. Generalize the fluid properties by using the Peng-Robinson or Redlich-Kwong-Soave equations of state as normally practiced in numerical reservoir simulation, and study the temperature behavior when the reservoir pressure is dropped below the bubble point pressure and gas evolves from oil.

5. Because of the IMPES algorithm of numerical simulation used in Chapter 4, we suppressed the stability problem by using a small time steps (1 day). To avoid the stability problem, we recommend to use the implicit pressure and saturation algorithm with explicit calculations of temperature.

As a last recommendation toward the development of DTS, we believe that it would be beneficial if the fiber-optic cable could somehow measure the inflow temperature inside the sandface; thus, the approximate inflow temperature model discussed in Section 3.3 would link directly to reservoir flow performance without having to couple with the wellbore flow effect, which tends to mask the inflow information in the wellbore temperature profiles.

Nomenclature

Specific notations are defined next to the equations in the text where they are used. If the notations are not defined in the body text, the following notations are used as defaults. The SI unit system is used here for consistency.

<u>English alphabet</u>

C_{JT} Joule-Thomson coefficient [K/Pa]

C_p specific heat capacity [J/(kg K)]

c compressibility [1/Pa]

c_t total (fluid and rock) compressibility [1/Pa]

D depth [m]

e total energy flux [J/s/m^2]

f friction factor []

f_m mixture friction factor []

g gravity acceleration [m/s^2]

H specific enthalpy [J/kg]

h reservoir thickness [m]

PI productivity index [m^3/s/Pa]

K_T thermal conductivity of fluid [J/(s m K)]

K_{Tt} total thermal conductivity of rock and fluid [J/(s m K)]

k permeability [m^2]

k_{rl} relative permeability of a phase l []

L length of well [m]

N_{Re} Reynolds number []

N_p number of phases []

p pressure [Pa]

p_c capillary pressure [Pa]

q volumetric flow rate [m^3/s]

Re   Reynolds number []

r_w well radius [feet]

S_l saturation of a phase l []

S_{wr} irreducible water saturation []

T temperature [K]

T_I inflow temperature of fluid entering a wellbore [K]

T_o temperature at external boundary of reservoir [K]

t time [s]

u Superficial velocity [m/s]

U_o overall heat transfer coefficient [J/(m^2 s K)]

U specific internal energy [J/kg]

v interstitial velocity of fluid [m/s]

V specific volume [m^3/kg]

Y length of reservoir [m]

y_l holdup of a phase l []

Greek alphabet

β thermal expansion coefficient [1/K]

μ viscosity [Pa s]

ρ density [kg/m^3]

ϕ porosity []

Φ   flow potential

θ angle from horizontal [radian]

τ stress shear tensor [Pa]

ε relative roughness []

π constant (3.1415...) []

Subscripts

g gas

I inflow

o oil

s solid part of rock

w water

well   wellbore

Superscripts

$\rightharpoonup$ vector quantity

$=$ tensor quantity

APPENDIX A

Fluid Properties

This appendix is intended to provide information about gas, oil and water properties, emphasizing only aspects that relate to the subject of this dissertation. There are many empirical correlations based on laboratory PVT analyses in the literature. We choose correlations that can be applied to the oil-field ranges of pressure and temperature. One should refer to the original literature for a clear understanding of the limitation of the correlations. The main purpose here are to show step by step how to obtain the fluid properties, and to give references to the original literature.

A.1 GAS PROPERTIES

Natural gas properties are calculated by assuming that the specific gravity of gas (γ_g), pressure and temperature are known.

A.1.1 Density of gas

Step 1: Calculate pseudocritical pressure and temperature of natural gas using Sutton's equations (Sutton, 1985).

$$p_{pc} = 756.8 - 131.0\gamma_g - 3.6\gamma_g^2 \tag{A.1}$$

$$T_{pc} = 169.2 + 349.5\gamma_g - 74.0\gamma_g^2 \tag{A.2}$$

where γ_g is specific gravity of gas. Pressure and temperature are psia, and $^\circ R$.

Step 2: Calculate pseudo-reduced pressure and temperature.

$$p_{pr} = \frac{p}{p_{pc}} \tag{A.3}$$

$$T_{pr} = \frac{T}{T_{pc}} \tag{A.4}$$

Pressure and temperature are psia, and $^{\circ}R$.

Step 3: Calculate compressibility factors of natural gas using Dranchuk and Abou-Kassem's equations (Dranchuk and Abou-Kassem, 1975).

$$\begin{aligned}
z = 1 + (A + \frac{A_2}{T_{pr}} + \frac{A_3}{T_{pr}^3} + \frac{A_4}{T_{pr}^4} + \frac{A_5}{T_{pr}^5})\rho_{pr} + (A_6 + \frac{A_7}{T_{pr}} + \frac{A_8}{T_{pr}^2})\rho_{pr}^2 \\
- A_9(\frac{A_7}{T_{pr}} + \frac{A_8}{T_{pr}^2})\rho_{pr}^5 + A_{10}(1 + A_{11}\rho_{pr}^2)(\frac{\rho_{pr}^2}{T_{pr}^3})\exp(-A_{11}\rho_{pr}^2)
\end{aligned} \tag{A.5}$$

where

$$\rho_{pr} = 0.27\left[\frac{p_{pr}}{zT_{pr}}\right]$$

The constants are $A_1 = 0.3265$, $A_2 = -1.0700$, $A_3 = -0.5339$, $A_4 = 0.05169$, $A_5 = -0.05165$, $A_6 = 0.5475$, $A_7 = -0.7361$, $A_8 = 0.1844$, $A_9 = 0.1056$, $A_{10} = 0.6134$, $A_{11} = 0.7210$.

The range of applicability is $0.2 \leq p_{pr} < 30$ for $1.0 < T_{pr} \leq 3.0$ and $p_{pr} < 1.0$ for $0.7 < T_{pr} < 1.0$

Step 4: Calculate gas density.

$$\rho = \frac{M\,p}{zRT} \tag{A.6}$$

where

$$M = 28.97\gamma_g^2$$

$$R = 10.732 \ \frac{psia. \cdot ft^3}{lbmol \cdot {}^{\circ}R}$$

130

Density is in $\dfrac{lb}{ft^3}$.   Pressure and temperature are $psia$, $^{\circ}R$.

A.1.2   Thermal expansion coefficient of gas

Once the gas density as a function of pressure and temperature is known, the thermal expansion coefficient of gas can be calculated from its definition.   The isobaric thermal coefficient of volume expansion for gas is defined as

$$\beta = -\frac{1}{\rho}\left(\frac{\partial \rho}{\partial T}\right)_p \tag{A.7}$$

or

$$\beta = \frac{1}{T} + \frac{1}{z}\left(\frac{\partial z}{\partial T}\right)_p \tag{A.8}$$

β is in $\dfrac{1}{^{\circ}R}$.   Temperature is in $^{\circ}R$.

A.1.3   Viscosity of gas

The equations presented by Lee *et al.* (1966) are the following,

$$\mu_g = A(10^{-4})\exp(B\rho^c) \tag{A.9}$$

where

$$A = \frac{(9.379 + 0.01607 M_a)T^{1.5}}{209.2 + 19.26 M_a + T},$$

$$B = 3.448 + \frac{986.4}{T} + 0.01009 M_a,$$

$$C = 2.447 - 0.2224 B.$$

$$M_a = 28.97\gamma_g$$

μ_g = gas viscosity in centipoises

$T =$ temperature in $^\circ R$. $\rho =$ gas density in $\dfrac{g}{cc}$.

A.1.4 Heat capacity of gas

Perry and Chilton (1973) presented the following equation for methane.

$$C_p = a + bT + \frac{c'}{T^2} \tag{A.10}$$

where C_p is in $\dfrac{kJ}{kgK}$, T is in K, and the coefficients $a = 1.39, b = 0.003001$, and $c' = 0$.

A.1.5 Total thermal conductivity of gas in reservoir ($K_{Tt,g}$)

The thermal conductivity of sandstone saturated with gas at reservoir temperature are from Anand *et al*. (1973). In the ranges of temperature between 150 $^\circ$F and 250 $^\circ$F, the value of $K_{Tt,g}$ is almost constant.

$$K_{Tt,g} = 1.3 \quad \frac{Btu}{lb \cdot ft \cdot ^\circ F} \tag{A.11}$$

A.2 OIL PROPERTIES

Crude oil properties are calculated by assuming that pressure, temperature, $^\circ API$, gas specific gravity and solution of gas (R_s) are known.

A.2.1 Bubble point pressure of oil

The following equations were presented by Standing (1977).

$$p_b = 18.2 \left[(CN)_{pb} - 1.4 \right] \tag{A.12}$$

132

where

$$(CN)_{pb} = \left(\frac{R_s}{\gamma_g}\right)^{0.83} 10^{(0.00091T - 0.0125\,API)}$$

T is reservoir temperature in $^\circ F$, R_S is solution gas-oil ratio in $\dfrac{scf}{STB}$, and p_b is bubble-point pressure in psia.

A.2.2 Density of oil

The following equations are need to obtain the density of the crude oil at reservoir condition (Standing, 1977; McCain, 1990).

$$\rho = \rho_{po} + \Delta\rho_p - \Delta\rho_T \tag{A.13}$$

$$\Delta\rho_p = (0.167 + 16.181(10^{-0.0425\upsilon_{po}})\left(\frac{p}{1000}\right) - 0.01(0.299 + 262(10^{-0.0603\rho_{po}})\left(\frac{p}{1000}\right)^2 \tag{A.14}$$

where p is pressure in psia, ρ_{po} is the pseudoliquid density, and $\Delta\rho_p$ is the adjustment for pressure in $\dfrac{lb}{ft^3}$

$$\Delta\rho_T = (0.00302 + 1.505\rho_{bs}^{-0.951})(T - 60)^{0.938} - \left(0.0216 - 0.0233\left(10^{-0.0161\rho_{bs}}\right)\right)(T - 60)^{0.475} \tag{A.15}$$

where T is temperature in $^\circ F$, ρ_{bs} is the liquid density at pressure and $60\,^\circ F$, $\Delta\rho_T$ is the adjustment for temperature in $\dfrac{lb}{ft^3}$.

$$\rho_{po} = \frac{\dfrac{R_s M_a}{380.7} + 350.207\gamma_o}{5.615 + \dfrac{R_s M_a}{380.7\rho_a}} \tag{A.16}$$

$$M_a = 28.97\gamma_g$$

$$\gamma_o = \frac{141.5}{131.5 + {}^\circ API}$$

$$\rho_a = 38.52(10^{-0.00326\,API}) + (94.75 - 33.93\log API)\log\gamma_g$$

where API is the gravity of the liquid in ${}^\circ API$ and ρ_a is the apparent liquid density of the gas in $\dfrac{lb}{ft^3}$ at $60\,{}^\circ F$ and atmospheric pressure.

A.2.3 Thermal expansion coefficient of oil

The isobaric thermal expansion of an undersaturated oil is defined as

$$\beta = -\frac{1}{\rho}\left(\frac{\partial\rho}{\partial T}\right)_p \tag{A.17}$$

or

$$\beta = \frac{1}{B_o}\left(\frac{\partial B_o}{\partial T}\right)_p \tag{A.18}$$

β is the thermal expansion coefficient in $\dfrac{1}{{}^\circ R}$. B_o is the oil formation volume factor. ρ is oil density. Since the density of an undersaturated liquid decreases as the temperature increases, β is positive.

A.2.4　Viscosity of oil

First calculate the dead oil viscosity from Ng and Egbogah (1983)'s equation. Then calculate viscosity of oil at bubble-point pressure from Beggs and Robinson (1975)'s equation.

$$\log[\log(\mu_{oD}+1)]=1.8653-0.025086API-0.5644\log(T) \tag{A.19}$$

where T is reservoir temperature in $^{\circ}F$, API is stock-tank oil gravity in $^{\circ}API$, and μ_{oD} is the dead oil viscosity in centipoises at atmospheric pressure and T.

$$\mu_{ob}=A\mu_{oD}^{B} \tag{A.20}$$

where

$$A=10.715(R_s+100)^{-0.515}$$
$$B=5.44(R_s+150)^{-0.338}$$

where R_s is the solution gas-oil ratio of the liquid at p and T, μ_{oD} is the dead oil viscosity in centipoises. μ_{ob} is the oil viscosity in centipoises at bubble-point pressure.

Finally, calculate the oil viscosity at reservoir condition

$$\mu_o=\mu_{ob}\left(\frac{p}{p_b}\right)^{B} \tag{A.21}$$

and

$$B=C_1 p^{C_2}\exp(C_3+C_4 p)$$

where $C_1 = 2.6$, $C_2 = 1.187$, $C_3 = -11.513$, $C_4 = -8.98 \times 10^{-5}$ and p is pressure above bubble-point pressure and p_b is bubble-point pressure in psia. μ_o is the oil viscosity at reservoir condition.

A.2.5 Heat capacity of oil

Gambill (1957) developed a relation for heat capacity of oil at reservoir temperature for T is less than about 300 $^\circ F$ as the following.

$$C_p = \frac{(0.388 + 0.00045T)}{\sqrt{\gamma_o}} \tag{A.22}$$

where C_p is the heat capacity of oil in $\frac{Btu}{lb\,^\circ F}$, T is reservoir temperature in $^\circ F$, and

$$\gamma_o = \frac{141.5}{131.5 + \,^\circ API}$$

A.2.6 Total thermal conductivity of oil in reservoir ($K_{Tt,o}$)

The thermal conductivity of sandstone saturated with oil at reservoir temperature are from Anand *et al.* (1973). In the ranges of temperature between 150 ^oF and 250 ^oF, the value of $K_{Tt,o}$ is almost constant.

$$K_{Tt,o} = 2.0 \ \frac{Btu}{lb \cdot ft \cdot \,^\circ F} \tag{A.23}$$

A.3 WATER PROPERTIES

Water properties are calculated by assuming that pressure, temperature and salinity are known.

A.3.1 Density of water

The density of water at reservoir condition are estimated using correlation presented by McCain (1990).   First calculate water density at standard condition.

$$\rho_{WSTD} = 62.368 + 0.438603S + 1.60074\left(10^{-3}\right)S^2 \tag{A.24}$$

where S is the salinity in weight percent solids, ρ_{WSTD} is the water density at standard condition in $\dfrac{lb}{ft^3}$.

Then, calculate the water formation volume factor.

$$B_W = \left(1 + \Delta V_{WP}\right)\left(1 + \Delta V_{WT}\right) \tag{A.25}$$

and

$$\Delta V_{WT} = -1.0001(10^{-2}) + 1.33391\left(10^{-4}\right)T + 5.50654\left(10^{-7}\right)T^2$$

$$\Delta V_{Wp} = -1.95301(10^{-9}) - 1.72834\left(10^{-13}\right)p^2 T - 3.58922\left(10^{-7}\right)p - 2.25341\left(10^{-10}\right)p^2$$

where

T is in $^\circ F$, p in psia and B_W is in $\dfrac{reservoir\ bbl}{STB}$.

Finally, calculate water density at reservoir condition.

$$\rho_W = \frac{\rho_{WSTD}}{B_W} \tag{A.26}$$

where ρ_W is water density in $\dfrac{lb}{ft^3}$.

A.3.2 Thermal expansion coefficient of water

The isobaric thermal expansion of water is defined as

$$\beta = -\frac{1}{\rho}\left(\frac{\partial \rho}{\partial T}\right)_p \tag{A.27}$$

or

$$\beta = \frac{1}{B_W}\left(\frac{\partial B_W}{\partial T}\right)_p \tag{A.28}$$

β is thermal expansion coefficient in $\frac{1}{^{\circ}R}$. B_W is water formation volume factor. ρ_W is water density. Since the density of water decreases as the temperature increases, β is positive.

A.3.3 Viscosity of water

Water viscosity correlation was developed from data that have a temperature range of 86.5 to 167 $^{\circ}$F and pressures up to 14,000 psi (Collins, 1987). First calculate water viscosity at atmospheric pressure. Then calculate the ratio of viscosity at reservoir condition.

$$\mu_{WSTD} = AT^B \tag{A.29}$$

$$Ratio = 0.9994 + 4.0295(10^{-5})p + 3.1062(10^{-9})p^2 \tag{A.30}$$

$$\mu_W = \mu_{WSTD}\ Ratio \tag{A.31}$$

where T is in $^{\circ}F$, μ_{WSTD} and μ_W are in centipoises.

$$A = A_o + A_1 S + A_2 S^2 + A_3 S^3$$

$$B = B_o + B_1 S + B_2 S^2 + B_3 S^3 + B_4 S^4$$

138

where $A_o = 109.574$, $A_1 = -8.40564$, $A_2 = 0.313314$, $A_3 = 8.72213 \times 10^{-3}$,

$B_o = -1.12166$, $B_1 = 2.63951 \times 10^{-2}$, $B_2 = -6.79461 \times 10^{-4}$, $B_3 = -5.47119 \times 10^{-5}$,

$B_4 = 1.55586 \times 10^{-6}$ and S is salinity in weight percent solids.

A.3.4   Heat capacity of water

The heat capacity of liquid water at saturation condition can be represented by the following equation (Cassis, 1985).

$$c_p = 4.182 - 1.5 \times 10^{-4} T + 3.44 \times 10^{-7} T^2 + 4.26 \times 10^{-8} T^3 \tag{A.32}$$

where c_p is in $\dfrac{kJ}{kg\,^\circ C}$ and T is in $^\circ C$.

A.3.5   Total thermal conductivity of water in reservoir ($K_{Tt,w}$)

The thermal conductivity of sandtone saturated with water at reservoir temperature are from Anand *et al*. (1973).   In the ranges of temperature between 150 and 250 ^{o}F, the value of $K_{Tt,w}$ is almost constant.

$$K_{Tt,w} = 2.5 \quad \frac{Btu}{lb \cdot ft \cdot ^\circ F} \tag{A.33}$$

APPENDIX B

Derivatives and Limits of Terms

This appendix provides a detail of derivatives and limits of terms mentioned in Chapter 3, Section 3.3.1.2. The parameters and terms are defined as

$$a = m_1 e^{m_1 h/2 + m_2 Y/2} - m_2 e^{m_1 Y/2 + m_2 h/2}$$

$$b = (T_o - \frac{1}{\beta})m_2 e^{m_2 h/2}$$

$$c = (T_o - \frac{1}{\beta})m_1 e^{m_1 h/2}$$

$$d = m_r(\frac{2}{h})e^{m_2 Y/2 + m_1 h/2}$$

$$g = m_r(\frac{2}{h})e^{m_1 Y/2 + m_2 h/2}$$

$$T_e = \frac{1}{\beta} + \frac{-be^{m_1 h/2} + ce^{m_2 h/2}}{a - d + g}$$

$$m_1 = \alpha q$$

$$m_2 = \sigma q$$

$$m_r = \delta q$$

$$\alpha = \frac{1}{4hL}\left[\frac{\rho C_p}{K_{Tt}} + \sqrt{\left(\frac{\rho C_p}{K_{Tt}}\right)^2 + \frac{4\beta\mu}{kK_{Tt}}}\right]$$

$$\sigma = \frac{1}{4hL}\left[\frac{\rho C_p}{K_{Tt}} - \sqrt{\left(\frac{\rho C_p}{K_{Tt}}\right)^2 + \frac{4\beta\mu}{kK_{Tt}}}\right]$$

$$\delta = \frac{1}{4\pi L}\left[\frac{\rho C_p}{K_{Tt}} - \sqrt{\left(\frac{\rho C_p}{K_{Tt}}\right)^2 + \frac{4\mu\beta}{kK_{Tt}}}\right]$$

The following terms are required to substitute into equation (3.41) when applying L'Hopital's rule.

1) Limit of $\dfrac{d}{dq}\left(-b\,e^{m_1 h/2}\right)$

$$\frac{d}{dq}\left(-b\,e^{m_1 h/2}\right) = -\left(b(h/2)\alpha e^{m_1 h/2} + (T_0 - 1/\beta)\,e^{m_1 h/2}\left[m_2(h/2)\sigma e^{m_2 h/2} + \sigma e^{m_2 h/2}\right]\right)$$

$$\lim_{q\to 0}\left(\frac{d}{dq}\left(-b\,e^{m_1 h/2}\right)\right) = -(T_0 - 1/\beta)\sigma$$

2) Limit of $\dfrac{d}{dq}\left(c\,e^{m_2 h/2}\right)$

$$\frac{d}{dq}\left(c\,e^{m_2 h/2}\right) = \left(\sigma m_1(h/2)\,(T_0 - 1/\beta)\,e^{m_1 h/2 + m_2 h/2} + (T_0 - 1/\beta)e^{m_2 h/2}\left[m_1\frac{de^{m_1 h/2}}{dq} + e^{m_1 h/2}\frac{dm_1}{dq}\right]\right)$$

$$\lim_{q\to 0}\left(\frac{d}{dq}\left(c\,e^{m_2 h/2}\right)\right) = (T_0 - 1/\beta)\alpha$$

3) Limit of $\dfrac{d}{dq}(a)$

$$\frac{d}{dq}(a) = \frac{d}{dq}\left(m_1 e^{m_1 h/2 + m_2 Y/2} - m_2 e^{m_1 Y/2 + m_2 h/2}\right)$$

$$\frac{d}{dq}(a) = \left(m_1 e^{m_1 h/2 + m_2 Y/2}(h\alpha/2 + Y\sigma/2) + \alpha e^{m_1 h/2 + m_2 Y/2} - q\sigma e^{m_1 Y/2 + m_2 h/2}(Y\alpha/2 + h\sigma/2) - e^{m_1 Y/2 + m_2 h/2}\right)$$

$$\lim_{q\to 0}\left(\frac{d}{dq}(a)\right) = \left(\alpha e^{m_1 h/2 + m_2 Y/2} - \sigma e^{m_1 Y/2 + m_2 h/2}\right) = \alpha - \delta$$

4) Limit of $\dfrac{d}{dq}(d)$

$$\frac{d}{dq}(d) = \left(m_r(2/h)(Y\sigma/2 + h\alpha/2)e^{m_1h/2+m_2Y/2} + (2/h)\delta\, e^{m_2Y/2+m_1h/2}\right)$$

$$\lim_{q\to 0}\left(\frac{d}{dq}(d)\right) = (2/h)\delta$$

5)   Limit of $\dfrac{d}{dq}(e)$

$$\frac{d}{dq}(e) = \left(m_r(2/h)(Y\alpha/2 + h\sigma/2)\,e^{m_1Y/2+m_2h/2} - (2/h)e^{m_1Y/2+m_2h/2}\right)$$

$$\lim_{q\to 0}\left(\frac{d}{dq}(e)\right) = (2/h)\delta$$

APPENDIX C

Finite-Difference Formulation of Mass Balance

For three-dimension flow in a Cartesian coordinate system, the mass balance over a box-shaped control volume ($\Delta x \Delta y \Delta z$) can be written as below.

$$
-\frac{\Delta y \Delta z}{\rho_o} \Delta_x (\rho_o u_o) - \frac{\Delta x \Delta z}{\rho_o} \Delta_y (\rho_o u_o) - \frac{\Delta x \Delta y}{\rho_o} \Delta_z (\rho_o u_o)
$$
$$
-\frac{\Delta y \Delta z}{\rho_w} \Delta_x (\rho_w u_w) - \frac{\Delta x \Delta z}{\rho_w} \Delta_y (\rho_w u_w) - \frac{\Delta x \Delta y}{\rho_w} \Delta_z (\rho_w u_w) \tag{4.6}
$$
$$
= \phi S_o c_o \left(\frac{\Delta x \Delta y \Delta z}{\Delta t} \right) \Delta_t p_o + \phi S_w c_w \left(\frac{\Delta x \Delta y \Delta z}{\Delta t} \right) \Delta_t p_w
$$

An example shows how the finite differences were done. Here we show the finite difference of the third term on the left side.

$$
-\frac{\Delta x \Delta y}{\rho_o} \Delta_z (\rho_o u_o) = -\frac{\Delta x \Delta y}{\rho_o} \left[(\rho_o u_o)_{k+1/2} - (\rho_o u_o)_{k-1/2} \right]
$$

Substitute Darcy velocity

$$
-\frac{\Delta x \Delta y}{\rho_o} \Delta_z (\rho_o u_o) = -\left(\frac{\Delta x \Delta y}{\rho_o} \right)_k \left[\begin{array}{l} \left(-\rho_o \frac{kk_{ro}}{\mu_o} \left\langle \frac{\Delta p_o}{\Delta z} - \rho_o g \frac{\Delta D}{\Delta z} \right\rangle \right)_{k+1/2} \\ -\left(-\rho_o \frac{kk_{ro}}{\mu_o} \left\langle \frac{\Delta p_o}{\Delta z} - \rho_o g \frac{\Delta D}{\Delta z} \right\rangle \right)_{k-1/2} \end{array} \right]
$$

Note that if the spatial indicators (i, j, k) are left out, the defaults are either i, j, or k.

Now, expand Darcy velocity

$$-\frac{\Delta x \Delta y}{\rho_o} \Delta_z (\rho_o u_o) = -\left(\frac{\Delta x \Delta y}{\rho_o}\right)_k \begin{bmatrix} \left(-\rho_o \frac{kk_{ro}}{\mu_o}\right)_{k+1/2} \left(\frac{p_{o,k+1}^{n+1} - p_{o,k}^{n+1}}{\Delta z} - \rho_o g \frac{D_{k+1} - D_k}{\Delta z}\right) \\ -\left(-\rho_o \frac{kk_{ro}}{\mu_o}\right)_{k-1/2} \left(\frac{p_{o,k}^{n+1} p_{ok} - p_{o,k-1}^{n+1}}{\Delta z} - \rho_o g \frac{D_k - D_{k-1}}{\Delta z}\right) \end{bmatrix}$$

Apply upstream weighting and rearrange the terms

$$-\frac{\Delta x \Delta y}{\rho_o} \Delta_z (\rho_o u_o) = \begin{bmatrix} p_{ok+1}^{n+1} \left(\frac{\Delta x \Delta y}{\rho_o \Delta z}\right)_k \left(\frac{\rho_o kk_{ro}}{\mu_o}\right)_k + p_{ok-1}^{n+1} \left(\frac{\Delta x \Delta y}{\rho_o \Delta z}\right)_k \left(\frac{\rho_o kk_{ro}}{\mu_o}\right)_{k-1} \\ + p_{ok}^{n+1} \left\langle -\left(\frac{\Delta x \Delta y}{\rho_o \Delta z}\right)_k \left(\frac{\rho_o kk_{ro}}{\mu_o}\right)_k - \left(\frac{\Delta x \Delta y}{\rho_o \Delta z}\right)_k \left(\frac{\rho_o kk_{ro}}{\mu_o}\right)_{k-1} \right\rangle \\ -(\rho_o g)_k (D_{k+1} - D_k) \left(\frac{\Delta x \Delta y}{\rho_o \Delta z}\right)_k \left(\frac{\rho_o kk_{ro}}{\mu_o}\right)_k \\ +(\rho_o g)_{k-1} (D_k - D_{k-1}) \left(\frac{\Delta x \Delta y}{\rho_o \Delta z}\right)_k \left(\frac{\rho_o kk_{ro}}{\mu_o}\right)_{k-1} \end{bmatrix}$$

The finite-difference form of the equation (4.6) is

$$A_{ijk} p_{wi+1,jk}^{n+1} + B_{ijk} p_{wi-1,jk}^{n+1} + C_{ijk} p_{wi,j+1,k}^{n+1} + D_{ijk} p_{wi,j-1,k}^{n+1} + E_{ijk} p_{wi+1,j,k}^{n+1} + F_{ijk} p_{wi-1,jk}^{n+1}$$
$$+ G_{ijk} p_{wijk}^{n+1} = RHS_{ijk}$$

where

$$A_{ijk} = \left[\left(\frac{\Delta y \Delta z}{\rho_w \Delta x}\right)_i \left(\frac{\rho_w kk_{rw}}{\mu_w}\right)_i + \left(\frac{\Delta y \Delta z}{\rho_o \Delta x}\right)_i \left(\frac{\rho_o kk_{ro}}{\mu_o}\right)_i\right]$$

$$B_{ijk} = \left[\left(\frac{\Delta y \Delta z}{\rho_w \Delta x} \right)_i \left(\frac{\rho_w k k_{rw}}{\mu_w} \right)_{i-1} + \left(\frac{\Delta y \Delta z}{\rho_o \Delta x} \right)_i \left(\frac{\rho_o k k_{ro}}{\mu_o} \right)_{i-1} \right]$$

$$C_{ijk} = \left[\left(\frac{\Delta x \Delta z}{\rho_w \Delta y} \right)_j \left(\frac{\rho_w k k_{rw}}{\mu_w} \right)_j + \left(\frac{\Delta x \Delta z}{\rho_o \Delta y} \right)_j \left(\frac{\rho_o k k_{ro}}{\mu_o} \right)_j \right]$$

$$D_{ijk} = \left[\left(\frac{\Delta x \Delta z}{\rho_w \Delta y} \right)_j \left(\frac{\rho_w k k_{rw}}{\mu_w} \right)_{j-1} + \left(\frac{\Delta x \Delta z}{\rho_o \Delta y} \right)_j \left(\frac{\rho_o k k_{ro}}{\mu_o} \right)_{j-1} \right]$$

$$E_{ijk} = \left[\left(\frac{\Delta x \Delta y}{\rho_w \Delta z} \right)_k \left(\frac{\rho_w k k_{rw}}{\mu_w} \right)_k + \left(\frac{\Delta x \Delta y}{\rho_o \Delta z} \right)_k \left(\frac{\rho_o k k_{ro}}{\mu_o} \right)_k \right]$$

$$F_{ijk} = \left[\left(\frac{\Delta x \Delta y}{\rho_w \Delta z} \right)_k \left(\frac{\rho_w k k_{rw}}{\mu_w} \right)_{k-1} + \left(\frac{\Delta x \Delta y}{\rho_o \Delta z} \right)_k \left(\frac{\rho_o k k_{ro}}{\mu_o} \right)_{k-1} \right]$$

$$G_{ijk} = \left[-A_{ijk} - B_{ijk} - C_{ijk} - D_{ijk} - E_{ijk} - F_{ijk} - \left(\frac{\phi S_w c_w \Delta x \Delta y \Delta z}{\Delta t} \right)^n_{ijk} - \left(\frac{\phi (1 - S_w) c_o \Delta x \Delta y \Delta z}{\Delta t} \right)^n_{ijk} \right]$$

$$
RHS_{ijk} = \begin{bmatrix}
- p_{wijk}^{n}\left(\dfrac{\phi\, S_w c_w \Delta x \Delta y \Delta z}{\Delta t}\right)^{n}_{ijk} - p_{wijk}^{n}\left(\dfrac{\phi (1 - S_w) c_o \Delta x \Delta y \Delta z}{\Delta t}\right)^{n}_{ijk} \\[2ex]
+ \left(\rho_w g\right)_k \left(D_{k+1} - D_k\right) E_{ijk}^{w} - \left(\rho_w g\right)_{k-1}\left(D_k - D_{k-1}\right) F_{ijk}^{w} \\[2ex]
+ \left(\rho_o g\right)_k \left(D_{k+1} - D_k\right) E_{ijk}^{o} - \left(\rho_o g\right)_{k-1}\left(D_k - D_{k-1}\right) F_{ijk}^{o} \\[2ex]
- p_{c\,i+1}\left(\dfrac{\Delta y \Delta z}{\rho_o \Delta x}\right)_i \left(\dfrac{\rho_o k k_{ro}}{\mu_o}\right)_i - p_{c\,i-1}\left(\dfrac{\Delta y \Delta z}{\rho_o \Delta x}\right)_i \left(\dfrac{\rho_o k k_{ro}}{\mu_o}\right)_{i-1} \\[2ex]
- p_{c\,i}\left[-\left(\dfrac{\Delta y \Delta z}{\rho_o \Delta x}\right)_i \left(\dfrac{\rho_o k k_{ro}}{\mu_o}\right)_i - \left(\dfrac{\Delta y \Delta z}{\rho_o \Delta x}\right)_i \left(\dfrac{\rho_o k k_{ro}}{\mu_o}\right)_{i-1}\right] \\[2ex]
- p_{c\,j+1}\left(\dfrac{\Delta x \Delta z}{\rho_o \Delta y}\right)_j \left(\dfrac{\rho_o k k_{ro}}{\mu_o}\right)_j - p_{c\,j-1}\left(\dfrac{\Delta x \Delta z}{\rho_o \Delta y}\right)_j \left(\dfrac{\rho_o k k_{ro}}{\mu_o}\right)_{j-1} \\[2ex]
- p_{c\,j}\left[-\left(\dfrac{\Delta x \Delta z}{\rho_o \Delta y}\right)_j \left(\dfrac{\rho_o k k_{ro}}{\mu_o}\right)_j - \left(\dfrac{\Delta x \Delta z}{\rho_o \Delta y}\right)_j \left(\dfrac{\rho_o k k_{ro}}{\mu_o}\right)_{j-1}\right] \\[2ex]
- p_{c\,k+1}\left(\dfrac{\Delta x \Delta y}{\rho_o \Delta z}\right)_k \left(\dfrac{\rho_o k k_{ro}}{\mu_o}\right)_k - p_{c\,k-1}\left(\dfrac{\Delta x \Delta y}{\rho_o \Delta z}\right)_k \left(\dfrac{\rho_o k k_{ro}}{\mu_o}\right)_{k-1} \\[2ex]
- p_{c\,k}\left[-\left(\dfrac{\Delta x \Delta y}{\rho_o \Delta z}\right)_k \left(\dfrac{\rho_o k k_{ro}}{\mu_o}\right)_k - \left(\dfrac{\Delta x \Delta y}{\rho_o \Delta z}\right)_k \left(\dfrac{\rho_o k k_{ro}}{\mu_o}\right)_{k-1}\right]
\end{bmatrix}
$$

APPENDIX D

Finite-Difference Formulation of Energy Balance

The energy balance from equation (4.21) is

$$
(\rho_o \vec{u}_o C_{po} + \rho_w \vec{u}_w C_{pw})\bar{\nabla}T - (\beta_o \vec{u}_o \cdot \bar{\nabla}p_o + \beta_w \vec{u}_w \cdot \bar{\nabla}p_w)T - \bar{\nabla} \cdot (K_{Tt} \cdot \bar{\nabla}T) + \vec{u}_o \cdot \bar{\nabla}p_o
$$

$$
+ \vec{u}_w \cdot \bar{\nabla}p_w + \bar{\nabla} \cdot (\rho_o \vec{u}_o gD + \rho_w \vec{u}_w gD) = -[(1-\phi)\rho_s C_{ps} + \phi(S_o \rho_o C_{po} + S_w \rho_w C_{pw})]\frac{\partial T}{\partial t}
$$

$$
+ T\left(S_o \beta_o \phi_o \frac{\partial p_o}{\partial t} + S_w \beta_w \phi \frac{\partial p_w}{\partial t}\right) - \frac{\partial}{\partial t}(S_o \rho_o gD + S_w \rho_w gD)
$$

An example shows how the finite differences were done over a box-shaped control volume ($\Delta x \Delta y \Delta z$). Here we show the finite difference of the first term on the left side. Note that if the spatial indicators (i, j, k) are left out, the defaults are either i, j, or k.

$$
(\rho_o \vec{u}_o C_{po} + \rho_w \vec{u}_w C_{pw})(\Delta x \Delta y \Delta z)\bar{\nabla}T =
\begin{bmatrix}
(\rho_o \vec{u}_o C_{po} + \rho_w \vec{u}_w C_{pw})_i (\Delta y \Delta z)(T_{i+1}^{n+1} - T_i^{n+1}) \\
+ (\rho_o \vec{u}_o C_{po} + \rho_w \vec{u}_w C_{pw})_j (\Delta x \Delta z)(T_{j+1}^{n+1} - T_j^{n+1}) \\
+ (\rho_o \vec{u}_o C_{po} + \rho_w \vec{u}_w C_{pw})_k (\Delta x \Delta y)(T_{k+1}^{n+1} - T_k^{n+1})
\end{bmatrix}
$$

Rearrange the terms.

$$
(\rho_o \vec{u}_o C_{po} + \rho_w \vec{u}_w C_{pw})(\Delta x \Delta y \Delta z)\bar{\nabla}T =
\begin{bmatrix}
\Delta y \Delta z \, P1_{ijk} \, T_{i+1}^{n+1} - \Delta y \Delta z \, P1_{ijk} \, T_i^{n+1} \\
+ \Delta x \Delta z \, P2_{ijk} \, T_{j+1}^{n+1} - \Delta x \Delta z \, P2_{ijk} \, T_j^{n+1} \\
+ \Delta x \Delta y \, P3_{ijk} \, T_{k+1}^{n+1} - \Delta x \Delta y \, P3_{ijk} \, T_k^{n+1}
\end{bmatrix}
$$

The finite-difference form of the equation (4.21) is

$$A_{ijk}\, p^{n+1}_{wi+1,jk} + B_{ijk}\, p^{n+1}_{wi-1,jk} + C_{ijk}\, p^{n+1}_{wi,j+1,k} + D_{ijk}\, p^{n+1}_{wi,j-1,k} + E_{ijk}\, p^{n+1}_{wi+1,j,k} + F_{ijk}\, p^{n+1}_{wi-1,jk}$$
$$+ G_{ijk}\, p^{n+1}_{wijk} = RHS_{ijk}$$

where

$$A_{ijk} = -\Delta y \Delta z\, P1_{ijk} + \left(\frac{\Delta y \Delta z}{\Delta x}\right) K_{Tt,x}$$

$$B_{ijk} = \left(\frac{\Delta y \Delta z}{\Delta x}\right) K_{Tt,x}$$

$$C_{ijk} = -\Delta x \Delta z\, P2_{ijk} + \left(\frac{\Delta x \Delta z}{\Delta y}\right) K_{Tt,y}$$

$$D_{ijk} = \left(\frac{\Delta x \Delta z}{\Delta y}\right) K_{Tt,y}$$

$$E_{ijk} = -\Delta x \Delta y\, P3_{ijk} + \left(\frac{\Delta x \Delta y}{\Delta z}\right) K_{Tt,z}$$

$$F_{ijk} = \left(\frac{\Delta x \Delta y}{\Delta z}\right) K_{Tt,z}$$

$$G_{ijk} = \begin{bmatrix} \Delta y \Delta z\, P1_{ijk} + \Delta x \Delta z\, P2_{ijk} + \Delta x \Delta y\, P3_{ijk} + \Delta x \Delta y \Delta z\, P4_{ijk} - 2\left(\frac{\Delta y \Delta z}{\Delta x}\right) K_{Tt,x} \\ -2\left(\frac{\Delta x \Delta z}{\Delta y}\right) K_{Tt,y} - 2\left(\frac{\Delta x \Delta y}{\Delta z}\right) K_{Tt,z} + P7_{ijk} + P8_{ijk} \end{bmatrix}$$

148

$$RHS_{ijk} = \Delta x \Delta y \Delta z \, P5_{ijk} + \Delta x \Delta y \Delta z \, P6_{ijk} + P7_{ijk} \, T_{ijk}^{n} - P9_{ijk}$$

and

$$P1_{ijk} = \left[\rho_{o,i} \left(\frac{-kk_{ro}}{\mu_o} \right)_i \left(\frac{p_{o,i+1}^{n+1} - p_{o,i}^{n+1}}{\Delta x} \right) C_{po,i} + \rho_{w,i} \left(\frac{-kk_{rw}}{\mu_w} \right)_i \left(\frac{p_{w,i+1}^{n+1} - p_{w,i}^{n+1}}{\Delta x} \right) C_{pw,i} \right]$$

$$P2_{ijk} = \left[\rho_{o,j} \left(\frac{-kk_{ro}}{\mu_o} \right)_j \left(\frac{p_{o,j+1}^{n+1} - p_{o,j}^{n+1}}{\Delta y} \right) C_{po,j} + \rho_{w,j} \left(\frac{-kk_{rw}}{\mu_w} \right)_j \left(\frac{p_{w,j+1}^{n+1} - p_{w,j}^{n+1}}{\Delta y} \right) C_{pw,j} \right]$$

$$P3_{ijk} = \left[\begin{array}{l} \rho_{o,k} \left(\frac{-kk_{ro}}{\mu_o} \right)_k \left(\frac{p_{o,k+1}^{n+1} - p_{o,k}^{n+1}}{\Delta z} - \rho_{o,k} g \frac{D_{k+1} - D_k}{\Delta z} \right) C_{po,k} \\[4mm] + \rho_{w,k} \left(\frac{-kk_{rw}}{\mu_w} \right)_k \left(\frac{p_{w,k+1}^{n+1} - p_{w,k}^{n+1}}{\Delta z} - \rho_{w,k} g \frac{D_{k+1} - D_k}{\Delta z} \right) C_{pw,k} \end{array} \right]$$

$$P4_{ijk} = - \left[\begin{array}{l} \beta_{o,i} \left(-\frac{kk_{ro}}{\mu_o} \right)_i \left(\frac{p_{o,i+1} - p_{o,i}}{\Delta x} \right) \left(\frac{p_{o,i+1} - p_{o,i}}{\Delta x} \right) \\[4mm] + \beta_{o,j} \left(-\frac{kk_{ro}}{\mu_o} \right)_j \left(\frac{p_{o,j+1} - p_{o,j}}{\Delta y} \right) \left(\frac{p_{o,j+1} - p_{o,j}}{\Delta y} \right) \\[4mm] + \beta_{o,k} \left(-\frac{kk_{ro}}{\mu_o} \right)_k \left(\frac{p_{o,k+1} - p_{o,k}}{\Delta z} - \rho_o g \frac{D_{k+1} - D_k}{\Delta z} \right) \left(\frac{p_{o,k+1} - p_k}{\Delta z} \right) \\[4mm] \beta_{w,i} \left(-\frac{kk_{rw}}{\mu_w} \right)_i \left(\frac{p_{w,i+1} - p_{w,i}}{\Delta x} \right) \left(\frac{p_{w,i+1} - p_{w,i}}{\Delta x} \right) \\[4mm] + \beta_{w,j} \left(-\frac{kk_{rw}}{\mu_w} \right)_j \left(\frac{p_{w,j+1} - p_{w,j}}{\Delta y} \right) \left(\frac{p_{w,j+1} - p_{w,j}}{\Delta y} \right) \\[4mm] + \beta_{w,k} \left(-\frac{kk_{rw}}{\mu_w} \right)_k \left(\frac{p_{w,k+1} - p_{w,k}}{\Delta z} - \rho_w g \frac{D_{k+1} - D_k}{\Delta z} \right) \left(\frac{p_{w,k+1} - p_k}{\Delta z} \right) \end{array} \right]$$

149

$$
P5_{ijk} = \begin{bmatrix} \left(\dfrac{-k_x k_{ro}}{\mu_o}\right)_i \left(\dfrac{p_{o,i+1} - p_{o,i}}{\Delta x}\right)^2 + \left(\dfrac{-k_x k_{rw}}{\mu_w}\right)_i \left(\dfrac{p_{w,i+1} - p_{w,i}}{\Delta x}\right)^2 \\[2mm] + \left(\dfrac{-k_y k_{ro}}{\mu_o}\right)_j \left(\dfrac{p_{o,j+1} - p_{o,j}}{\Delta y}\right)^2 + \left(\dfrac{-k_y k_{rw}}{\mu_w}\right)_j \left(\dfrac{p_{w,j+1} - p_{w,j}}{\Delta y}\right)^2 \\[2mm] + \left(\dfrac{-k_z k_{ro}}{\mu_o}\right)_k \left(\dfrac{p_{o,k+1} - p_{o,k}}{\Delta z} - \rho_{o,k} g \dfrac{D_{k+1} - D_k}{\Delta z}\right)^2 \\[2mm] + \left(\dfrac{-k_z k_{rw}}{\mu_w}\right)_k \left(\dfrac{p_{w,k+1} - p_{w,k}}{\Delta z} - \rho_{w,k} g \dfrac{D_{k+1} - D_k}{\Delta z}\right)^2 \end{bmatrix}
$$

$$
P6_{ijk} = \begin{bmatrix} \rho_{o,i}\left(\dfrac{-kk_{ro}}{\mu_o}\right)_i \left(\dfrac{p_{o,i+1} - p_{o,i}}{\Delta x}\right)\dfrac{gD_i}{\Delta x} + \rho_{w,i}\left(\dfrac{-kk_{rw}}{\mu_w}\right)_i \left(\dfrac{p_{w,i+1} - p_{w,i}}{\Delta x}\right)\dfrac{gD_i}{\Delta x} \\[2mm] - \left\langle \rho_{o,i-1}\left(\dfrac{-kk_{ro}}{\mu_o}\right)_{i-1} \left(\dfrac{p_{o,i} - p_{o,i-1}}{\Delta x}\right)\dfrac{gD_{i-1}}{\Delta x} + \rho_{w,i-1}\left(\dfrac{-kk_{rw}}{\mu_w}\right)_{i-1} \left(\dfrac{p_{w,i} - p_{w,i-1}}{\Delta x}\right)\dfrac{gD_{i-1}}{\Delta x} \right\rangle \\[2mm] + \rho_{o,j}\left(\dfrac{-kk_{ro}}{\mu_o}\right)_j \left(\dfrac{p_{o,j+1} - p_{o,j}}{\Delta y}\right)\dfrac{gD_j}{\Delta y} + \rho_{w,j}\left(\dfrac{-kk_{rw}}{\mu_w}\right)_j \left(\dfrac{p_{w,j+1} - p_{w,j}}{\Delta y}\right)\dfrac{gD_j}{\Delta y} \\[2mm] - \left\langle \rho_{o,j-1}\left(\dfrac{-kk_{ro}}{\mu_o}\right)_{j-1} \left(\dfrac{p_{o,j} - p_{o,j-1}}{\Delta y}\right)\dfrac{gD_{j-1}}{\Delta y} + \rho_{w,j-1}\left(\dfrac{-kk_{rw}}{\mu_w}\right)_{j-1} \left(\dfrac{p_{w,j} - p_{w,j-1}}{\Delta y}\right)\dfrac{gD_{j-1}}{\Delta y} \right\rangle \\[2mm] + \rho_{o,k}\left(\dfrac{-kk_{ro}}{\mu_o}\right)_k \left(\dfrac{p_{o,k+1} - p_{o,k}}{\Delta z} - \rho_{o,k} g \dfrac{D_{k+1} - D_k}{\Delta z}\right)\dfrac{gD_k}{\Delta z} \\[2mm] + \rho_{w,k}\left(\dfrac{-kk_{rw}}{\mu_w}\right)_k \left(\dfrac{p_{w,k+1} - p_{w,k}}{\Delta z} - \rho_{w,k} g \dfrac{D_{k+1} - D_k}{\Delta z}\right)\dfrac{gD_k}{\Delta z} \\[2mm] - \left\langle \begin{array}{l} \rho_{o,k-1}\left(\dfrac{-kk_{ro}}{\mu_o}\right)_{k-1} \left(\dfrac{p_{o,k} - p_{o,k-1}}{\Delta z} - \rho_{o,k-1} g \dfrac{D_k - D_{k-1}}{\Delta z}\right)\dfrac{gD_{k-1}}{\Delta z} \\[2mm] + \rho_{w,k-1}\left(\dfrac{-kk_{rw}}{\mu_w}\right)_{k-1} \left(\dfrac{p_{w,k} - p_{w,k-1}}{\Delta z} - \rho_{w,k-1} g \dfrac{D_k - D_{k-1}}{\Delta z}\right)\dfrac{gD_{k-1}}{\Delta z} \end{array} \right\rangle \end{bmatrix}
$$

150

$$P7_{ijk} = -\Delta x \Delta y \left[(1-\phi) \rho_s C_{p,s} + S_o \rho_o C_{p,o} + S_w \rho_w C_{p,w} \right]_{ijk}^n$$

$$P8_{ijk} = \Delta x \Delta y \Delta z \left[\left(\frac{S_o \beta_o \phi}{\Delta t} \right)_{ijk}^n \left(p_{w,ijk}^{n+1} + p_{c,ijk}^{n+1} - p_{w,ijk}^n - p_{c,ijk}^n \right) + \left(\frac{S_w \beta_w \phi}{\Delta t} \right)_{ijk}^n \left(p_{w,ijk}^{n+1} - p_{w,ijk}^n \right) \right]$$

$$P9_{ijk} = -\frac{\Delta x \Delta y \Delta z}{\Delta t} \left[\left(S_o \rho_o gD + S_w \rho_w gD \right)_{ijk}^{n+1} - \left(S_o \rho_o gD + S_w \rho_w gD \right)_{ijk}^n \right]$$

APPENDIX E

Dimensionless Form of Pressure and Temperature for Reservoir Flow

This study has shown several specific examples that depend on a particular types of fluid and dimensions of flow geometry. To generalize the pressure and temperature solutions to be independent of dimensions and a particular fluid, we have developed the solutions in terms of dimensionless groups. A grouping technique used here is based on the Inspectional Analysis presented by Shook *et al*. (1992). We have reduced the physical constants and variables in the energy balance from 7 (q, ρ, C_p, β, K_{Tt}, μ, k) to 3 (G_{1D}, G_{2D}, G_{3D}) dimensionless groups.

Consider a two-dimensional flow shown in Figure E.1. The horizontal well is in the center of an isotropic reservoir and being considered as a source/sink. The top and bottom of the reservoir are impermeable.
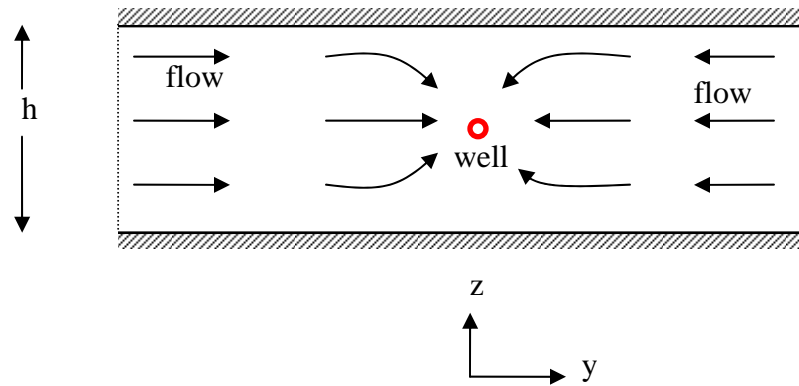

Figure E.1   Schematic of flow direction in the y-z plane with no-flow boundaries.

152

E.1 MASS BALANCE

For a single-phase and steady-state flow with no gravity, the governing equation is

$$\frac{\partial^2 p_D}{\partial y_D^2} + \frac{\partial^2 p_D}{\partial z_D^2} = 0 \tag{E.1}$$

Two boundary conditions are required to solve this second-order differential equation. The proper boundary conditions are

$$p_D(r_{wD}) = 1 \tag{E.2}$$

$$\left(\frac{\partial p_D}{\partial r_D}\right)_{r_{wD}} = \frac{q_D}{2\pi r_{wD}} \tag{E.3}$$

The dimensionless groups are defined as the followings.

$$q_D = \frac{q\mu}{kLp_{well}} \tag{E.4}$$

$$p_D = \frac{p}{p_{well}} \tag{E.5}$$

$$y_D = \frac{y}{h} \tag{E.6}$$

153

$$z_D = \frac{z}{h} \tag{E.7}$$

$$r_{wD} = \frac{r_w}{h} \tag{E.8}$$

The conformal mapping solution from Chapter 2, equation (2.8), can be rewritten in dimensionless parameters as

$$p_D(y_D, z_D) = \frac{q_D}{2\pi} \ln\left[\cosh(2\pi y_D) - \cos(2\pi z_D)\right] \tag{E.9}$$

The radial-linear composite solution from Chapter 2, equations (2.9) and (2.10), can be rewritten in the dimensionless parameters as

Radial flow:

$$p_D(y_D, z_D) = \frac{q_D}{2\pi} \ln\left(\frac{\sqrt{y_D^2 + z_D^2}}{r_{wD}}\right), \text{ for } r_{rD} \le \sqrt{y_D^2 + z_D^2} \le 0.5 \tag{E.10}$$

Linear flow:

$$p_D(y_D, z_D) = \frac{q_D}{2\pi} \ln\left(\frac{0.5}{r_{wD}}\right) + 0.5 q_D (y_D - 0.5) \text{ , for } y_D \ge 0.5 \tag{E.11}$$

To illustrate the dimensionless pressure profiles in a reservoir, we compare the conformal mapping solution and the radial-linear composite solution at $z_D = 0$ and $z_D = 0.5$ presented in Figure E.2. Note that p_{Dwell} is the p_D evaluated at $r_D = r_{wD}$ where $y_D = r_w$ and $z_D = 0$.

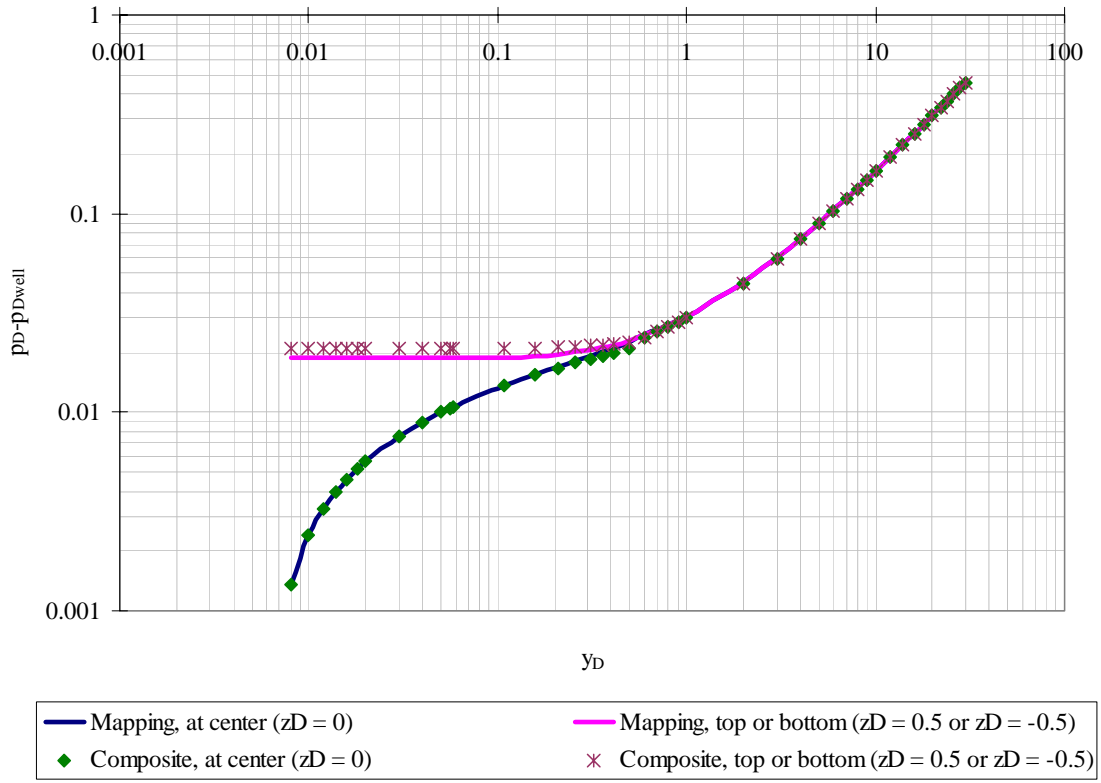Figure E.2   Comparison of conformal mapping model and composite model at
$r_{wD} = 0.006$ and $q_D = 0.02957$.

E.2   ENERGY BALANCE

The dimensionless solution of the energy balance for radial-linear composite flow

is derived as the following.

Radial region:

$$\rho C_p u_r \frac{dT}{dr} - \beta T u_r \frac{dp}{dr} + u_r \frac{dp}{dr} - K_{Tt} \frac{1}{r} \frac{d}{dr}\left(r \frac{dT}{dr} \right) = 0 \tag{E.12}$$

155

The above equation can be arranged into dimensionless groups as below.

$$r_D^2 \frac{d^2 T_D}{d r_D^2} + (a_D + 1) r_D \frac{d T_D}{d r_D} + b_D T_D = d_D \qquad \text{(E.13)}$$

where

$$T_D = \frac{T}{T_o}$$

$$r_D = \frac{r}{h}$$

$$a_D = -\frac{\rho C_p}{K_{Tt}} \left(\frac{q}{2\pi L} \right) = \frac{G_{1D}}{\pi}$$

$$b_D = -\frac{\mu \beta}{k K_{Tt}} \left(\frac{q}{2\pi L} \right)^2 = \frac{G_{2D}}{\pi^2}$$

$$d_D = -\frac{\mu \beta}{k K_{Tt} T_o} \left(\frac{q}{2\pi L} \right)^2 = \frac{G_{3D}}{\pi^2}$$

Equation (E.13) is solved in a similar manner as presented in Section 3.3. The radial dimensionless solution is

$$T_D(r_D) = C_{oD} r_D^{m_{oD}} + C_{rD} r_D^{m_{rD}} + \frac{G_{3D}}{G_{2D}} \qquad \text{(E.14)}$$

where

156

$$m_{oD} = \frac{-a_D - \sqrt{a_D{}^2 - 4b_D}}{2}$$

(E.15)

$$m_{rD} = \frac{-a_D + \sqrt{a_D{}^2 - 4b_D}}{2}$$

(E.16)

Linear region:

$$\rho C_p u_y \frac{dT}{dy} - \beta T u_y \frac{dp}{dy} + u_y \frac{dp}{dy} - \frac{d}{dy}\left(K_{Tt}\frac{dT}{dy}\right) = 0$$

(E.17)

The above equation can be rearranged into dimensionless form as below.

$$\frac{d^2 T_D}{d y_D^2} + G_{1D}\frac{dT_D}{d y_D} + G_{2D}T_D = G_{3D}$$

(E.18)

where

$$T_D = \frac{T}{T_o}$$

$$y_D = \frac{y}{h}$$

$$G_{1D} = -\frac{\rho C_p}{K_{Tt}}\left(\frac{q}{2L}\right)$$ (note that q is negative for production)

$$G_{2D} = -\frac{\beta\mu}{kK_{Tt}}\left(\frac{q}{2L}\right)^2$$

$$G_{3D} = -\frac{\mu}{kK_{Tt}T_o}\left(\frac{q}{2L}\right)^2$$

The equation (E.18) is solved in a similar manner as presented in Section 3.3. The linear dimensionless solution is

$$T_D(y_D) = C_{1D}e^{m_{1D}y_D} + C_{2D}e^{m_{2D}y_D} + \frac{G_{3D}}{G_{2D}} \tag{E.19}$$

where

$$m_{1D} = \frac{-G_{1D} - \sqrt{G_{1D}^2 - 4G_{2D}}}{2} \tag{E.20}$$

$$m_{2D} = \frac{-G_{1D} + \sqrt{G_{1D}^2 - 4G_{2D}}}{2} \tag{E.21}$$

Apply the boundary conditions to evaluate the integration constants $(C_{oD}, C_{rD}, C_{1D}, C_{2D})$.

1) T_D is finite as r_D approaches zero.

2) $\left(\dfrac{dT_D}{dr_D}\right)_{r_D=0.5} = \left(\dfrac{dT_D}{dy_D}\right)_{y_D=0.5}$

158

3) $\quad T_D(r_D = 0.5) = T_D(y_D = 0.5)$

4) $\quad T_D(y_D = Y_D / 2) = 1$

The integration constants are

$$C_{oD} = 0$$

$$C_{rD} = \frac{D_x}{D}$$

$$C_{1D} = \frac{D_y}{D}$$

$$C_{2D} = \frac{D_z}{D}$$

where

$$D = 0.5^{m_{rD}} \left[e^{0.5 m_{1D} + m_{2D} Y_D / 2} (m_{1D} - 2 m_{rD}) - e^{0.5 m_{2D} + m_{1D} Y_D / 2} (m_{2D} - 2 m_{rD}) \right]$$

$$D_x = \left(1 - \frac{G_{3D}}{G_{2D}} \right) e^{0.5 m_{2D}} \left(m_{1D} e^{0.5 m_{1D}} - m_{2D} e^{0.5 m_{1D}} \right)$$

$$D_y = -\left(1 - \frac{G_{3D}}{G_{2D}} \right) e^{0.5 m_{2D}} 0.5^{m_{rD}} \left(m_{2D} - 2 m_{rD} \right)$$

$$D_z = \left(1 - \frac{G_{3D}}{G_{2D}}\right) e^{0.5m_{1D}} 0.5^{m_{rD}} \left(m_{1D} - 2m_{rD}\right)$$

Once the integration constants are evaluated, the particular solutions are equation (E.14) for $r_{wD} \leq r_D \leq 0.5$ and the equation (E.19) for $y_D \geq 0.5$. The illustration of the dimensionless temperature profile for reservoir flow is shown in Figure E.3. The dimensionless groups that correspond to the dimensionless pressure profiles (Figure E.2) are $G_{1D} = 6.1291$, $G_{2D} = -0.0016$, $G_{3D} = -0.0038$, $Y_D = 60$, $r_{wD} = 0.006$.

To verify the dimensionless groups, we arbitrarily vary the rock and fluid properties such that the dimensionless groups do not change. The values of parameters used in each case are presented in Table E.1. The calculation results, plotted in Figure E.3, show a perfect agreement with the base case.

Table E.1   Rock and fluid properties for verifying the dimensionless groups.

|	Base case	Case 1	Case 2	Case 3
Density [lbm/ft^3]	40	33.333	40	40
Heat capacity [Btu/(lb-^{o}F)]	0.524	0.6288	0.524	0.524
Flow rate [bbl/d]	5000	5000	6250	5000
Producing length [feet]	1000	1000	1250	1000
Permeability [md]	50	50	50	95
Viscosity [cp]	1	1	1	1.9
Total conductivity [Btu/(hr-ft-^{o}F)]	2	2	2	2
G_{1D}	6.1291	6.1291	6.1291	6.1291
G_{2D}	-0.0016	-0.0016	-0.0016	-0.0016
G_{3D}	-0.0038	-0.0038	-0.0038	-0.0038
Y_D	60	60	60	60
r_{wD}	0.006	0.006	0.006	0.006
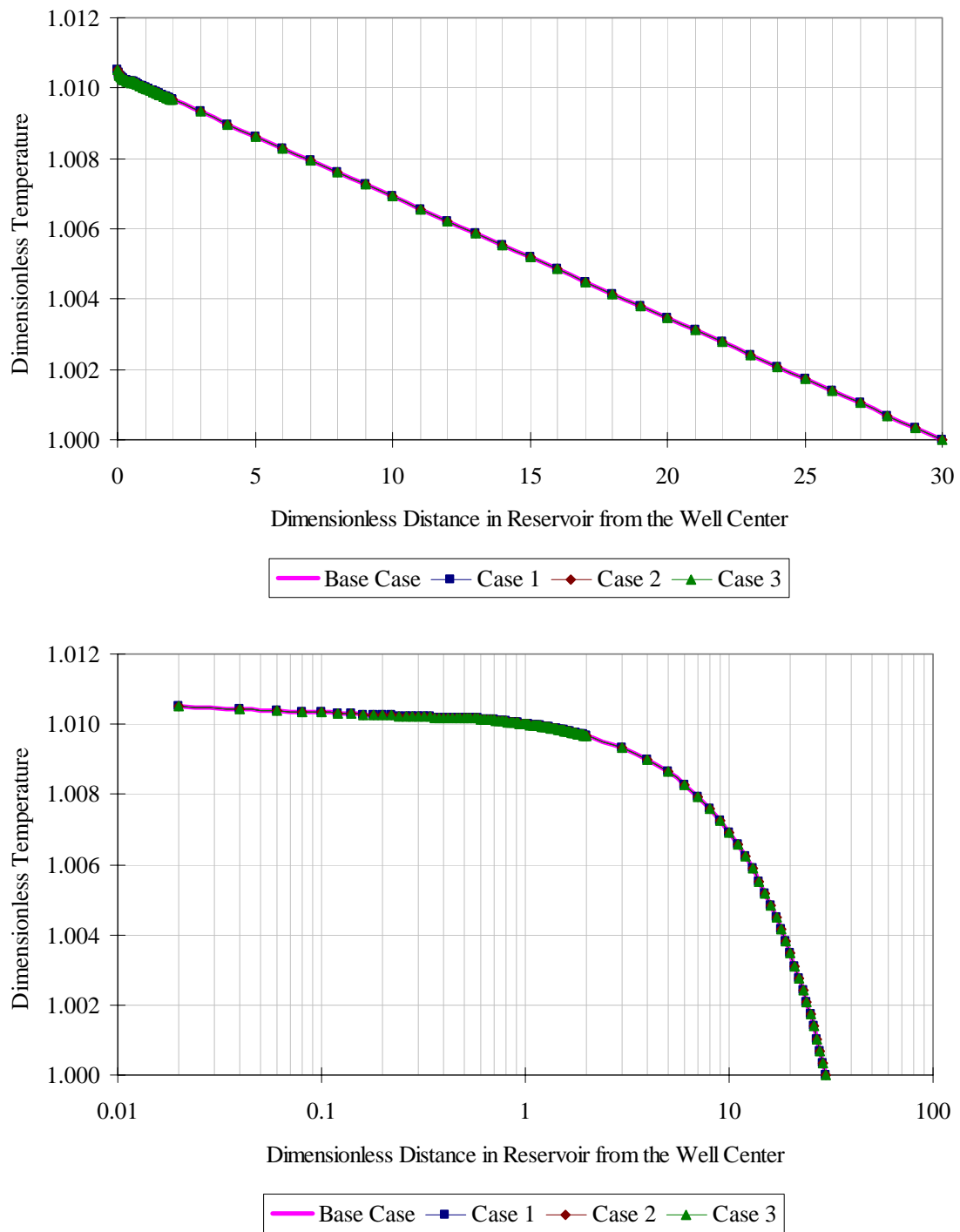
Figure E.3 Reservoir dimensionless temperature profile in linear scale (top) and semi-log scale (bottom).

162

The dimensionless inflow temperatures are obtained from the dimensionless radial solution evaluated at $r_D = r_{wD}$. The illustrations of how the dimensionless inflow temperatures change with respect to each dimensionless group are presented in Figure E.4 through E.6 in which the dimensionless groups that are not varied are constant at $G_{1D} = 6.1291$, $G_{2D} = -0.0016$, $G_{3D} = -0.0038$, $Y_D / 2 = 30$, $r_{wD} = 0.006$.

Physically, the three dimensionless groups represent the causes of temperature changes. G_{1D} is a representation of heat convection. G_{2D} is a representation of thermal expansion of fluid. G_{3D} is a representation of viscous dissipation. In Figure E.4, when G_{2D} is large (i.e. large thermal expansion), the dimensionless inflow temperatures are less than one (cooling effect). On the contrary, when G_{2D} is small, the dimensionless inflow temperature is greater than one, which means that viscous dissipation is more than thermal expansion (heating effect). The last conclusion that can be drawn is that the dominant causes of temperature changes are the thermal expansion (G_{2D}) and the viscous dissipation (G_{3D}).
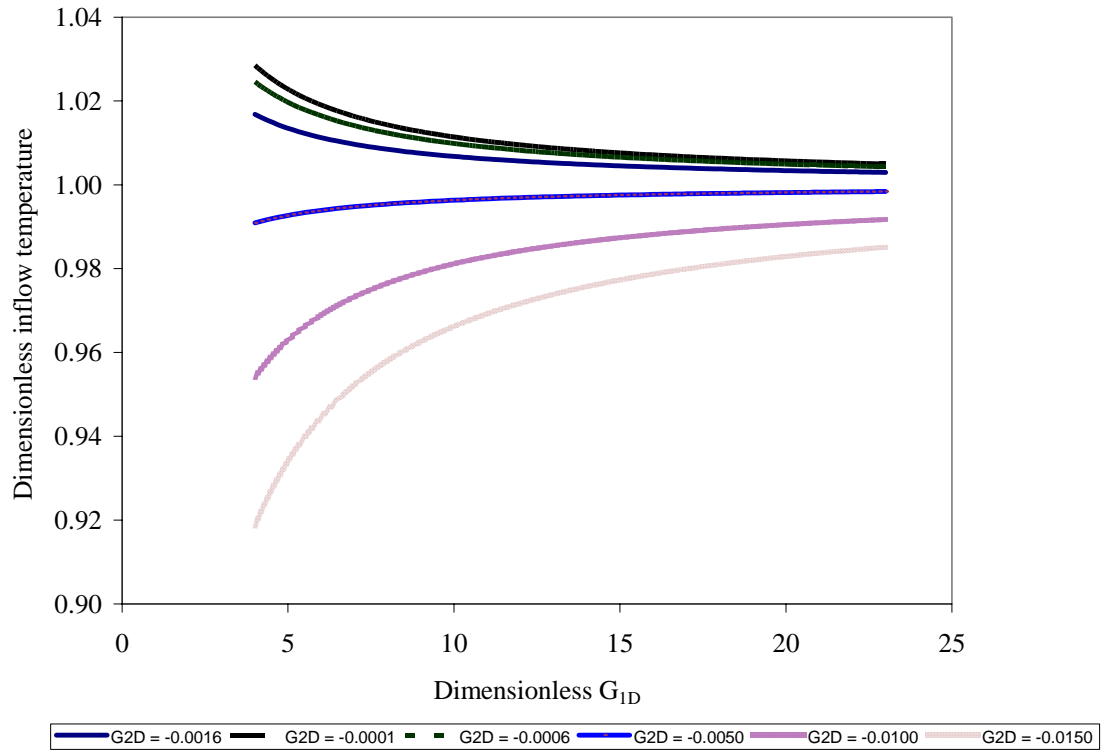
Figure E.4   Change of the dimensionless inflow temperature with respect to G_{1D}
($G_{3D} = -0.0038$, $Y_D / 2 = 30$, $r_{wD} = 0.006$).

Figure E.5   Change of the dimensionless inflow temperature with respect to G_{2D}.
($G_{1D} = 6.1291$, $G_{3D} = -0.0038$, $Y_D / 2 = 30$, $r_{wD} = 0.006$)

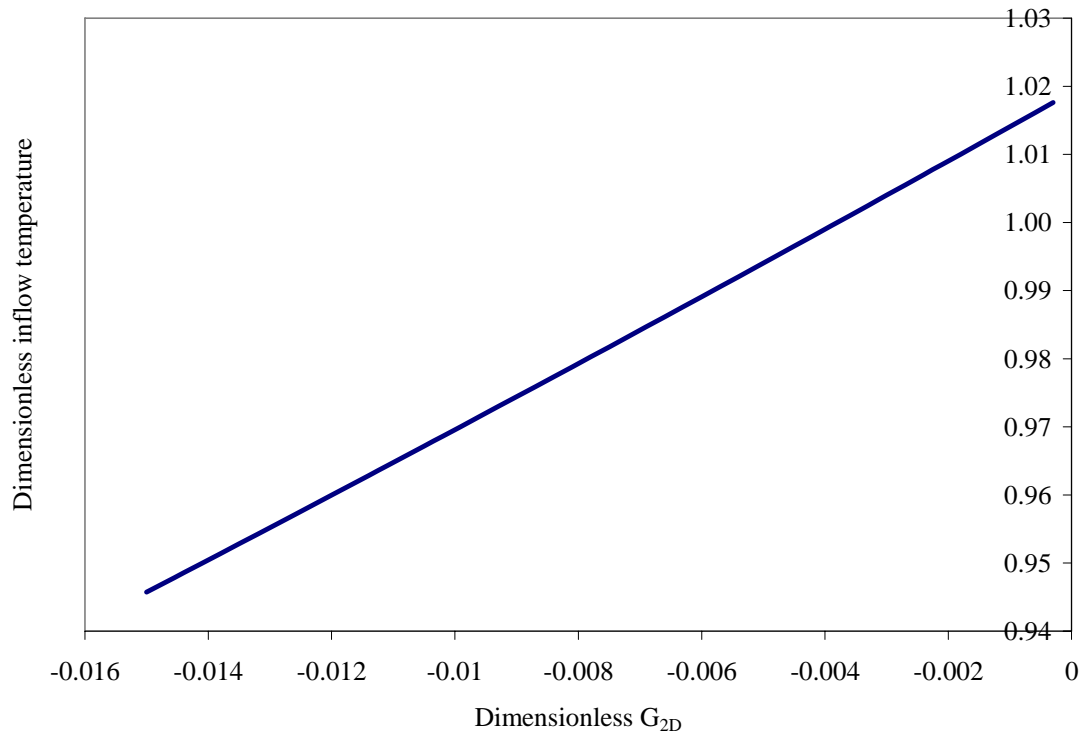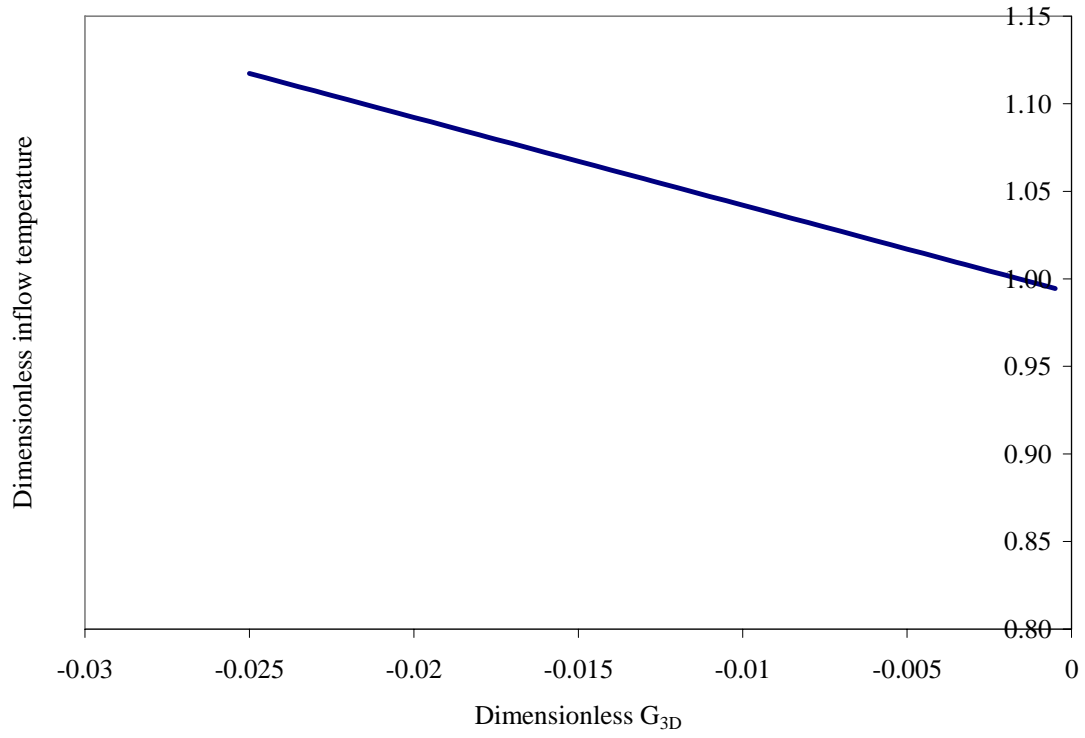Figure E.6   Change of the dimensionless inflow temperature with respect to G_{3D}.
($G_{1D} = 6.1291$, $G_{2D} = -0.0016$, $Y_D / 2 = 30$, $r_{wD} = 0.006$)

References

Aguilera, R., Artindale, J. S., Cordell, G. M., Ng, M. C., Nicholl, G. W., and Runions, G. A.: Horizontal Wells, Gulf Publishing Company, Houston, TX, 1991.

Al-Hadhrami, A. K., Elliott, L., and Ingham, D. B.: "A New Model for Viscous Dissipation in Porous Media Across a Range of Permeability Values," *Transport in Porous Media*, p. 117-122, Netherlands, 2003.

Anand, J., Somerton, W. H., and Gomaa, E.: "Predicting Thermal Conductivities of Formations From Other Known Properties," *Society of Petroleum Engineering Journal*, p. 267-273, October 1973.

Aziz, K., and Settari, A.: Petroleum Reservoir Simulation, Applied Science Publishers Ltd., London, United Kingdom, 1979.

Beggs, H. D., and Robinson, J. R.: "Estimating the Viscosity of Crude Oil Systems," *Journal of Petroleum Technology*, p. 1140-1141, September 1975.

Besson, J.: "Performance of Slanted and Horizontal Wells on an Anisotropic Medium," paper SPE 20965 presented at the Europec 90, The Hague, Netherlands, 22-24 October, 1990.

Bird, R. B., Stewart, W. E., and Lightfoot, E. N.: Transport Phenomena, Second Edition, John Wiley and Sons, New York, NY, 2002.

Brown, G. A., Kennedy, B., and Meling, T.: "Using Fibre-Optic Distributed Temperature Measurements to Provide Real-Time Reservoir Surveillance Data on Wytch Farm Field Horizontal Extended-Reach Wells," paper SPE 62952 presented at the SPE Annual Technical Conference and Exhibition, Dallas, TX, 1-4 October, 2000.

Brown, G., Storer, D., McAllister, K., Al-Asimi, M., and Raghavan, K.: "Monitoring Horizontal Producers and Injectors During Cleanup and Production Using Fiber-Optic-Distributed Temperature Measurements," paper SPE 84379 presented at the SPE Annual Technical Conference and Exhibition, Denver, CO, 5-8 October, 2003.

Butler, R. M.: Horizontal Wells for the Recovery of Oil, Gas, and Bitumen, The Petroleum Society of the Canadian Institute of Mining, Metallurgy and Petroleum, Calgary, Canada, 1994.

Carr, T. R., Mason, E. P., and Feazel, C. T.: <u>Horizontal Wells Focus on the Reservoir</u>, American Association of Petroleum Geologists, Tulsa, OK, 2003.

Carslaw, H. S., and Jaeger, J. C.: <u>Conduction of Heat in Solids</u>, Second Edition, Oxford University Press, Oxford, United Kingdom, 1959.

Cassis, R., Fuller, N., Hepler, L. G., McLean, R. J., Skauge, A., Srinivasan, N. S., and Yan, H.: "Specific Heat Capacities of Bitumens and Heavy Oils, Reservoir Minerals, Clays, Dehydrated Clays, Asphaltenes and Cokes," *Alberta Oil Sands Technology and Research Authority Journal of Research*, p. 163-173, January 1985.

Chaperon, I. : "Theoretical Study of Coning Toward Horizontal and Vertical Wells in Anisotropic Formations: Subcritical and Critical Rates," paper SPE 15377 presented at the SPE Annual Technical Conference, New Orleans, LA, 5-8 October, 1986.

Chauvel, Y. L., and Oosthoek, P.: "Production Logging in Horizontal Wells: Applications and Experience to Date," paper SPE 21094 presented at the SPE Latin American Petroleum Engineering Conference, Rio de Janeiro, Brazil, 14-19 October, 1990.

Chen, W., Zhu, D., and Hill, A. D.: "A Comprehensive Model of Multilateral Well Deliverability," paper SPE 64751 presented at the SPE International Oil and Gas Conference and Exhibition, Beijing, China, 7-10 November, 2000.

Collins, A. G.: "Properties of Produced Waters," <u>Petroleum Engineering Handbook</u>, Bradley, H. B. *et al.* (editors), p. 24-17, Society of Petroleum Engineers, Dallas, TX, 1987.

Coludrovich, E. J., McFadden, J. D., Palke, M. R., Roberts, W. R., and Robson, L. J.: "The Boris Field Well Management Philosophy – The Application of Permanent Downhole Flowmeters to Pressure Transient Analysis: An Integrated Approach ," paper SPE 90316 presented at the SPE Annual Technical Conference and Exhibition, Houston, TX, 26-29 September, 2004.

Connolly, E.T.: "Resume and Current Status of the Use of Logs in Production," paper L presented at the SPWLA annual logging symposium, Dallas, TX, 4-7 May, 1965.

Cooke, C. E. Jr.: "Radial Differential Temperature (RDT) Logging-A New Tool for Detecting and Treating Flow Behind Casing," *Journal of Petroleum Technology*, p. 676, June 1979.

Corey, A. T.: <u>Mathematics of Immiscible Fluids in Porous Media</u>, Water Resources Publication, Littleton, CO, 1986.

Curtis, M. R., and Witterholt, E. J.: "Use of the Temperature Log for Determining Flow Rates in Producing Wells," paper SPE 4637 presented at the SPE Annual Meeting, Las Vegas, NV, 30 September-3 October, 1973.

Davis, E. R.: "Interpretation of Fracture Height with Temperature Logs," MS Thesis, The University of Texas at Austin, Austin, TX, 1993.

Decarre, S., and Fabre, J.: "Phase Inversion Prediction Study," *Jounal of L'Institut Francais du Petrole*, 1997.

Dikken, B. J.: "Pressure Drop in Horizontal Wells and Its Effect on Production Performance", *Journal of Petroleum Technology*, p. 1426-1433, November 1990.

Dranchuk, P. M, and Abou-Kassem, J. H.: "Calculation of z-Factors for Natural Gases Using Equations of State," *Journal of Canada Petroleum Technology*, p. 34-36, July, 1975.

Economides, M. J., Hill, A. D., and Ehlig-Economides, C.: <u>Petroleum Production Systems</u>, Prentice Hall, Saddle River, NJ, 1994.

Elshahawi, H. M. R.: "A Theoretical Study of Temperature Variations in Wellbores: Implications for Temperature Logging," MS Report, The University of Texas at Austin, Austin, TX, 1997.

Erlandsen, S. M.: "Production Experience From Smart Wells in the Oseberg Field," paper SPE 62953 presented at the SPE Annual Technical Conference and Exhibition, Dallas, TX, 1-4 October, 2000.

Furui, K., Zhu, D., and Hill, A. D.: "A Rigorous Formation Damage Skin Factor and Reservoir Inflow Model for a Horizontal Well," *SPE Production and Facilities*, p. 151-157, August 2003.

Foucault, H., Poilleux, D., Djurisic, A., Slikas, M., Strand, J., and Silva, R.: "A Successful Experience for Fiber Optic and Water Shut Off on Horizontal Wells with Slotted Liner Completion in an Extra Heavy Oil Field," paper SPE 89405 presented at the SPE/DOE Fourteenth Symposium on Improved Oil Recovery, Tulsa, OK, 17-21 April, 2004.

Gambill, W. R.: "You Can Predict Heat Capacities," *Chemical Engimeering*, p. 42-46, June, 1957.

Giger, F.: "Analytic 2D Models of Water Cresting Before Breakthrough for Horizontal Wells," paper SPE 15378 presented at the SPE Annual Technical Conference, New Orleans, LA, 5-8 October, 1986.

Goins, W. C. Jr., and Dawson, D. D. Jr.: "Temperature Surveys to Locate Zone of Lost Circulation," *Oil and Gas Journal*, p. 170, 22 June, 1953.

Gringarten, A. C., and Ramey, H. J. Jr.: "The Use of Green's Functions in Solving Unsteady-Flow Problem in Reservoirs," *SPE Journal*, p. 285-296, October, 1973.

Haddad, S., Proano, E., and Patel, Y.: "A Method to Diagnose Depletion, Skin, kh, and Drive Mechanism Effects Using Reservoir Monitoring Data," paper SPE 90032 presented at the SPE Annual Technical Conference and Exhibition, Houston, TX, 26-29 September, 2004.

Hasan, A. R., and Kabir, C. S.: "Aspects of Wellbore Heat Transfer During Two-Phase Flow," *SPE Production and Facilities*, p. 211, August 1994.

Hasan, A. R., and Kabir, C. S.: Fluid Flow and Heat Transfer in Wellbores, Society of Petroleum Engineers, Richardson, TX, 2002.

Hill, A. D.: Production Logging-Theoretical and Interpretive Elements, Society of Petroleum Engineers, Richardson, TX, 1990.

Jones, C.: "The Use of Bottomhole Temperature Variation in Production Testing," paper SPE 18381 presented at the SPE European Conference, London, United Kingdom, 16-19 October, 1988.

Jorden, J., and Campbell, F.: Well Logging for Physical Properties (Vol. I): Borehole Environment, Mud and Temperature Logging, Society of Petroleum Engineers, Dallas, TX, 1984.

Joshi, S. D.: Horizontal Well Technology, PennWell Publishing Company, Tulsa, OK, 1991.

Katz, D. L., and Lee, R. L.: Natural Gas Engineering: Production and Storage, McGraw-Hill Companies, New York, NY, 1990.

Keller, H. H., and Baldwin, W. F.: "Quantitative Interpretation of Temperature Logs," paper SPE 5091 presented at the SPE Annual Technical Conference and Exhibition, Houston, TX, 6-9 October, 1974.

Kragas, T. K., Turnbull, B. F., and Francis, M. J.: "Permanent Fiber-Optic Monitoring at Northstar: Pressure/Temperature System and Data Overview," *SPE Production and Facilities*, p. 86-93, May 2004.

Kreyszig, E.: Advanced Engineering Mathematics, Eighth Edition, John Wiley & Sons, New York, NY, 1999.

Kunz, K. S., and Tixier, M. P.: "Temperature Surveys in Gas Producing Wells," *Journal of Petroleum Technology*, p. 111, July 1955.

Lake, L. W.: Enhanced Oil Recovery, Prentice Hall, Saddle River, NJ, 1989.

Lanier, G. H., Brown, G., and Adams, L.: "Brunei Field Trial of a Fibre Optic Distributed Temperature Sensor (DTS) System in a 1,000m Open Hole Horizontal Oil Producer," paper SPE 84324 presented at the SPE Annual Technical Conference and Exhibition, Denver, CO, 5-8 October, 2003.

Larson, R. E., Hostetler, R. P., and Edwards, B. H.: Calculus, Fourth Edition, D.C. Heath and Company, Lexington, MA, 1990.

Lee, A. L., Gonzales, M. H., and Eakin, B. E.: "The Viscosity of Natural Gases," *AIME Transactions*, p. 997-1000, 1966.

Lewis, R. W., Morgan, K., and Zienkiewicz, O. C.: Numerical Methods in Heat Transfer, John Wiley and Sons, New York, NY, 1981.

Li, H., Zhu, D., Lake, L. W., and Hill, A. D.: "A New Method to Interpret Two-Phase Profiles from Temperature and Flowmeter Logs," paper SPE 56793 presented at the SPE Annual Technical Conference and Exhibition, Houston, TX, 3-6 October, 1999.

Maubeuge, F., Didek, M., Beardsell, M. B., Arquis, E., Bertrand, O., and Caltagirone, J. P.: "MOTHER : A Model for Interpreting Thermometrics," paper SPE 28588 presented at the SPE Annual Technical Conference and Exhibition, New Orleans, LA, 25-28 September, 1994.

McCain, W. D. Jr.: The Properties of Petroleum Fluids, second edition, PennWell Publishing Company, Tulsa, OK, 1990.

McKinley, R. M.: "Production Logging," paper SPE 10035 presented at the SPE International Petroleum Exhibition and Technical Symposium, Beijing, China, 18-26 March, 1982.

Moler, C. B.: Numerical Computing with Matlab, Society for Industrial and Applied Mathematics, Philadelphia, PA, 2004.

Ng, J.T., and Egbogah, E.O.: "An Improved Temperature Viscosity Correlation for Crude Oil Systems," paper 833432 presented at the Annual Technical Meeting of the Petroleum Society of CIM, Banff, Alberta, Canada, 1983.

Ouyang, L. B., and Aziz, K.: "A Simplified Approach to Couple Wellbore Flow and Reservoir Inflow for Arbitrary Well Configurations," paper SPE 48936 presented

at the SPE Annual Technical Conference and Exhibition, New Orleans, LA, 27-30 September, 1998.

Ouyang, L. B., and Aziz, K.: "A Homogeneous Model for Gas-Liquid Flow in Horizontal Wells," *Journal of Petroleum Science and Engineering*, p. 119-128, 2000.

Ouyang, L. B., and Belanger, D.: "Flow Profiling via Distributed Temperature Sensor (DTS) System-Expectation and Reality," paper SPE 90541 presented at the SPE Annual Technical Conference and Exhibition, Houston, TX, 26-29 September, 2004.

Owodunni, A., Travis, T., and Dunk, G.: "The Use of Multilateral Technology to Arrest Production Decline in a West-Texas Gas Field," paper SPE 84029 presented at the SPE Annual Technical Conference and Exhibition, Denver, CO, 5-8 October, 2003.

Ozkan, E., and Raghavan, R.: "A Breakthrough Time Correlation for Coning Toward Horizontal Wells," paper SPE 20964 presented at Europec Conference, The Hague, Netherlands, 22-24 October, 1990.

Peaceman, D. W.: "Interpretation of Well-Block Pressure in Numerical Reservoir Simulation," *SPE Journal*, p. 183-194, June 1978.

Peaceman, D. W.: "Interpretation of Well-Block Pressure in Numerical Reservoir Simulation With Nonsquare Grid Blocks and Anisotropic Permeability," *SPE Journal*, p. 531-543, June 1983.

Peaceman, D. W.: "Interpretation of Wellblock Pressures in Numerical Reservoir Simulation: Part 3- Off-Center and Multiple Wells Within a Wellblock," *SPE Reservoir Engineering*, p. 227-232, May 1990.

Perry, R. H., Green, D. W., and Maloney, J. O.: Perry's Chemical Engineers' Handbook, sixth edition, McGraw-Hill Book Company, New York, NY, 1984.

Pratap, R.: Getting Started with Matlab, Oxford University Press, Oxford, United Kingdom, 2002.

Prats, M.: Thermal Recovery, Society of Petroleum Engineers, Richardson, TX, 1982.

Ramakrishnan, T. S., and Raghuraman, B.: "A Method for Continuous Interpretation of Permanent Monitoring Pressure Data," paper SPE 90910 presented at the SPE Annual Technical Conference and Exhibition, Houston, TX, 26-29 September, 2004.

Ramey, H. J. Jr.: "Wellbore Heat Transmission," *Journal of Petroleum Technology*, p. 427-435, April 1962.

Romero-Juarez, A.: "A Note on the Theory of Temperature Logging," *SPE Journal*, p. 375, December 1969.

Sagar, R. K., Dotty, D. R., and Schmidt, Z.: "Predicting Temperature Profiles in a Flowing Well," *SPE Production Engineering*, p. 441, November 1991.

Sandler, S. I.: Chemical and Engineering Thermodynamics, Third Edition, John Wiley and Sons, New York, NY, 1999.

Sensornet Limited, "DTS Advantages and Technology," /www.sensornet.co.uk/, 2006.

Shampine, L. F., Gladwell, I., and Thompson, S.: Solving ODE's with Mathlab, Cambridge University Press, Cambridge, United Kingdom, 2003.

Shih, T. M.: Numerical Properties and Methodologies in Heat Transfer, Hemisphere Publishing Corporation, New York, NY, 1983.

Shook, M., Li, D., and Lake, L. W.: "Predicting Temperature Profiles in a Flowing Well," *SPE Production Engineering*, p. 441, November 1991.

Silva, M. I. D. O., and Kato, T.: "Reservoir Management Optimization Using Permanent Downhole Gauge Data," paper SPE 90973 presented at the SPE Annual Technical Conference and Exhibition, Houston, TX, 26-29 September, 2004.

Delt Universtiy, "Smart Wells," www.dietzlab.tudelft.nl/, 2006.

Standing, M. B.: Volumetric and Phase Behavior of Oil Field Hydrocarbon Systems, Society of Petroleum Engineers, Dallas, TX, 1977.

Steffensen, R. J., and Smith, R. C.: "The Importance of Joule-Thomson Heating (or Cooling) in Temperature Log Interpretation," paper SPE 4636 presented at the Annual Fall Meeting of the Society of Petroleum Engineers of AIME, Las Vegas, NV, 30 September - 3 October, 1973.

Sutton, R.P.: "Compressibility Factors for High-Molecular-Weight Reservoir Gases," paper SPE 14265 presented at the SPE Annual Technical Conference and Exhibition, Las Vegas, NV, 22-25 September, 1985.

Tolan, M., Boyle, M., and Williams, G.: "The Use of Fiber-Optic Distributed Temperature Sensing and Remote Hydraulically Operated Interval Control Valves for the Management of Water Production in the Douglas Field," paper SPE 71676 presented at the SPE Annual Technical Conference and Exhibition, New Orleans, LA, 30 September-3 October, 2001.

Yoshioka, K.: "A Comprehensive Statistically-Based Method to Interpret Real-Time Flowing Measurments," PhD dissertation, Texas A&M University, College Station, TX, Anticipated in 2007.

Yoshioka, K., Zhu, D., Hill, A. D., and Lake, L. W.: "Interpretation of Temperature and Pressure Profiles Measured in Multilateral Wells Equipped with Intelligent Completions," paper SPE 94097 presented at the Europec Biennial Conference, Madrid, Spain, 13-16 June, 2005.

Zhu, D.: "Effect of Temperature on Minifrac Pressure Behavior," PhD dissertation, The University of Texas at Austin, Austin, TX, 1992.